QUANTUM ELECTRONIC EFFECTS IN ULTRATHIN METAL
FILMS ON SEMICONDUCTORS

BY

PETER JEREMY CZOSCHKE

B.A., Carleton College, 1997
M.S., University of Illinois at Urbana-Champaign, 2002

DISSERTATION

Submitted in partial fulfillment of the requirements
for the degree of Doctor of Philosophy in Physics
in the Graduate College of the
University of Illinois at Urbana-Champaign, 2005

Urbana, Illinois

Abstract

As the size of a metallic system approaches the atomic scale, deviations from the bulk are expected in a plethora of different physical properties due to quantum size effects. In this work, two of these effects are investigated in detail: the structural distortions that arise due to quantum confinement of a metal's itinerant electrons to an ultrathin film and variations in the surface energy (relative stability) of such films as a function of thickness. These effects are first examined from a theoretical viewpoint, where models based upon a free-electron gas confined to a one-dimensional quantum well are derived to illustrate the basic physical phenomena. These models are engineered such that they are realistic enough to be used in the analysis of empirical data with the adjustment of a small number of phenomenological parameters.

These effects are then investigated experimentally using surface x-ray diffraction at a third-generation synchrotron radiation facility (the Advanced Photon Source at Argonne National Laboratory). Extended reflectivity spectra from smooth atomic-scale Pb films prepared on Si(111) substrates at 110 K are obtained for thicknesses of 6–19 atomic layers that exhibit distinctive features indicative of quasibilayer lattice distortions. A detailed analysis shows variations within the layer structure of each film that are correlated with Friedel-like charge density oscillations at the film boundaries. Variations in the lattice distortions are also observed as a function of thickness with a quasibilayer periodicity. This effect is explained in the context of quantum size effects using the theoretical models.

A second experiment is also described in which initially smooth Pb films are progressively annealed from 110 K to near room temperature. The film morphology is examined every 5–10 K by scanning the extended x-ray reflectivity, which reveals the initially smooth films breaking up into islands of specific heights. Once the samples reach a state of quasi-equilibrium, the distributions of island heights are measured, which show strong quasibilayer variations in the relative stability of different height islands (film thicknesses). These variations are related to electronic contributions to the surface energy using the free-electron-based theoretical models.

Acknowledgments

This research and dissertation would not have been possible without the help and support of many people. In particular, I would like to thank my advisor, Professor Tai-Chang Chiang, for always being there for questions, answers, or just friendly discussions. I would also like to thank the staff at the UNICAT beamline, in particular Hawoong Hong, who spent many a late night with me troubleshooting a technical problem or mulling over the latest strange diffraction pattern we were seeing. Past and current members of the Chiang National Lab research group also deserve mention, especially Tim Kidd and Martin Holt, who both helped me in those early years of my graduate career when I needed to learn the basics and develop the self-confidence to be a good scientist.

I am also very grateful for the personal support I received from my family. Many thanks go to my Mom and Dad, who instilled in me a great love for learning and a thirst for knowledge; to my wife, Becky, who was willing to pull up anchor in Minnesota from her friends and family to come out to the middle of corn country, just to let me follow my dream of getting the best education possible. Her love and support were always there for me, something on which I knew I could always rely. Last but not least, a big kiss and hug go to my baby daughter, Meredith, who showed (is showing) me what the truly important things in life are.

Table of Contents

List of Figures

List of Tables

List of Abbreviations

1D,2D,3D	One-, Two-, and Three-Dimensional.
AL	Atomic Layer.
APS	Advanced Photon Source.
c/s	Counts per second.
CTR	Crystal Truncation Rod.
fcc	Face-centered cubic.
HAS	Helium Atom Scattering.
ID	Insertion Device.
LEED	Low Energy Electron Diffraction.
MBE	Molecular Beam Epitaxy.
QSE	Quantum Size Effects.
RHEED	Reflection High Energy Electron Diffraction.
r.l.u.	Reciprocal lattice unit(s).
rms	Root-mean-square.
STM	Scanning Tunneling Microscopy.
SXRD	Surface X-Ray Diffraction.
TDS	Thermal Diffuse Scattering.
TSP	Titanium Sublimation Pump.
UHV	Ultrahigh Vacuum.
UNICAT	University, National Laboratory, Industry Collaborative Access Team.

List of Symbols and Constants

α, β The angles the incident and exit x-ray beams make with the sample surface. In a specular geometry, $\alpha \approx \beta$.

Δ Charge spillage at one interface of a film, in units of length.

ϵ_0 Permittivity of the vacuum, 8.854×10^{-12} C^2/(J m).

$\varepsilon_b, \varepsilon_s$ Energy densities of the bulk and surface, respectively. Note that the bulk density has units of energy per volume whereas the surface density is in energy per area.

θ The Bragg angle for a reflection.

2θ The scattering angle, which is the angle between $\mathbf{k}_i$ and $\mathbf{k}_f$. In a specular geometry, $2\theta = \alpha + \beta$. Also related to the magnitude of the momentum transfer (for elastic scattering) as $q = 2k\sin(2\theta/2)$.

θ_n The occupancy (coverage) of layer n relative to a bulk Pb(111) layer.

λ X-ray wavelength, which in this study was 0.623 Å, corresponding to 19.9 keV.

Λ Partial coherence factor (see Sec. 2.6.4), $\Lambda = 1$ corresponds to a fully coherent structure factor.

ρ Charge density.

ω Sample rocking angle (offset from specular), $\omega = (\alpha - \beta)/2$.

a A lattice constant of the conventional unit cell. For lead and silicon at 110 K, $a_{\mathrm{Pb}} = 4.92$ Å and $a_{\mathrm{Si}} = 5.43$ Å.

$\mathbf{a}$ A real-space basis vector (crystal axis) of the conventional unit cell.

$\mathbf{a}'$ A real-space basis vector (crystal axis) of the surface coordinate system. By convention, in SXRD $\mathbf{a}'_3$ is chosen to be nominally parallel to the surface normal of the sample.

A Surface area of a single film interface.

A_{cell} Area of the surface unit cell. For a (111)-oriented *fcc* or diamond surface, $A_{\text{cell}} = a^2\sqrt{3}/4$.

$\mathcal{A}$ Scattered x-ray amplitude.

b   A reciprocal-space basis vector.

c The speed of light, 2.998×10^8 m/s.

$\mathcal{C}$ Geometric correction factor(s).

D Total width of a theoretical quantum well.

e Unit of fundamental charge, 1.602×10^{-19} C.

E_F Fermi energy, $E_F = \frac{\hbar^2 k_F^2}{2m_e}$.

E_S The surface energy per surface atom of a film, $E_S = A_{\text{cell}}\varepsilon_s$.

$h, \hbar$ Planck's constant and Planck's constant over 2π, $h = 6.626 \times 10^{-34}$ m^2 kg/s.

hc The product of a photon's energy and wavelength, $12\,398.4$ eV Å.

$\dfrac{\hbar^2}{2m_e}$ Ratio of an electron's energy to k^2, 3.81 eV Å^2.

H, K, L Bulk-indexed Miller indices.

k_B Boltzmann's constant, 8.617×10^{-5} eV/K.

$\mathbf{k}, k$ Wave vector and its magnitude, usually in Å^{-1}. $\mathbf{k}_i$ and $\mathbf{k}_f$ refer to the wave vectors of the incident and exit x-ray beams, respectively, and $k = 2\pi/\lambda$.

k_F Fermi wave vector.

l The component of momentum transfer parallel to the surface normal, measured in Si(111) reciprocal lattice units (0.668 Å^{-1}), $l = q_z a_{\text{Si}}\sqrt{3}/(2\pi)$.

m_e Mass of the electron, 9.109×10^{-31} kg.

N Number of atomic layers in a film.

N_{val} The number of valence electrons per atom of film material ($N_{\text{val}} = 4$ for Pb).

p_N The fractional surface area covered by a film of thickness N AL.

$\mathbf{q}, q$ Momentum transfer and its magnitude, $\mathbf{q} \equiv \mathbf{k}_f - \mathbf{k}_i$.

r_0 The classical radius of the electron, also called the Thomson scattering length, $r_0 = \frac{e^2}{4\pi\epsilon_0 m_e c^2} = 2.817 \times 10^{-5}$ Å.

t Average interlayer spacing. For bulk Pb(111) at 110 K, $t =$ 2.84 Å.

T Temperature, taken in this study (Chapter 6) to be the annealing temperature.

V System volume. In model calculations of a film, $V = DA$.

Z Atomic number, or the number of electrons around an un-ionized atom.

1 Introduction

1.1 Quantum Size Effects

With the smallest feature size on current electronic devices already approaching the atomic scale, a fundamental understanding of the physical consequences of shrinking such devices is becoming increasingly important. When the thickness of a metal film or the size of a metallic nanostructure becomes comparable to the quantum coherence length of its itinerant electrons, effects due to confinement and quantization of the allowed electronic states become significant. Since these effects are highly size-dependent, they are generally termed quantum size effects (QSE). QSE have been observed in a multitude of different physical properties of metal nanostructures, including their transport characteristics, thermal stability, work function, superconducting transition temperature, electron-phonon coupling, electronic structure, surface charge density, growth behavior and morphology, chemical reactivity, and surface energy [1–45]. To further understand such effects on a fundamental physical level, it is useful to start with a simplified system in which only one of the three spatial dimensions has a length scale in the quantum regime. Thin films and quasi-two-dimensional nanostructures fall into this category and are the subject of this research. In particular, two effects will be focused upon: film lattice distortions due to QSE and variations in the surface energy as a function of film thickness or island height.

Both of these physical effects are examined experimentally using surface x-ray diffraction (SXRD) from a high-brilliance synchrotron source. In each case, ultrathin lead (Pb) films or film nanostructures grown on silicon (Si) substrates are the samples used as prototypes of the metal-on-semiconductor system. Pb/Si films were chosen for this research for several reasons. Due to decades of investment by the semiconductor industry, high-quality single-crystal wafers of Si are readily available and low-cost. For the same reason, systems based on Si surfaces are of great interest for technological applications. Furthermore, clean and smooth Si surfaces can be prepared very easily and reproducibly simply by heating the substrates to high temperatures *in vacuo*. Pb is an attractive material for use as a film because it

does not intermix with Si, so the Pb/Si interface is abrupt [46–49], and it is very free-electron-like, with a Fermi surface that is close to spherical [50]. In addition, previous studies have shown Pb films to be strongly affected by QSE, with interesting surface morphologies and growth behaviors having been observed and correlated with electronic structure (see below).

The electronic structure of a thin metal-on-semiconductor film can be viewed as a one-dimensional potential well in which the itinerant electrons of the metal are confined on one side by the film-vacuum potential barrier and on the other side by the band gap of the semiconductor. To aid in the experimental investigations and further elucidate the physics of QSE, a series of theoretical models based on a free-electron gas confined to such a quantum well are derived in Chapter 4. As the models are developed with the specific purpose of explaining empirical data, they are engineered to contain a small number of adjustable parameters to account for the specific phenomenology encountered in the experiments. The results from the models are then used in least-squares fitting routines to help explain the SXRD data.

1.2   Step Height Oscillations in Ultrathin Metal Films

One of the effects for which there is less experimental data available is the impact quantum confinement has on the lattice structural distortion (strain) of atomic-scale metal films relative to the bulk. Scanning tunneling microscopy (STM) and helium-atom scattering (HAS) experiments have all reported lattice distortions related to QSE [17–20]; however, these techniques probe primarily the electron density at the surface of the sample, shedding little light on the internal film or buried interface structure. A study using x rays, which scatter primarily off the electrons bound to the atomic cores and have long penetration lengths, can thus provide valuable complementary information to the existing body of work.

An example of results from a STM study [19] showing evidence of structural distortions in thin Pb/Si films is reproduced in Fig. 1.1. In this work, films were grown at 200 K, a temperature at which steep-sided islands form on the Si surface, between which is a single wetting layer. The samples are prepared in a metastable state in which stepped terraces are present on the island tops. The height profile of the island tops was then scanned to measure the step heights between terraces differing in thickness by a single atomic layer. As can be seen in the cross-sectional profile in Fig. 1.1(a), the step heights are different depending on the absolute height of the terraces N,
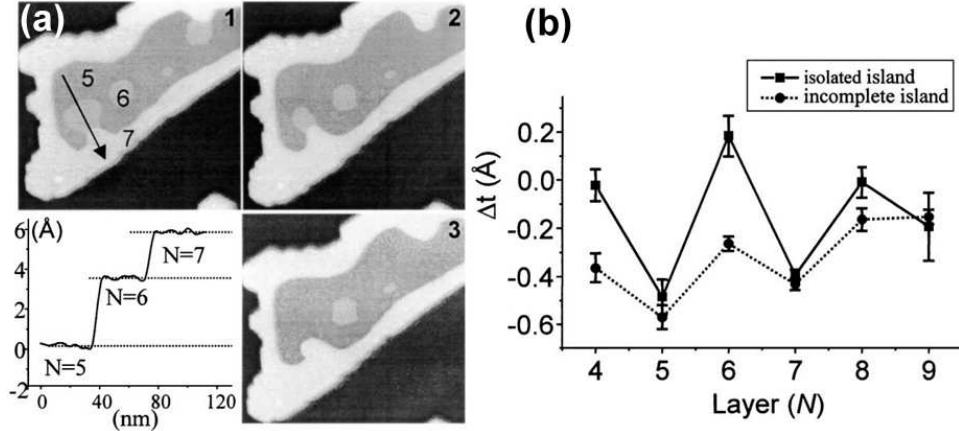
Figure 1.1: (a) STM images (300 nm×300 nm) showing evidence of step height variations as a function of thickness. The height profile is measured along the line shown in Frame 1. Frames 2 and 3 are subsequent images of the same island. (b) The deviation from the ideal island height as a function of the island height N, which shows bilayer oscillations. Reproduced from Ref. 19.

expressed in atomic layers (AL) and measured from the wetting layer (not from the substrate). In this case, the step height between $N = 5$ and $N = 6$ is clearly larger than that between $N = 6$ and $N = 7$. The deviation of the total island height from the ideal is shown in Fig. 1.1(b), which indicates the presence of bilayer oscillations in the film thickness as a function of N. Furthermore, the magnitude of these oscillations is surprisingly large, 0.4–0.8 Å. These bilayer oscillations were correlated with the electronic structure of the islands using scanning tunneling spectroscopy.

The STM study provides tantalizing evidence of some sort of structural distortion due to QSE; however, since it used a scanning probe technique, only the top surface of the islands could be probed, with no information on the internal lattice structure or buried interface available. In Chapter 5, an attempt to observe and understand this effect is undertaken using SXRD, which probes all the atomic layers in the film on equal footing since the penetration length of the x rays is much greater than the film thickness. Since the structural distortions are specifically indicated to vary for different island heights or film thicknesses, the morphology of the film must be as uniform as possible for a SXRD study to be successful. Fortunately, it was found that smooth, closed films could be grown if the substrates are properly pretreated and the growth temperature is low enough (∼110 K). By studying smooth films of near-atomic uniformity, the film morphology is greatly simplified and a study of the vertical lattice distortions is possible.

The experimental analysis in Chapter 5 indeed indicates the presence of

3

strong lattice distortions in the Pb films. However, the structural effects are found to be much more complicated than those originally observed in the STM study. Not only are oscillations in total film thickness observed with a bilayer (quasibilayer, actually) periodicity, but lattice distortions are also found *within* each film that are linked to QSE. This connection is explicitly made via the theoretical models developed in Chapter 4. The internal lattice distortions in the films also have a quasibilayer periodicity and are primarily near the film surface and the buried film-substrate interface. These distortions dampen away from the film boundaries in a manner very similar to the Friedel oscillations in the electronic charge density present at the surface of a bulk-truncated metal [51]. The variations in total film thickness observed are similar to those shown in Fig. 1.1(b) but are shown to be primarily a secondary result of more complicated structural distortions present in the layer structure of the film.

1.3 The Preferred or "Magic" Thickness Effect

The other frames in Fig. 1.1(a) show subsequent images of the same Pb island taken after a short period of time, which show that the $N = 6$ portions of the island tend to disappear in favor of $N = 5$ or $N = 7$ thicknesses. This behavior would seem to indicate that the $N = 6$ height is less stable than the other two terrace heights. This fact is confirmed by other x-ray diffraction, STM, and low-energy electron diffraction (LEED) studies [21–26], which have found that the morphology of Pb films grown on Si substrates at temperatures of 150–200 K consists of flat-topped, steep-sided islands of preferred heights. An example of this morphology is shown in Fig. 1.2(a), with a height histogram of the image shown in Fig. 1.2(b). Under the proper conditions, surfaces with islands mostly of a single uniform height can be prepared [22–28]. For this reason, such island heights are often called "magic" heights (thicknesses). The origin of this effect has been attributed to QSE, where electronic contributions to the surface energy of the films or islands result in local minima for certain thicknesses that cause those thicknesses to be more stable than others. In some cases, this effect can be quite dramatic, enabling the growth of unusually stable atomically-uniform films with the magic thickness [28, 44, 45].

More generally, electronic contributions cause oscillations in the surface energy as a function of thickness. This effect is examined theoretically in Chapter 4 in the context of a free-electron gas confined to a quantum well. In the case of Pb films, the oscillations due to QSE have a quasibilayer peri-
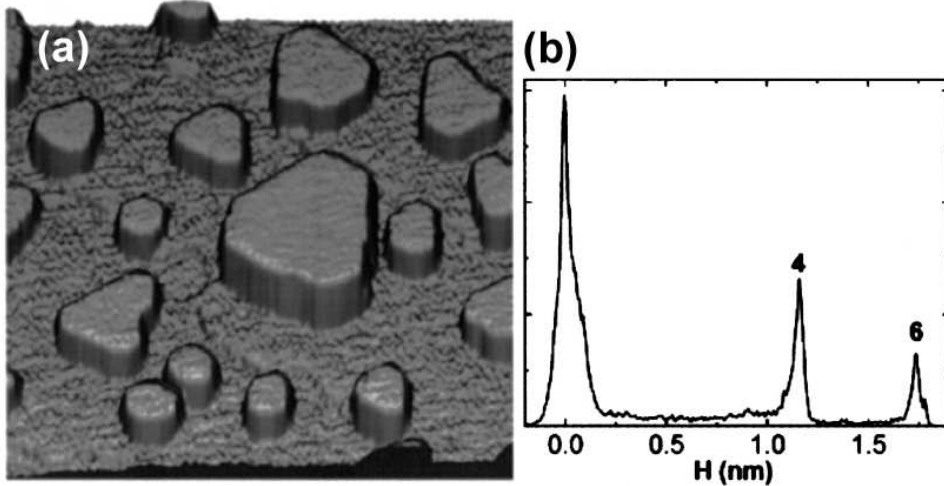
Figure 1.2: (a) A 200 nm×200 nm STM image of islands grown at 200 K showing the flat-topped, steep-sided morphology. (b) A histogram showing that the islands are overwhelmingly of heights 4 AL and 6 AL above a reference height of 2 AL. Reproduced from Ref. 25.

odicity which result in films with either even or odd numbers of atomic layers being preferred, with a cross-over between the two happening periodically following a regular superperiodic beating pattern. These quasibilayer oscillations have also been seen in first-principles calculations [26, 29, 41]. The results of some of these calculations are reproduced in Fig. 1.3. From this figure, the origin of the preferred thickness effect can be seen. The surface energy has a global minimum at $N = 1$, which corresponds to a wetting layer. A second deep local minimum can be seen at $N = 6$. For thicknesses between these two, the system can lower its overall energy by phase separating into surface regions with thicknesses of 1 and 6 AL, thereby resulting in the flat-topped islands observed in the microscopy studies. Note that the N values shown in Fig. 1.3 differ by 1 AL from those in Fig. 1.1 and by 2 AL from those in Fig. 1.2 since the latter two studies did not include the wetting layer in their thickness calculations. In the last case, there is also a diffuse lattice gas layer on top of the wetting layer that is also not included.

Thus, evidence of electronic effects for specific film thicknesses has been reported, but comprehensive empirical information on the surface energy over a broad range of thicknesses is lacking. The technique of x-ray diffraction is well-suited to provide such measurements since it both measures absolute film thicknesses and provides a statistical sampling over a macroscopic area. By preparing a sample that is near thermal equilibrium, a broad range of thicknesses can be present on the sample that reflects the local energy landscape of the system. The distribution of thicknesses can
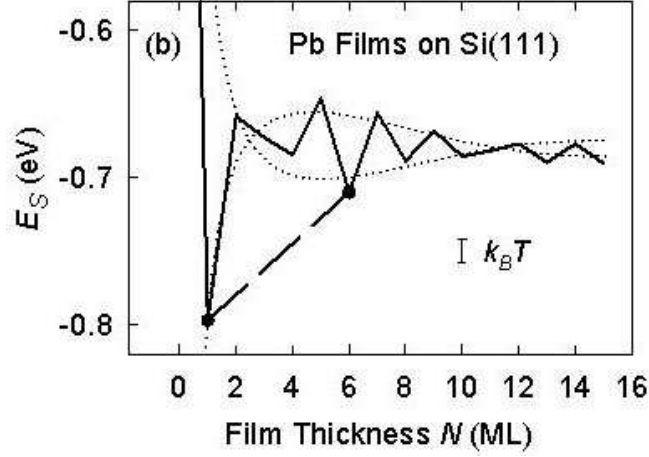
Figure 1.3: Results of first-principles calculations of a supported Pb/Si film showing quasibilayer oscillations in the surface energy. The local minimum at $N = 6$ results in a phase separation of films with thicknesses between 1 and 6 AL ($\equiv$ML) into uniform-height islands surrounded by a wetting layer. Reproduced from Ref. 26.

be measured using x-ray diffraction to obtain the relative film stability as a function of thickness, which is related to the surface energy. Such a study is presented in Chapter 6, where quantitative information on the surface energy of Pb/Si films is obtained over a broad range of thicknesses. The results are consistent with those from the theoretical model for the surface energy developed in Chapter 4 and with the first-principles calculations shown in Fig. 1.3. This study represents the first empirical measurements of QSE in the surface energy over a comprehensive range of thicknesses.

2 Surface X-Ray Diffraction

2.1 Introduction

This chapter is meant as a brief introduction to the technique of SXRD and the background needed to understand it. This technique can be used for many different purposes to obtain a wealth of information about the properties of a sample's surface, as described elsewhere in many different books and reviews [52–57]. However, since only a very narrow scope of these particular applications is relevant to the present work, only the background and theory needed to understand the subsequent chapters will be discussed in detail. In particular, only elastic scattering in the kinematic regime (no multiple scattering) will be considered. Due to the weak interaction of x rays with conventional condensed matter, this simplification is justified. That being said, there are a number of techniques that specifically capitalize on the information one can obtain from non-kinematic effects. However, since the experimental conditions in this study were specifically chosen to minimize such effects, they will not be discussed in detail.

In addition, although a wealth of three-dimensional information can be obtained from the examination of all the various crystal truncation rods, in this study only measurements of the specularly reflected intensity (specular rod) will be presented, which contains no contributions due to the in-plane order of the sample's atomic layers. In this manner, the out-of-plane order can be studied without the details of the lateral structure of the films influencing the data, effectively reducing the problem to one-dimension along the surface normal.

The chapter begins with an introduction to the concept of crystal lattices and the nomenclature used to describe them. Particular attention will be paid to the face-centered cubic (*fcc*) and diamond lattice structures since they are most relevant to the present work. Since we will be primarily interested in surfaces and quasi-2D films adsorbed to surfaces, a coordinate system based upon the symmetry and structure of a crystal surface will be introduced and its relationship to the bulk coordinate system explained. The basic phenomenon of diffraction will then be discussed, both from the

scalar Bragg viewpoint as well as the vectorial von Laue formulation. An important concept in the description of diffraction phenomena is the reciprocal lattice, which will be described and related to the real-space (direct) lattice of the crystal. After a brief discussion of the effects that surface reconstructions and lattice superperiodicities have on observed diffraction patterns, the formulas used to quantitatively describe the diffracted intensity from a crystalline sample are derived, along with a number of experimental correction factors that need to be taken into account. Finally, the specific equations for the extended reflectivity from Pb/Si(111) films are derived that will be used in the rest of the work to fit experimental data.

2.2 Crystal Lattices

2.2.1 The Unit Cell

A crystal by definition is a three-dimensional repetition of some identical configuration of atoms or molecules, called the unit cell. A crystal is constructed from its constituent unit cells like a 3D block composed of identical bricks, where each brick has the same relative distribution of atoms or molecules within itself. In the case of a crystal, the bricks can have any shape, as long as they are identical and fill up the entire crystal volume without any intervening spaces when stacked together. The regular manner in which the unit cells are repeated to make up the crystal can be described by three non-coplanar vectors called the *crystal axes*, which are conventionally denoted by the vectors $\mathbf{a}_1$, $\mathbf{a}_2$, and $\mathbf{a}_3$. If the unit cell is taken to have the form of a parallelepiped (which it can always be chosen to be), then these vectors describe the orientation and lengths of the three distinct edges of the unit cell.

There is no unique unit cell for any given crystal lattice or choice of crystal axes. However, there are two special types of unit cells that bear special attention. The first is called the *primitive unit cell*, which is a unit cell that contains the fewest number of atoms possible while still by itself describing the crystal structure. However, the primitive unit cell is not always the most convenient to work with and sometimes by using a larger unit cell (and hence not primitive), it can be chosen to be a nice symmetric shape (e.g., a cube). This second type of unit cell is called the *conventional unit cell*. Note that to conserve the volume of the crystal, the physical volume of the conventional unit cell must be equal to an integer times the volume of the primitive unit cell. The conventional unit cell will also have a
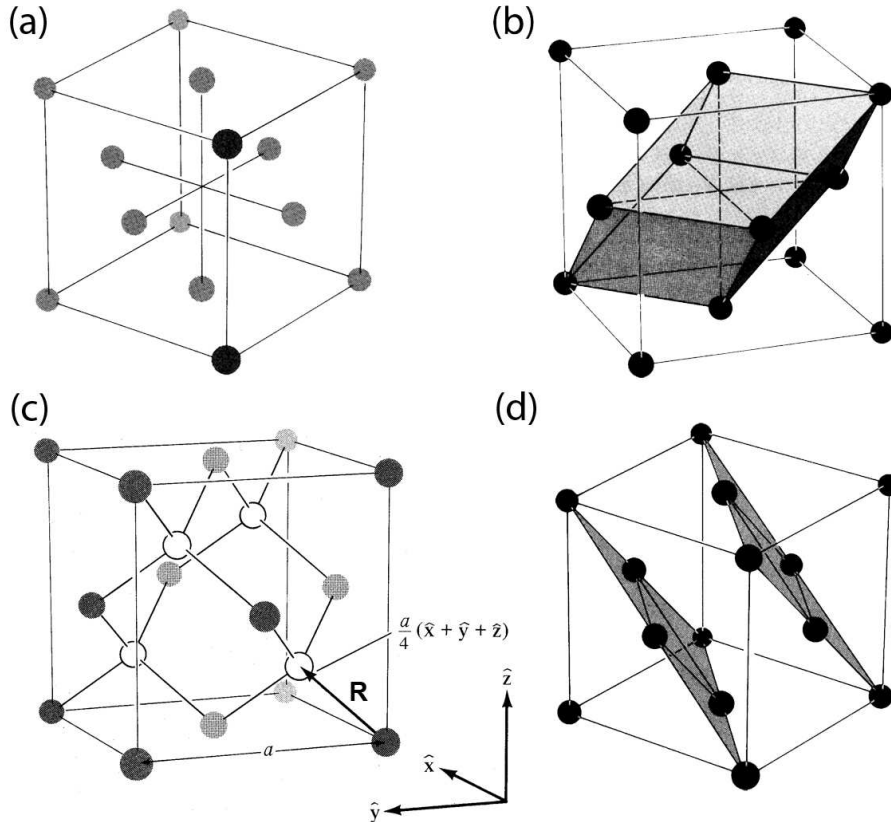
Figure 2.1: (a) The structure of the *fcc* conventional unit cell. (b) A primitive unit cell is shown as a shaded parallelepiped, which has a one-atom basis. (c) The diamond lattice, which is the same as a *fcc* lattice with a two-atom basis. The vector showing the relative position of the second atom in this basis is shown. (d) Some of the (111) planes of the *fcc* lattice. Adapted from Ref. 58.

correspondingly greater number of atoms contained within it. In general, if a unit cell contains more than one atom or molecule in it, the configuration of the individual constituents (i.e., their relative positions) throughout the unit cell is called a *basis*. The distinctions between these terms will become clearer with the examples outlined below.

In this work, we will be primarily concerned only with Si, which has a diamond lattice structure, and Pb, whose lattice structure is face-centered-cubic (*fcc*). Since the diamond structure is a special case of the *fcc* lattice, we will for now concentrate on the latter. The atomic arrangement of a *fcc* lattice is shown in Fig. 2.1(a). The conventional unit cell for this lattice consists of a cube with atoms positioned at each of the corners and in the middle of each face of the cube. The *fcc* conventional unit cell is *not* a primitive unit cell. A primitive unit cell for the *fcc* lattice is shown in Fig. 2.1(b) as a shaded region. It can be seen that this unit cell is primitive by displac-

9

ing the parallelepiped slightly along one of its diagonals and noticing that it then encompasses only one atom. In contrast, if one displaces the conventional unit cell (the cube) along one of its diagonals, it becomes evident that it contains four atoms — one corner atom and three of the face-centered atoms. As such, it can be inferred that the volume of the conventional unit cell is four times that of the primitive unit cell. The lattice constant of a *fcc* material denotes the length of one edge of the cube of the conventional unit cell. In the case of Pb, this constant is $a_{\mathrm{Pb}} = 4.92$ Å at 110 K.

The diamond lattice is a variant of the *fcc* lattice where the primitive unit cell has a two-atom basis. That is, the local surroundings of the two atoms in the basis are different and thus must both be included in the primitive unit cell. The structure of the diamond conventional unit cell is shown in Fig. 2.1(c). The additional atoms are shown as white circles to distinguish them from the normal *fcc* positions. In addition, the vector pointing to the second atom in the basis is shown. That is, the basis can be described as having one atom at the origin and the other located at the vector position $\mathbf{R} = \frac{1}{4}(\mathbf{a}_1 + \mathbf{a}_2 + \mathbf{a}_3)$ (where $\mathbf{a}_1 = a\hat{\mathbf{x}}$, $\mathbf{a}_2 = a\hat{\mathbf{y}}$, and $\mathbf{a}_3 = a\hat{\mathbf{z}}$ are the crystal axes for the conventional unit cell). Under careful inspection, one will notice that all of the white circles in the diagram lie at this vector position with relation to one of the *fcc* positions, and that every *fcc* atom has a corresponding white atom companion (not all are visible in the figure). The diamond lattice can thus be considered to be two interpenetrating *fcc* lattices, with one displaced by $\mathbf{R}$ with respect to the other. As with the *fcc* lattice, the lattice parameter quoted for a material with a diamond lattice structure corresponds to the length of one edge of the cube of the conventional unit cell ($a_{\mathrm{Si}} = 5.43$ Å at 110 K).

2.2.2 Miller Indices and Crystal Planes

Vectors composed of combinations of the crystal axes can be used to denote different directions and atomic planes with respect to the crystal structure. The coefficients of the three crystal axes are called the Miller indices. Specifically, a direction is notated with square brackets and the three Miller indices. By convention, these indices are usually chosen to be integers and negative numbers are notated with a bar ($\bar{1} = -1$). For example, [100] is equivalent to $\mathbf{a}_1$, whereas [$2\bar{1}0$] denotes the direction $2\mathbf{a}_1 - \mathbf{a}_2$. Similarly, a crystallographic plane of the crystal is denoted with the vector normal to the plane. In this case, the Miller indices are placed in round braces — e.g., (110) denotes the plane whose normal lies along the [110] direction. Thus,
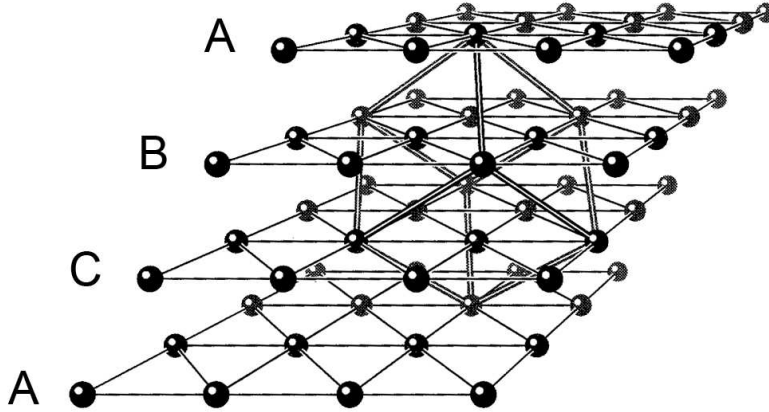
Figure 2.2: The (111) planes of the *fcc* lattice form a close-packed stacking sequence with three distinct in-plane arrangements relative to one another that stack $ABCABCABC\ldots$. The conventional unit cell is also shown. Adapted from Ref. 59.

when one refers to the (111) surface of a crystal, they are speaking of a crystal facet whose exposed surface is the (111) crystallographic plane. By its nature, a crystal possesses certain rotational and inversion symmetries. As such, certain directions and crystallographic planes will be symmetrically equivalent to one another. For example, in the case of a cubic system, the [100], [010], and [001] directions are all equivalent since they are all related by a symmetry operation (rotation by 90° in this case) allowed by the crystal structure.

In our case, the substrates used were single-crystal Si(111) wafers, meaning the top polished surface of the wafer is nominally the (111) crystallographic plane. When Pb is thermally evaporated on these substrates (see Sec. 3.5.1), the films form with a (111)-oriented crystalline structure. The (111) planes of a *fcc* material are shown in Fig. 2.1(d) with respect the conventional unit cell. Since Pb is a *fcc* material, each atomic layer of Pb on the Si substrate has the structure of one of these Pb(111) planes. However, as is evident in Fig. 2.1(d), three of these planes occur in every unit cell (there will be an additional one at either the top-right or bottom-left corner, which must be included). If these three planes are stacked one on top of the other, it can be seen that they have different arrangements of atoms relative to one another, as shown in Fig. 2.2. Specifically, each individual plane forms a triangular net of atoms. However, when the planes are stacked, they are not placed one on top of the other, but are offset slightly so that the atoms stack closely together. For this reason, the *fcc* lattice is often called cubic close-packed, since it represents the densest manner in which spheres
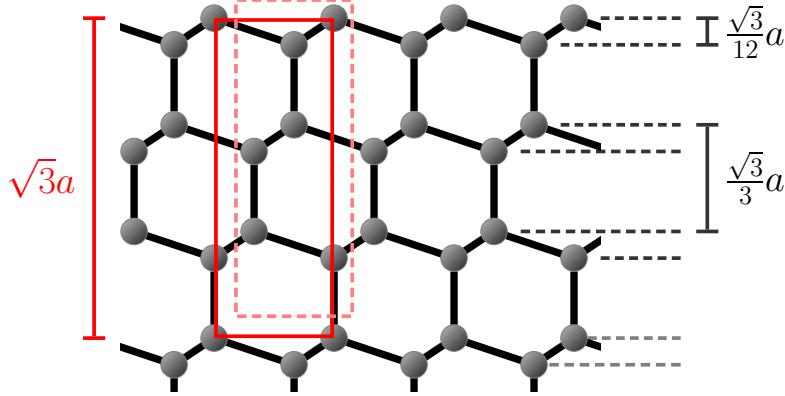
Figure 2.3: The (111) planes of the diamond lattice form three sets of bilayers per unit cell with the interlayer spacings shown. The unit cell in the surface (hexagonal) coordinate system is shown with a solid red box. By displacing the box slightly (dashed box) it is clear that this choice of unit cell contains six atoms, compared to eight in the conventional unit cell.

can be packed together into a 3D structure.* Every third stacking plane has an identical orientation and relative lateral displacement, resulting in an $ABCABCABC...$ stacking order. There exist alternative close-packed structures that have a similar hexagonal (or triangular) nets of atoms in each plane but that have a different stacking order. For example, the hexagonal close-packed (hcp) lattice has the stacking order $ABABAB....$ Such structures represent independent crystal lattices, though, which are distinct from the *fcc* lattice of Pb.

Since the *fcc* unit cell has a length of $a\sqrt{3}$ along the [111] direction, the interlayer spacing between the atomic layers of a *fcc* material in this direction is $a\frac{\sqrt{3}}{3}$. In contrast, the diamond lattice consists of two interpenetrating *fcc* lattices, with one displaced from the other by the vector $\frac{1}{4}(\mathbf{a}_1 + \mathbf{a}_2 + \mathbf{a}_3)$, which is equivalent to $\frac{1}{4}$ of the unit cell length in the [111] direction. Thus, the atomic layer structure of (111) planes in a diamond structure is the same as the $fcc(111)$ structure with an additional atom directly above each of the $fcc(111)$ planes a distance of $a\frac{\sqrt{3}}{4}$, which places it a distance of $a\frac{\sqrt{3}}{12}$ below the next $fcc(111)$ plane above it. The layer structure thus consists of three sets of bilayers, each consisting of two layers separated by $a\frac{\sqrt{3}}{12}$ and with the interbilayer distance being $a\frac{\sqrt{3}}{3}$. A cross-section of this layer structure is shown in Fig. 2.3. Due to the bilayer structure of the atomic planes in the [111] direction, there are two possibilities for truncation of the surface:

---

*Next time you buy oranges at the grocery store, notice how they are stacked (if they are stacked at all). Although they likely are not aware of it, an attentive grocer will stack spherical produce in $fcc(111)$ planes since it is the most efficient method of packing the product on the shelf and forms a nice pyramidal structure.
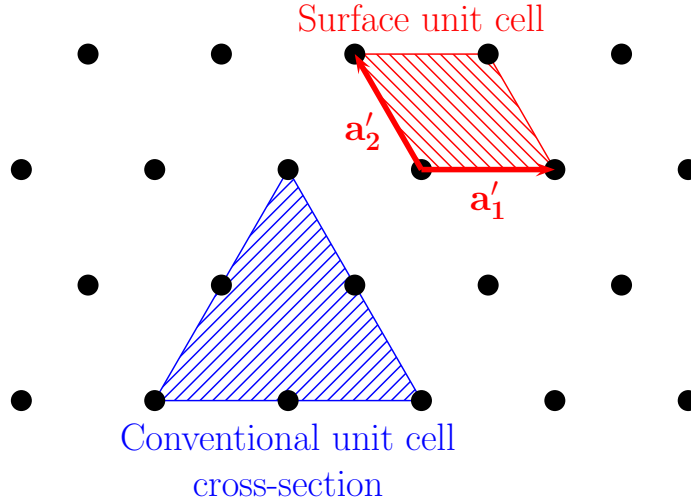
Figure 2.4: The $fcc(111)$ surface consists of a hexagonal net of atoms. The crystal axes and unit cell for the surface coordinate system are shown. The third crystal axis is pointed out of the paper and is parallel to the surface normal.

either between the bilayers or in the middle of a bilayer. In the case of Si, it has been experimentally verified that the Si(111) surface is terminated between the bilayers, as shown in Fig. 2.3 [60].

2.2.3 Surface Coordinates

When working with the surface of a crystal, it is not always convenient to work in the framework of the conventional unit cell, particularly if none of the crystal axes coincides with the surface normal. In that case a different set of crystal axes is generally chosen such that $\mathbf{a}'_3$ is nominally normal to the surface and $\mathbf{a}'_1$ and $\mathbf{a}'_2$ lie in the plane of the surface. Since this coordinate system is different from the conventional one, it is necessary to be able to translate any results specified with the surface coordinates to the conventional coordinates, which can be accomplished with a standard coordinate transformation. For our purposes, though, since only reflectivity measurements will be discussed, the full transformation matrix is not needed. For the interested reader, its derivation is covered in other works [56, 61].

In the case of a material with a fcc (or diamond) lattice, the (111) planes in the unit cell form a hexagonal (triangular) net, as can be seen in Fig. 2.2. This 2D net has been reproduced in Fig. 2.4 along with a cross-section of the conventional unit cell shown in blue. This cross-section is equivalent to those shown in Fig. 2.1(d). The surface normal is in the [111] direction, so

the third crystal axis in the surface coordinate system is

$$\mathbf{a}_3' = \mathbf{a}_1 + \mathbf{a}_2 + \mathbf{a}_3. \tag{2.1}$$

The standard choice for the in-plane crystal axes is shown with red arrows in Fig. 2.4 along with the surface unit cell defined thereby. By noting that the distance between neighboring atoms in the (111) surface corresponds to half of the diagonal of one of the cubic faces of the conventional unit cell [see Fig. 2.1(d)], it should be clear that both of the lengths of each of these surface crystal axes is $\frac{\sqrt{2}}{2}a$. Specifically, these vectors are [61]

$$\mathbf{a}_1' = \frac{1}{2}(\mathbf{a}_1 - \mathbf{a}_2)$$
$$\mathbf{a}_2' = \frac{1}{2}(\mathbf{a}_2 - \mathbf{a}_3). \tag{2.2}$$

Thus, the area of the surface unit cell is $A_{\text{cell}} = \frac{\sqrt{3}}{4}a^2$. From Eq. (2.1), the length of the third crystal axis is $\sqrt{3}a$. Thus, the volume of the unit cell in the surface coordinate system is $\frac{3}{4}$ of the volume of the conventional unit cell. In the case of a *fcc* lattice, this means that the surface unit cell volume encompasses three atoms (compared to the four encompassed by the conventional unit cell volume, as discussed in Sec. 2.2.1). In the case of a diamond lattice, this means the surface unit cell volume encompasses six atoms, as is evident in Fig. 2.3.

2.3 Diffraction and the Reciprocal Lattice

2.3.1 Bragg Reflections

The phenomenon of x-ray diffraction arises from the coherent interaction of electromagnetic waves scattered from a periodic collection of molecules or atoms in a crystal lattice. X rays are used because their wavelength is on the order of the interatomic spacing between the atomic constituents of a solid. Of all the scattered waves, only those scattered elastically will interfere coherently. Inelastically scattered waves generally all have different wavelengths and thus contribute to a diffuse incoherent background. The elastically scattered waves all have the wavelength of the incident radiation, but have different phases based upon the differences in path lengths between the scattering elements in the crystal. Diffraction arises when the scattered waves from all (or a macroscopic fraction, anyway) of the atoms in the crystal have the same phase. There are two historical perspectives to this
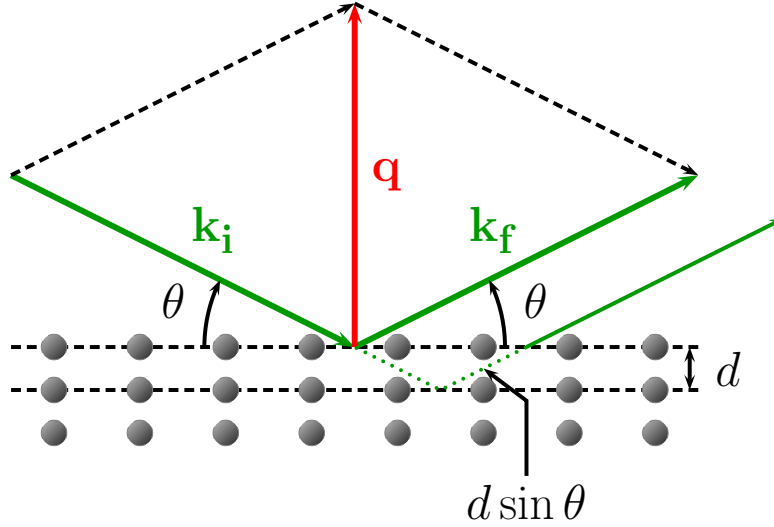
Figure 2.5: In the Bragg formalism, x rays reflect specularly from crystallographic planes in the crystal. When x rays reflected from different parallel planes add constructively, one sees a Bragg reflection. The angle θ at which such a reflection occurs is called the Bragg angle. Such a reflection can also be described with the momentum transfer vector $\mathbf{q}$ in the Laue formalism, in which case the condition for observing a Bragg reflection is when the momentum transfer vector points to a reciprocal lattice point.

phenomenon of diffraction. Both are equally valid and in fact equivalent, but approach it from a slightly different viewpoint.

The viewpoint of Bragg diffraction is based on three assumptions:

Assumption #1. A crystal can be decomposed into parallel lattice planes with regular interplanar spacings, denoted by d.

Assumption #2. X rays are specularly reflected from these crystallographic planes like light from a mirror.

Assumption #3. At specific angles of reflection, the reflected x rays interfere constructively and produce a diffracted beam. These angles with respect to the crystal planes are called *Bragg angles*.

This formulation is illustrated in Fig. 2.5, where three successive planes of atoms in a crystal are shown that have an interplanar spacing of d. The incident plane-wave x-rays make an angle θ with the planes of the crystal and are reflected specularly. The path length difference between the x rays reflected from the top atomic plane and the one below it is $2d\sin\theta$. For these waves to interfere constructively, this path length difference must be equal to an integer number of x-ray wavelengths. Thus, in the Bragg formulation,

the condition for diffraction is

$$2d \sin \theta = n\lambda, \quad\quad\quad (2.3)$$

where n is an integer and the angles θ satisfying this relation are called *Bragg angles*. This equation is called Bragg's Law.

The atomic planes shown in Fig. 2.5 are not necessarily those at the surface of a crystal. Since x rays interact weakly with matter and thus have a long penetration length, the planes shown in the schematic are surrogates for any possible crystallographic planes in the crystal. This implies that a Bragg reflection can be found for every conceivable combination of three coplanar points in the crystal lattice. These crystallographic planes can be described in terms of the crystal axes defined in Sec. 2.2. Specifically, each plane can be assigned a set of integer Miller indices HKL. By the crystallographic planes HKL, we mean a set of atomic planes, one of which passes through the origin and whose nearest neighboring plane passes through the three points at $\frac{1}{H}\mathbf{a}_1$, $\frac{1}{K}\mathbf{a}_2$, and $\frac{1}{L}\mathbf{a}_3$ [56]. The interlayer spacing is then related to these vectors as

$$d = \frac{\mathbf{a}_1}{H} \cdot \hat{\mathbf{n}} = \frac{\mathbf{a}_2}{K} \cdot \hat{\mathbf{n}} = \frac{\mathbf{a}_3}{L} \cdot \hat{\mathbf{n}} \quad\quad\quad (2.4)$$

where $\hat{\mathbf{n}}$ is the unit vector normal to the HKL planes.

2.3.2   The von Laue Formalism

The von Laue formulation of x-ray diffraction concentrates more on the momentum transfer vector,

$$\mathbf{q} \equiv \mathbf{k}_f - \mathbf{k}_i, \quad\quad\quad (2.5)$$

where the wave vectors $\mathbf{k}_i$ and $\mathbf{k}_f$ indicate the directions of the incoming and diffracted x rays and whose magnitudes are $k = 2\pi/\lambda$. The momentum transfer vector is shown in Fig. 2.5 with a red arrow. Since $|\mathbf{k}_i| = |\mathbf{k}_f| = k$ for elastically scattered x rays, the magnitude of this vector is $q = 2k \sin \theta$. Thus, Bragg's Law can be rewritten as

$$q = \frac{2\pi n}{d}. \qu\quad\quad\quad (2.6)$$

In addition, due to Assumption #2 on page 15, $\mathbf{q}$ is also normal to the crystallographic planes responsible for the diffracted beam in the Bragg formalism. Thus, every set of atomic planes in the crystal can be characterized by a vector whose direction is normal to the planes and whose magnitude

is proportional to the reciprocal of their interplanar spacing in the crystal. Specifically, the unit normal vector in Eqs. (2.4) can be taken to be $\hat{\mathbf{n}} = \mathbf{q}/q$. Together with Eqs. (2.6) and (2.4), this yields the *Laue conditions*

$$\mathbf{q} \cdot \mathbf{a}_1 = 2\pi H \tag{2.7a}$$

$$\mathbf{q} \cdot \mathbf{a}_2 = 2\pi K \tag{2.7b}$$

$$\mathbf{q} \cdot \mathbf{a}_3 = 2\pi L \tag{2.7c}$$

where by convention the integer n is absorbed into H, K, and L.

Thus, every Bragg reflection has a corresponding $\mathbf{q}$ vector. Since the dimensions of $\mathbf{q}$ are inverse-length, the mathematical space in which this vector resides is called *reciprocal space*. The structure of reciprocal space is complementary to that of the real space of the crystal. Specifically, if the basis vectors of reciprocal space are chosen such that they are orthogonal to two of the three crystal axes,

$$\mathbf{a}_i \cdot \mathbf{b}_j = 2\pi\delta_{ij}, \tag{2.8}$$

then the momentum transfer vector for the Bragg reflection corresponding to the crystallographic planes HKL can be conveniently written as

$$\mathbf{q} = H\mathbf{b}_1 + K\mathbf{b}_2 + L\mathbf{b}_3, \tag{2.9}$$

which by inspection can be seen to obey the Laue conditions, Eqs. (2.7).

The only basis vectors that obey the orthogonality relation, Eq. (2.8), are

$$\mathbf{b}_1 = 2\pi \frac{\mathbf{a}_2 \times \mathbf{a}_3}{\mathbf{a}_1 \cdot (\mathbf{a}_2 \times \mathbf{a}_3)} \tag{2.10a}$$

$$\mathbf{b}_2 = 2\pi \frac{\mathbf{a}_3 \times \mathbf{a}_1}{\mathbf{a}_1 \cdot (\mathbf{a}_2 \times \mathbf{a}_3)} \tag{2.10b}$$

$$\mathbf{b}_3 = 2\pi \frac{\mathbf{a}_1 \times \mathbf{a}_2}{\mathbf{a}_1 \cdot (\mathbf{a}_2 \times \mathbf{a}_3)}, \tag{2.10c}$$

which can be seen from the following example. To construct the basis vector $\mathbf{b}_1$, one first notes that to be orthogonal to both $\mathbf{a}_2$ and $\mathbf{a}_3$, it must be parallel to $\mathbf{a}_2 \times \mathbf{a}_3$. The magnitude of this cross product is the area of the unit cell facet spanned by the vectors $\mathbf{a}_2$ and $\mathbf{a}_3$. By Eq. (2.8), the magnitude of $\mathbf{b}_1$ must be inversely proportional to the length of $\mathbf{a}_1$ projected onto the vector $\mathbf{a}_2 \times \mathbf{a}_3$, which is just the "height" of the parallelepiped defined by the three crystal axes. Thus, the proper quantity with which to normalize

Unit Cell Type	Selection Rule (Allowed Reflections)
Primitive (Simple)	Any H, K, L
Body Centered	$H + K + L = 2n$
Face Centered	H, K, L all odd or H, K, L all even
Diamond (fcc + 2-atom basis)	H, K, L all odd or H, K, L all even and $H + K + L = 4n$
Hexagonal Close-Packed	L even or $H + 2K \neq 3n$

Table 2.1: Selection rules for common types of crystal lattices. In all cases, n is any integer and H, K, L refer to the bulk-indexed Miller indices of a Bragg reflection.

$\mathbf{b}_1$ is $\mathbf{a}_1 \cdot (\mathbf{a}_2 \times \mathbf{a}_3)$, the volume of the unit cell. This yields the definition of $\mathbf{b}_1$ given by Eq. (2.10a). A similar procedure can be followed for $\mathbf{b}_2$ and $\mathbf{b}_3$.

The Laue conditions thus describe a 3D lattice of points in reciprocal space, each of which corresponds to a $\mathbf{q}$ vector for a Bragg reflection. These points are called *Bragg points* and the lattice formed by these points in reciprocal space is called the *reciprocal lattice*. In the case where the crystal axes describe a unit cell with a one-atom basis (such as the simple cubic lattice, for instance), every possible combination of integers HKL corresponds to a Bragg peak. However, if the conventional unit cell has multiple identical atoms in its basis then some HKL combinations may not refer to allowed Bragg peaks and are thus termed "forbidden." This idea can be understood qualitatively as follows.[†] Consider for example the *fcc* conventional unit cell [Fig. 2.1(a)], which has a four-atom basis. Since the reciprocal lattice has the inverse properties of the direct (crystal) lattice, the packing of more atoms into the real-space unit cell (i.e., denser lattice points) means that the reciprocal space unit cell must have fewer points in it. That is, not every unit cell in reciprocal space, as defined by the basis vectors $\mathbf{b}_j$, will have a valid Bragg point in it. The rules by which one determines which points in the reciprocal lattice correspond to "allowed" Bragg reflections and which are forbidden are called selection rules. The selection rules for some basic unit cell types are shown in Table 2.1. For instance, the simple cubic lattice has no forbidden reflections; whereas for the *fcc* lattice, whose conventional unit cell is a cube with a basis, only reflections where all the Miller indices are either even or odd integers are allowed.

[†]The selection rules for determining which peaks are allowed or forbidden can also be determined analytically by constructing the structure factor for the unit cell (Sec. 2.5). See for example, pp. 125–129 in Ref. 55.

The selection rules are the result of an additional symmetry in the crystal lattice that is not represented in the conventional unit cell. If this additional symmetry is broken in some way — e.g., if some of the atoms in the basis are not identical, or they are displaced from their ideal positions — then the selection rules will not necessarily apply. That is, the *fcc* conventional unit cell has four atoms in it. If these atoms are all identical, then the selection rule (H, K, and L must be all odd or all even) applies. However, if one or more of these atoms is different in some way, then the selection rule may be broken. Similarly, if a material has a unit cell that has additional atoms in its basis, then additional selection rules may apply. For instance, for a diamond lattice, which is a special version of the *fcc* lattice with twice as many atoms per unit cell (the primitive unit cell has a two-atom basis), all the selection rules of *fcc* apply, plus the additional one that even if H, K, and L are all even, unless they add up to $4n$ the peak is forbidden.

2.4   Reconstructions and Superperiodicities

In the last section, the inverse nature of the reciprocal lattice was discussed in the context of selection rules. There it was found that if the conventional unit cell in real space is larger than the primitive unit cell, then there must be correspondingly fewer allowed reflections in reciprocal space. That is, a higher density of lattice points in real space translates to a lower density of lattice points in reciprocal space. This discussion all took place within the context of bulk crystal lattices. The structure of a crystal surface can deviate significantly from the structure of the bulk, though, and truncation of the crystal structure often results in dangling bonds that cause a rearrangement of the surface atoms into a superstructural configuration. Such a phenomenon is known as *surface reconstruction*.

As an example of this effect, consider a crystal surface whose bulk truncation would result in a square lattice of atoms. The direct (real-space) and reciprocal lattice along with the respective basis vectors in the surface coordinate system are shown in the top portion of Fig. 2.6. Depending on the details of the atomic structure of the crystal near the surface, the system may be able to reduce its surface energy slightly by shifting every other row of atoms a minute amount in alternating directions, as shown in the bottom portion of the figure. The surface in this case has formed a 2×1 reconstruction since the surface unit cell has effectively doubled its size in the $\mathbf{a}_1'$ direction.

In Sec. 2.3 it was found that the magnitude of $\mathbf{b}_1$ is proportional to
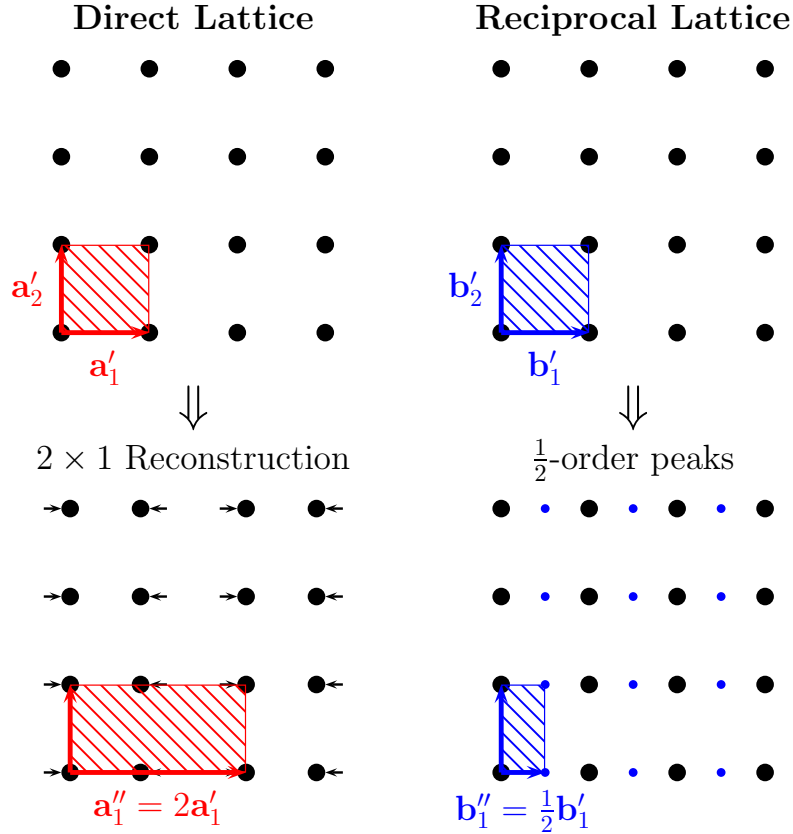
Figure 2.6: Illustration of a surface reconstruction. In this case, simple truncation of the crystal would result in a square lattice of atoms. The reciprocal lattice also thus consists of a square lattice of points. However, the lowest-energy configuration of the surface atoms may be such that they form a superstructure, in this case a 2×1 reconstruction. This effectively changes the size of the surface unit cell, resulting in corresponding superstructure peaks in reciprocal space.

$1/|\mathbf{a}_1|$; thus, an expansion of the effective real space unit cell by a factor of two must be accompanied by a shrinkage of the reciprocal space unit cell by a factor of two. This will result in *superstructure peaks* being found at fractional-order positions in reciprocal space (they are fractionally-ordered with respect to the original basis vectors, which are still used for indexing purposes). This effect is illustrated in the bottom portion of Fig. 2.6. In practice, since the shifts in atomic positions that cause the reconstruction are usually only very slight, the superstructure peaks are in general much weaker in intensity than the other peaks.

Although in this example it was assumed that the atoms that form the reconstruction are the surface atoms of a bulk-truncated crystal, such surface reconstructions can also be induced by one or more layers of adsorbate being deposited onto the crystal surface. The effects on the diffraction patterns

observed are similar to those described above with the additional complication that the superstructure formed by the adsorbate atoms may be either commensurate or incommensurate with the atomic lattice of the crystal surface. In the former case, the diffraction features of the adsorbate layer(s) will combine with those due to the underlying crystal lattice and interference between the scattered waves from the two may occur. In the latter case, the adsorbed atoms may form their own independent lattice and/or superstructure that usually have some orientational relationship to the lattice of the underlying crystal surface, even if they do not share the same periodicity. The diffracted waves from the adsorbate atoms will in general not interfere with those from the underlying substrate in this case, with a notable exception being the case of the reflectivity, which always contains contributions from all the surface layers, regardless of their in-plane orientations. The reflectivity will be discussed in Secs. 2.5 and 2.6.

The superstructure that is formed by a surface reconstruction, like the one described above, extends in two dimensions in the plane of the crystal surface. As will be seen in Chapter 5, it is also possible for the structure of a crystal surface or film to have a superperiodic structure along the direction normal to the surface of the sample. For instance, bilayer oscillations in the interlayer spacings of the atomic layers of a film will have much the same effect as the 2×1 reconstruction shown in Fig. 2.6, except that since the superperiodicity lies in the direction of $\mathbf{a}'_3$, the superstructure peaks will show up in the $\mathbf{b}'_3$ direction in reciprocal space instead of in the $\mathbf{b}'_1$ direction. Conceptually, though, the two effects are analogous — a superperiodicity in the real space lattice results in fractional-order diffraction features in reciprocal space.

2.5 Calculation of the Scattered Intensity

2.5.1 The Structure Factor

Since x rays are wavelike in nature, the scattered intensity from a collection of particles is calculated by first summing the amplitudes of the waves from each individual particle. Once the total amplitude is known, its square modulus is proportional to the measured intensity. The first step in calculating the scattered amplitude is to consider a single charged particle. The expression for the cross-section of a charged particle for scattering electromagnetic

radiation is given by the Thomson formula [62]

$$\frac{d\sigma}{d\Omega} = P \left(\frac{e^2}{4\pi\epsilon_0 mc^2} \right)^2, \tag{2.11}$$

where P is a polarization factor and m is the mass of the scatterer. Since the mass of an electron is more than three orders of magnitude smaller than the mass of a proton, less than $1/10^6$ of the measured signal will be due to scattering from the protons in the nucleus; thus, it will be subsequently assumed that the measured intensity is solely due to scattering from electrons. In that case, this formula can be rewritten as

$$\frac{d\sigma}{d\Omega} = P r_0^2 \tag{2.12}$$

where $r_0 = \frac{e^2}{4\pi\epsilon_0 m_e c^2} = 1.617 \times 10^{-5}$ Å is called the Thomson scattering length. The Thomson formula is classical in nature, which in principle is subject to corrections due to the quantum mechanical nature of the photon and scatterer. In particular, when the momenta of the incident and scattered photons are different, contributions due to inelastic scattering will occur. Such scattering can either be due to recoil of the electron, in which case it is termed Compton scattering, or in the case of an electron bound to an atomic nucleus, due to the electron making a transition to an excited state of the atom. Compton scattering is diffuse in nature and for our purposes can be considered part of the background that is subtracted from the data. In the case of atomic transitions, as long as the incident x-ray energy is far from any absorption edges of the material,[‡] the corrections due to such effects are negligible. Therefore, for our purposes, the Thomson formula is an accurate reflection of the electromagnetic cross-section of an electron.

The amplitude of a photon scattered from an electron at position $\mathbf{r}$ with respect to the origin is then

$$\mathcal{A}_1 = \mathcal{A}_0 r_0 \frac{1}{R_0} e^{i\mathbf{q}\cdot\mathbf{r}}, \tag{2.13}$$

where $\mathcal{A}_0$ is the amplitude of the incoming plane wave and the factor of $1/R_0$ arises from the spherical nature of the scattered wave. The polarization factor has been left out for the time being and will be reintroduced in Sec. 2.5.4. The phase factor of $e^{i\mathbf{q}\cdot\mathbf{r}}$ is due to the electron not being located at the origin. That is, relative to a wave scattered from the origin, the pho-

---

[‡]In the field of x-ray diffraction, the energies at which atomic transitions occur are commonly referred to as absorption edges due to the enormous jump in the absorption cross-section of the atom at these energies.
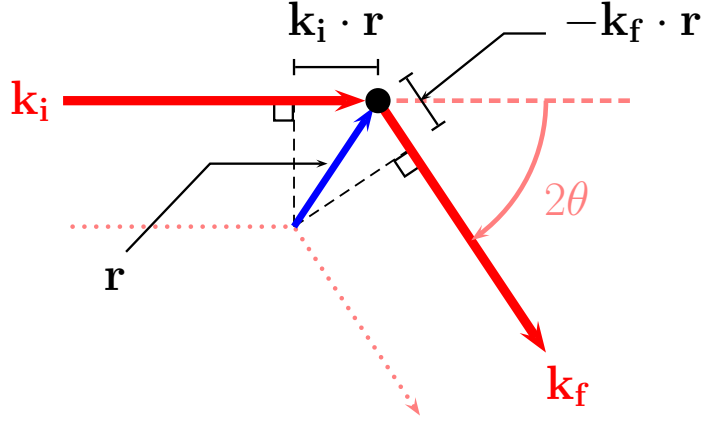
Figure 2.7: The geometry for scattering from a single electron. The scattered wave picks up a phase of $(\mathbf{k}_i - \mathbf{k}_f) \cdot \mathbf{r}$ relative to a wave scattered from the origin. The scattering angle 2θ is defined as the angle between the vectors $\mathbf{k}_i$ and $\mathbf{k}_f$.

ton picks up a phase shift of $\mathbf{k}_i \cdot \mathbf{r}$ along its incoming path and a phase shift of $-\mathbf{k}_f \cdot \mathbf{r}$ along its outgoing path, as shown in Fig. 2.7; hence, the total phase factor is $e^{-i(\mathbf{k}_i - \mathbf{k}_f) \cdot \mathbf{r}} = e^{i\mathbf{q} \cdot \mathbf{r}}$. This factor is arbitrary at the moment, since the origin is arbitrary; however, it will be of crucial importance when more than one electron is involved and the scattered waves from each particle interfere with one another. Note that since only elastic scattering will be considered, $|\mathbf{k}_f| = |\mathbf{k}_i| = k$ and the magnitude of the momentum transfer is

$$q = 2k \sin\left(\frac{2\theta}{2}\right), \qquad (2.14)$$

where 2θ is the *scattering angle*, defined as the angle between $\mathbf{k}_i$ and $\mathbf{k}_f$. As its notation suggests, the scattering angle is related to the Bragg angle introduced in Sec. 2.3; however, the scattering angle is a more generalized quantity that need not be related to a Bragg reflection *per se*. Indeed, we have yet to build a crystal lattice, without which diffraction cannot arise.

The amplitude from a collection of electrons located at positions $\mathbf{r}_j$ is just the sum of those from each individual scatterer, taking into account their different phases,

$$\mathcal{A} = \mathcal{A}_0 r_0 \frac{1}{R_0} \sum_j e^{i\mathbf{q} \cdot \mathbf{r}_j}, \qquad (2.15)$$

where it has been assumed that the distance to the detector is much larger than the size of the sample volume illuminated by the incident beam; that is, $R_0 \gg |\mathbf{r}_j|$. The scattering from an atom is not simply the scattering from a collection of free electrons, though, so Eq. (2.15) must be generalized to

an integral

$$\mathcal{A}_{\text{atom}} = \mathcal{A}_0 r_0 \frac{1}{R_0} \int \rho(\mathbf{r}) e^{i\mathbf{q}\cdot\mathbf{r}} d^3\mathbf{r}, \qquad (2.16)$$

where the electron density, $\rho(\mathbf{r})$, is described by the quantum mechanical wave functions of the electrons surrounding the nucleus. In such an integral it is customary to consider the vector origin to be the center of the atom. The integral in Eq. (2.16) is called the *atomic scattering factor*

$$\boxed{f(q) = \int \rho(\mathbf{r}) e^{i\mathbf{q}\cdot\mathbf{r}} d^3\mathbf{r},} \qquad (2.17)$$

which is the Fourier transform of the electron density of the atom. For very small momentum transfers, the exponential factor approaches unity and $f(q) \to Z$, the number of electrons in the atom. In its most general treatment, $f(q)$ is a complex quantity dependent on the incident x-ray energy. If the x-ray energy is close to an atomic absorption edge, the Thomson formula no longer adequately describes the cross-section of the electrons in the atom and corrections are necessary. However, since the x-ray energies used in this study were specifically chosen to avoid any such absorption edges, no such corrections were made to the atomic scattering factors used. The value of the atomic scattering factor as a function of the momentum transfer is tabulated for virtually all of the elements of the periodic table [63]. In this work, the values used for the atomic scattering factor were obtained via a cubic spline interpolation of the tabulated values for the neutral atoms. Since the atomic scattering factor varies monotonically and only very slowly, such a scheme yields accurate results. An example of the atomic scattering factor is shown in Fig. 2.8 for Si, which shows the tabulated values as well as the interpolation curve used.

The atomic scattering factor is written in Eq. (2.17) as a function of the magnitude of $\mathbf{q}$ since it is almost always spherically symmetric, owing to the approximate spherical symmetry of the core electron density around most atoms. However, deviations from complete spherical symmetry can have important effects. Most notably, such asymmetries are responsible for violations of the selection rules for carbon (diamond), silicon, and germanium [64]. These materials all form a diamond lattice whose primitive unit cell is that of a *fcc* lattice with a two-atom basis. As discussed in Sec. 2.3, if the atoms in this basis are identical, an additional selection rule applies due to an additional symmetry in the crystal, as shown in Table 2.1. In the cases of carbon, silicon, and germanium, the atoms are identical but their orientations are slightly different. Since the electron density surrounding the

Si Atomic Scattering Factor
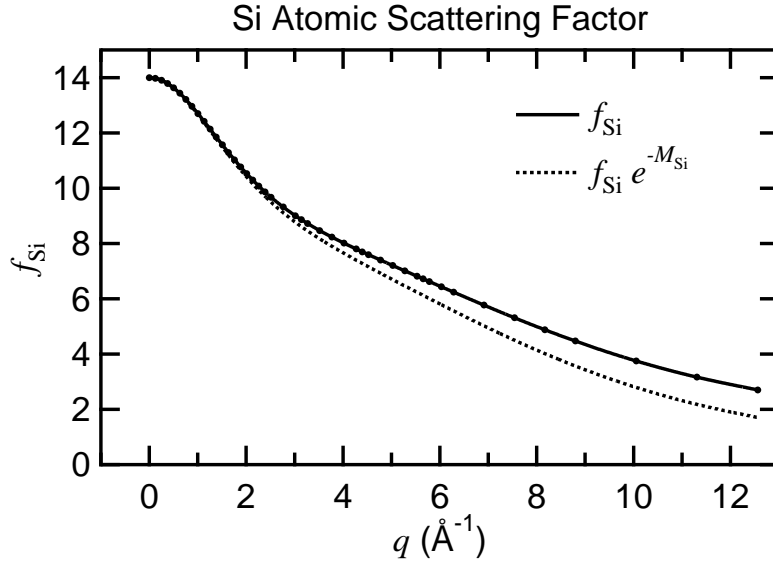
Figure 2.8: The atomic scattering factor for Si shown as a function of the momentum transfer. Also shown is the effect of taking temperature into account with the addition of a Debye-Waller factor. The points on the solid line show the tabulated values.

atoms is not exactly spherical, the symmetry that results in the additional selection rule (the even-indexed peaks with $H + K + L \neq 4n$ are forbidden in a diamond lattice but not in a *fcc* lattice) is broken. However, since the asymmetry is only very slight, these pseudo-forbidden peaks are extremely weak in comparison to the "true" Bragg peaks (those allowed for both a *fcc* and diamond lattice). As a result, the corrections due to this effect are usually negligible unless one happens to be measuring very near to one of the pseudo-forbidden peaks. In our case, the reflectivity profiles shown in Chapters 5 and 6 do scan over one of these peaks at $l = 6$, which corresponds to the Si(222) Bragg condition that would normally be forbidden $(2 + 2 + 2 \neq 4n)$ in a diamond lattice. Sharp peaks were indeed observed at this momentum transfer for all samples. In fact, the presence of the peak was usually a good indication that the sample was aligned properly, since it was weak enough to scan over, unlike the true Si Bragg peaks. Instead of introducing tedious corrections to the atomic scattering factor, though, these portions of the data, which usually consisted of only a few data points, were simply removed so as not to affect the analysis. An example of an extended x-ray reflectivity profile for which the Si(222) pseudo-Bragg peak has not been removed is shown in Fig. 3.8.

By extension of Eq. (2.15), the scattered amplitude from all the atoms

in the unit cell of a crystal is

$$\mathcal{A} = \mathcal{A}_0 r_0 \frac{1}{R_0} F(\mathbf{q}) \tag{2.18}$$

where

$$F(\mathbf{q}) = \sum_{j \in \text{cell}} f(q) e^{i\mathbf{q} \cdot \mathbf{R}_j} \tag{2.19}$$

is called the *structure factor*, since it describes the geometrical arrangement
of the atoms in the unit cell. The sum in this expression is over all the atoms
in the unit cell, each positioned at $\mathbf{R}_j$ with respect to the cell origin. Since
this arrangement is usually not spherically symmetric, $F(\mathbf{q})$ is in general
a function of the vector $\mathbf{q}$, unlike the atomic scattering factor. Just as the
atomic scattering factor is the Fourier transform of the electron density of an
atom, the structure factor is the Fourier transform of the electron density of
a crystal's unit cell. Since the unit cell is the fundamental entity or building
block of a crystal, $F(\mathbf{q})$ is the primary quantity representing the atomic
basis of the crystal structure. For this reason, the structure factor plays a
prominent role in x-ray crystallography.

In the case of a film, the presence of lattice relaxations or distortions in
the film structure often results in the interlayer spacings being dependent on
their vertical positions in the film. For this reason, when deriving a model
to describe the scattered amplitude from a film, the structure factor for the
film is often taken to extend the entire film thickness, with the positions of
the individual atomic layers in the film described by separate parameters
(see Sec. 2.6.3).

2.5.2 Diffraction from a 3D Crystal

The total scattered intensity from a crystal is proportional to the sum of
the amplitudes from all the crystal's unit cells. It is the combined ampli-
tude from the symmetric arrangement of a large number of unit cells in the
crystal that focuses the scattered x-rays into distinct beams, resulting in the
phenomenon that is commonly referred to as diffraction. For simplicity of
discussion, it will be assumed that the crystal consists of a parallelepiped
with N_1, N_2, and N_3 unit cells in the directions of the three crystal axes
$\mathbf{a}_1$, $\mathbf{a}_2$, and $\mathbf{a}_3$, respectively. However, the arguments that follow are equally
valid regardless of the shape of the crystal in question [56]. The scattered

amplitude from all these unit cells is

$$\mathcal{A}_{\text{xtal}} = \mathcal{A}_0 r_0 \frac{1}{R_0} F(\mathbf{q}) S_{N_1}(\mathbf{q} \cdot \mathbf{a}_1) S_{N_2}(\mathbf{q} \cdot \mathbf{a}_2) S_{N_3}(\mathbf{q} \cdot \mathbf{a}_3) \qquad (2.20)$$

where $S_N(x)$ is the geometric sum

$$S_N(x) = \sum_{n=0}^{N-1} e^{ixn} \qquad (2.21)$$

$$= \frac{1 - e^{ixN}}{1 - e^{ix}}. \qquad (2.22)$$

Since the measured intensity will be proportional to the square modulus of the amplitude, the quantity of interest is

$$\left| S_N(x) \right|^2 = \frac{\sin^2\left(\frac{1}{2}Nx\right)}{\sin^2\left(\frac{1}{2}x\right)}, \qquad (2.23)$$

which is called the N-slit interference function. An example of this function is shown in Fig. 2.9 for $N = 10$. As can be seen, it consists of $N - 2$ interference fringes between two large peaks whose heights scale as N^2 and widths scale as $1/N$. In the limit, $N \to \infty$, the N-slit function tends to an array of Dirac delta functions spaced by 2π in x. In the case of a bulk crystal, $N_1, N_2, N_3 \to \infty$ and Eq. (2.20) is zero everywhere except when the Laue conditions, Eqs. 2.7, are satisfied simultaneously. The large peaks in the N-slit interference function of Fig. 2.9 are thus the Bragg peaks described in Sec. 2.3.

Since the intensity is proportional to the square modulus of the scattered amplitude, it can be concluded that the diffraction pattern from a 3D crystal is zero everywhere except at discrete points that lie on a lattice in reciprocal space, where the intensity is

$$I_{HKL} \propto \left| \mathcal{A}_0 r_0 \frac{1}{R_0} F(H\mathbf{b}_1 + K\mathbf{b}_2 + L\mathbf{b}_3) N_1 N_2 N_3 \right|^2. \qquad (2.24)$$

This equation is written as a proportionality relationship since there are a number of experimental corrections that must still be taken into account, which will be detailed in Sec. 2.5.4. However, first a discussion of the differences between the diffraction from a 3D crystal and a 2D film is in order.

N-Slit Interference Function
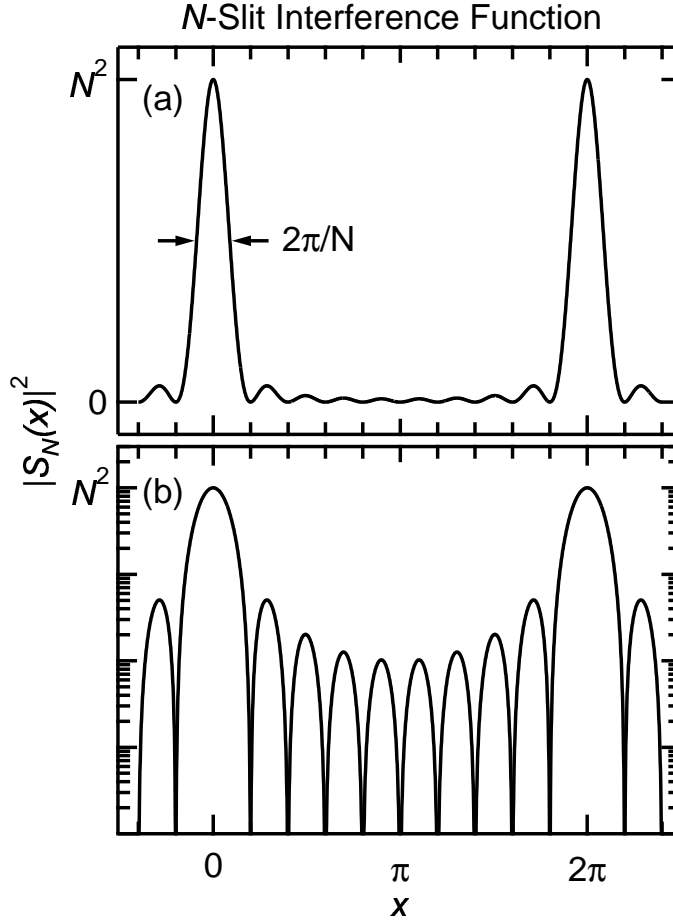
Figure 2.9: The N-slit interference function for $N = 10$ on (a) a linear scale and (b) a log scale. The heights of the main peaks scale as N^2, their widths as $1/N$, and they become Dirac delta functions as $N \to \infty$.

2.5.3 Diffraction from a Film

The conditions for constructive interference (diffraction) from a 3D crystal result in a lattice of Bragg points in reciprocal space defined by the Laue conditions. However, in the case of a film, the crystal is only large in two of the three dimensions. We will operate in the surface coordinate system of the film, as described in Sec. 2.2, where $\mathbf{a}'_3$ is directed along the surface normal (the z direction) and $\mathbf{a}'_1$ and $\mathbf{a}'_2$ both lie in the plane of the film and are thus perpendicular to $\mathbf{a}'_3$. In this case, $N_1, N_2 \to \infty$, and $N_3 = N$ is the number of layers in the film (a film of uniform thickness is assumed for the time being). Then the third Laue condition, Eq. (2.7c), is relaxed and the (former) points in reciprocal space defined by Eqs. (2.7a) and (2.7b) each have a profile like that of Fig. 2.9 extending in the z direction. These

features are called "rods" due to their one-dimensional nature in reciprocal space. In fact, such rod-like features are found around the Bragg points of bulk crystals as well, provided the crystal surface is sharp enough. For this reason, these features are often referred to as crystal truncation rods (CTRs) [65].

Regardless of the in-plane structure of the film and substrate, there is always a CTR for $H = K = 0$; that is, when $\mathbf{q}$ is aligned along the surface normal ($\mathbf{q} \cdot \mathbf{r} = q_z z$). This CTR is the specular rod and it offers a useful probe of the structural features normal to the surface — for example, vertical layer relaxations — without concern for the details of the lateral structure of the film or substrate. Such measurements are valuable when effects due to the lateral structure or in-plane order of the sample are not the primary focus. Although off-specular rods in principle collectively contain more information than the specular rod alone, if the in-plane structure of the film or substrate is not well-ordered, or if it is different for different portions of the film, the intensity along these rods will either be diffuse or divided among different regions of reciprocal space (e.g., different surface domains may have different in-plane orientations). In contrast, the reflectivity rod contains contributions from all the film overlayers regardless of their in-plane structure, and absolute information on vertical layer relaxations and film thicknesses can be obtained. It should be noted that unlike off-specular rods in most cases, the specular rod always contains contributions from both the substrate and the film overlayers. Thus, the scattered amplitudes from both must be added together to calculate the intensity along this rod.

For small momentum transfers ($q \ll 2\pi/a_3'$), the intensity along the specular rod is termed the x-ray reflectivity. It is relatively insensitive to the discrete atomic nature of the film and may include dynamical effects [54,55]. For higher momentum transfers, diffraction effects due to the crystalline structure of the film and substrate are evident. The rod profile in this regime is thus termed the *extended x-ray reflectivity*. To obtain information on the atomic-layer structure of the sample, large momentum transfers must be measured. Thus, for a study of lattice relaxations in film overlayers, or measurement of the distribution of film thicknesses present with atomic-layer resolution, the extended reflectivity is the appropriate portion of the rod to measure.

2.5.4 Geometrical Correction Factors

The measured intensity is proportional to the square modulus of the total scattered amplitude. However, the simplified treatment presented thus far ignores many of the experimental realities of measuring scattered x-ray intensities. The combined effects of these geometry-dependent correction factors will be denoted with the symbol $\mathcal{C}$ and can be broken up into the components [66]

$$\mathcal{C} = P\,\mathcal{C}_L\mathcal{C}_R\mathcal{C}_A \qquad (2.25)$$

where P is the polarization factor, $\mathcal{C}_L$ is the Lorentz factor, $\mathcal{C}_R$ is the rod interception factor, and $\mathcal{C}_A$ is the beam footprint area correction factor, all of which will be discussed below. Since these corrections are all specific to the scattering geometry chosen in the experiment, they in themselves do not contain any information about the structure of the sample. For this reason, and for simplicity of analysis, these geometric corrections were applied to the experimental data before analysis. Thus, most of the x-ray data presented in this work are the experimentally measured intensities divided by $\mathcal{C}$.

The other corrections discussed in this section are those due to temperature effects and those due to surface roughness. As will be seen, these effects have more to do with the details of the physical state and structure of the sample and therefore must in general be taken into account at the level of the structure factor calculation. Furthermore, additional corrections to the raw data may be necessary depending on the type of detector used and the absolute intensity of the scattered x-rays. Such corrections will be separately discussed in Sec. 3.3.2.

Polarization factor

The factor P introduced in Eq. (2.12) results from the different polarizations of the incoming and outgoing x-ray beams. Specifically, $P = |\epsilon_i \cdot \epsilon_f^*|^2$, where ϵ_i and ϵ_f denote the polarization vectors for the incident and scattered waves, respectively. In this work, synchrotron radiation was used exclusively to obtain the x-ray diffraction data. The x rays produced from a synchrotron result either from the emission of radiation as the electrons orbit around the synchrotron ring (bending magnet source) or from the horizontal "wiggling" motion produced as the electrons pass through a series of vertically-oriented permanent magnets placed in the path of the electrons (an insertion device). In any case, the acceleration of the electrons is always in the horizontal plane and hence the emitted x rays will be linearly

polarized in the horizontal plane as well.[§] The polarization factor is thus $P = \cos^2\psi$, where ψ is the angle between $\mathbf{k}_i$ and the projection of $\mathbf{k}_f$ onto the horizontal plane. For the experiments done in this study, the scattering plane (the plane formed by $\mathbf{k}_i$ and $\mathbf{k}_f$) was always horizontal, so in our case $\psi = 2\theta$ and

$$P = \cos^2(2\theta). \tag{2.26}$$

To avoid any confusion, it should be noted that most texts quote the polarization factor as

$$P' = \frac{1 + \cos^2(2\theta)}{2}, \tag{2.27}$$

which is true if the incident x rays are unpolarized. This expression can be easily obtained by noting that if the experiment had been set up such that the scattering plane were vertical, then the polarization factor would have been $P = 1$. Quantum mechanically, unpolarized x-rays are in a superposition of two arbitrary orthogonal polarization states, which can be chosen to be aligned and perpendicular to the scattering plane, respectively. The scattered x-ray intensity is then the average of the scattering from the two different polarization states, which yields Eq. (2.27).

Integrated intensity and the Lorentz factor

One would normally assume that the intensity as calculated in the previous sections would be an observable quantity; however, a number of experimental realities make measurement of such intensities impossible. Sample defects and mosaicity, finite energy resolution of the monochromatic source, and angular dispersion of the incident beam will all result in a finite spreading of the scattered beam. As a result, in practice the intensity of either a 2D or 3D region of reciprocal space is measured. This quantity is called the *integrated intensity* and is usually measured by scanning an angle with the diffractometer while measuring the scattered intensity. Hence, the actual integration is done in angular space, which must be converted to reciprocal space to compare it with theoretical models. This can be done using a standard coordinate transformation for the appropriate diffractometer and geometry [56, 66–68]. In the end, the integrated intensity is found to be related to the peak intensity by a factor called the Lorentz factor, which is equal to the inverse of the Jacobian of the transformation from angular space to reciprocal space. For measurements along the specular rod, the

---

[§]A notable exception to this rule exists in which a specialized undulator can be constructed to produce circularly polarized x-rays. However, such devices are rare and were certainly not used in this study.

Lorentz factor is simply [66, 67]

$$\mathcal{C}_L = \begin{cases} \frac{1}{\sin(2\alpha)} & \text{(rocking curve)} \\ \frac{1}{\sin \alpha} & \text{(ridge scan)} \end{cases} \tag{2.28}$$

where α is the angle the incident x-ray beam makes with the sample surface and the terms "rocking curve" and "ridge scan" refer to two different methods of measuring the specular rod to be discussed in Sec. 3.6.

Rod interception factor

The rod interception factor is related to the manner in which a diffraction rod from a 2D or quasi-2D system is experimentally measured. These techniques are discussed in detail in Sec. 3.6, when the origin of the rod interception factor will be illustrated more clearly. However, a brief discussion of the correction it entails is presented here for the sake of completeness.

The acceptance area of the detector is usually defined using a pair of slits. Such slits are generally perpendicular to each other and to the direction of the x-ray beam being measured. With the rocking curve method of measuring the integrated intensity of the specular rod, these detector slits are scanned across the specular condition to obtain a cross-sectional profile of the rod from which the background and integrated intensities can be determined. The resulting integration volume from such a procedure samples a slice of the specular rod that has a finite thickness in the z direction and that varies depending on the slit settings and angles of incidence and reflection (see Fig. 3.11). Specifically, the thickness of the cross-sectional slice is proportional to $\cos \beta$, where β is the angle the scattered x rays make with the sample surface [see Eq. (3.9)]. Hence, as the intensities at different places along the specular rod are measured (using the same slit settings), the magnitude of the integrated intensity varies as

$$\mathcal{C}_R = \cos \beta. \tag{2.29}$$

This factor is only necessary for data collected using the rocking curve method.

Beam footprint area

The measured intensity from a diffraction feature of a film will be proportional to the illuminated area of the sample. Actually, the area of the

32

sample that will contribute to the signal measured is the intersection of the projected areas of the beam footprint on the sample and the areal acceptance of the detector being used. In addition, angular dispersion of the source x-ray beam and finite angular acceptance of the detector should in principle also be accounted for [66, 67]. However, in practice, the detector slit settings are generally chosen such that the entire illuminated area of the sample is accepted, and with modern beamline optics and proper collimation of the scattered beam, angular dispersion is usually negligible. In particular, for the specular geometry, in which the beam footprint seen from the perspective of the detector is simply the incident beam profile (usually on the order of 0.5 mm × 0.5 mm), acceptance of the fully collimated beam by the detector is generally not a problem and the correction factor can be regarded as equal to the illuminated area of the sample. Assuming that the sample subtends the entire width of the beam, the area of the beam footprint in a specular geometry is proportional to

$$\boxed{\mathcal{C}_A = \frac{1}{\sin \alpha}} \tag{2.30}$$

where α is the angle the incident x rays make with the sample surface.

Debye-Waller factor and TDS

So far, it has been assumed that the atoms occupy fixed positions within the crystal lattice. However, thermal fluctuations in the atomic positions will be present at any finite temperature. Two effects arise from these thermal vibrations. First, a Debye-Waller factor of the form e^{-M} must be included in the structure factor, where $M \equiv \frac{1}{2} \langle \mathbf{q} \cdot \mathbf{u} \rangle^2$ and $\mathbf{u}$ is the displacement vector of the atoms from their equilibrium positions in the crystal due to thermal vibrations [56]. Since atoms of different materials will respond differently to thermal excitations, M will be dependent on both temperature and material. Thus, a unit cell that contains atoms of many different types will need to have the correct Debye-Waller factor applied to each atom in the structure factor. For this reason it is often most appropriate to apply the Debye-Waller factor directly to the atomic scattering factors. Although theoretically-derived values for the Debye-Waller factor are available [69], in the case of a film, where the response of the atoms to thermal excitations is not necessarily the same as their bulk counterparts, it is generally left as a free parameter that is determined from a fit to the experimental data. An example of the effect the Debye-Waller factor has on the atomic scattering

factor of a Si atom can be seen in Fig. 2.8.

Of course, the vibrations of the atoms in a crystal are not isotropic, but are subject to the spectrum of different phonon modes for the material. This fact results in a second temperature-related phenomenon called thermal diffuse scattering (TDS). In terms of effects on the scattered intensity, TDS appears as a series of broad diffuse peaks in reciprocal space emanating in high-symmetry directions from the Bragg points. As such, TDS does not interfere much with the comparatively sharp diffraction features presented in this work and can be considered part of the background that is subtracted from the signal.

Roughness

There are two different mtehods that can be used to account for the roughness of a sample surface. First, a simple model of the statistical properties of the surface roughness can be assumed and the results on the measured intensity profile calculated analytically. This method has been shown to work well for a variety of different surfaces by assuming an exponential distribution of heights on the surface [65]. In this model, layer 0, at the lowest (inner) end of the roughness boundary region, is assumed to be fully occupied, layer 1 right above it has a fraction β of sites occupied (not to be confused with the angle β), layer 2 has fraction β^2, etc. The intensity from such a surface is related to the ideally truncated surface by an additional multiplicative factor

$$I_{\text{rough}} = I_{\text{ideal}} \frac{(1 - \beta)^2}{1 + \beta^2 - 2\beta \cos(\mathbf{q} \cdot \mathbf{a}_3)}. \tag{2.31}$$

Alternately, the distribution of heights present on the surface can be described explicitly, with the relative site occupancy of the different layers in the boundary region included as free parameters to be determined by a fit to the experimental data. Such a method requires a diffraction profile with enough information that the free parameters are sufficiently constrained.

In the case of a supported film, there are two physical regions in which roughness is present. First, the thickness of the film itself (i.e., the number of atomic layers on top of the substrate) will not be perfectly uniform, resulting in a distribution of thicknesses. In our case, it will be found that the lattice structure of the film overlayers is itself thickness-dependent, so the surface morphology must be described explicitly. Since the films studied will have thicknesses less than 20 AL, the intensity along the specular rod will have a rich structure with enough information to determine the film

roughness explicitly, following the second method outlined above. Second, the underlying substrate on which the film is grown is not a perfectly flat surface. Since this roughness is due to statistical variations related to the sample preparation, it can be described using Eq. (2.31). However, clean Si(111) surfaces have been found in previous studies to have very small degrees of roughness [65], which was also found to be the case in this study, where the data analysis was found to be unaffected by inclusion of such a factor.

2.6 Extended Reflectivity of a Pb/Si(111) Film

2.6.1 Overview

In this section, the formulas derived in the previous sections of this chapter are applied to generate explicit equations for the extended reflectivity of a Pb/Si(111) film. These equations will then be used in a least-squares algorithm in Chapters 5 and 6 to fit experimental data. Since we are only concerned with the specularly reflected intensity, the momentum transfer vector is parallel to the surface normal (the z direction). Using the surface coordinate system described in Sec. 2.2.3, $\mathbf{q} \cdot \mathbf{a}_1 = \mathbf{q} \cdot \mathbf{a}_2 = 0$ and the scattering amplitude is dependent only on q_z. Thus, only the positioning and relative occupancy (density) of the atomic planes of the film and substrate in the z direction affect the reflectivity. By convention, the momentum transfer is specified using the reciprocal lattice units of the substrate; hence, in this work, the momentum transfer will be quoted with the index l, the perpendicular momentum transfer in Si(111) reciprocal lattice units (1 r.l.u. = 0.668 Å^{-1}):

$$l = \frac{a_{\mathrm{Si}}\sqrt{3}}{2\pi} q_z.$$

(2.32)

Using this convention, the Si(111) Bragg peak will appear at $l = 3$, whereas since Pb has a lattice constant roughly 10% larger than Si, the Pb(111) Bragg peak will appear at $l \approx 3.3$.

Two distinct surface morphologies were encountered in the experiments. In Chapter 5, films were grown at 110 K in progressive steps, where the thickness of the film was varied by deposition of additional Pb on the sample surface. In these experiments, the film growth was found to follow a layer-by-layer mode in which closed films form with low degrees of roughness. Since the temperature was held constant, the film morphology was effectively frozen in place and can be considered to be more-or-less uniform

over large lateral distances. An intensity calculated assuming only coherent contributions to the intensity is appropriate for such a morphology.

In contrast, Chapter 6 presents experiments where the Pb deposition was only done once per sample. After deposition, the films were annealed to progressively higher temperatures. Eventually, the additional thermal energy is enough that the atoms on the sample surface begin to rearrange themselves into nanostructures that are more stable than the closed films present immediately after deposition. If the distances between such structures is large enough, an incoherent contribution to the measured intensity may be discernible. In this case, the total intensity results from the incoherent addition of the scattered intensities from different regions of the surface. The formula for the reflected intensity differs somewhat for such a sample, with the introduction of a partial coherence factor necessary.

2.6.2 Substrate Amplitude Contribution

Since the reflectivity rod of the film overlayers coincides with that of the substrate, the scattered amplitudes from the two must be added together. All the substrates in this study were pretreated by a method that has been shown to result in a bulk-truncated Si(111) surface (see Sec. 3.5.2). Ignoring for the time being any lattice relaxations near the surface of the Si crystal, the contribution of the substrate to the scattered amplitude is that of a semi-infinite crystal truncated at $z = 0$ and extending in the $-z$ direction

$$\mathcal{A}_{\mathrm{Si}}(q_z) \propto \sigma_{\mathrm{Si}} F_{\mathrm{Si}}(q_z) \sum_{j=0}^{\infty} e^{-iq_z a_{\mathrm{Si}}\sqrt{3}j}, \tag{2.33}$$

where σ_{Si} is the atomic density of a Si(111) plane, $a_{\mathrm{Si}}\sqrt{3}$ is the length of the unit cell in the [111] direction, and $F_{\mathrm{Si}}(q_z)$ is the structure factor of Si as a function of the perpendicular momentum transfer. In the [111] direction, the Si unit cell consists of three equally spaced bilayers, with the interlayer spacing within each bilayer being $\frac{1}{12}$ of the total unit cell length (see Fig. 2.3). For the purpose of calculating the reflectivity, the different in-plane atomic arrangements of the three bilayers in each unit cell are immaterial and the three bilayers can be treated identically. Thus, the reflectivity structure factor for Si is

$$F_{\mathrm{Si}}(q_z) = f_{\mathrm{Si}}(q_z)e^{-M_{\mathrm{Si}}}\left(1 + e^{-iq_z a_{\mathrm{Si}}\sqrt{3}/12}\right)$$
$$\times \left(1 + e^{-iq_z a_{\mathrm{Si}}\sqrt{3}/3} + e^{-iq_z a_{\mathrm{Si}}2\sqrt{3}/3}\right) \tag{2.34}$$

N Layers $N + 1$ Layers
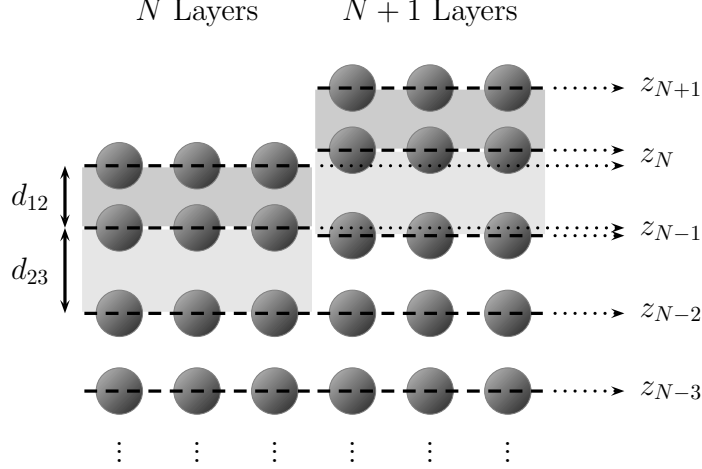
Figure 2.10: Roughness in the film will manifest itself at the atomic scale as a distribution of thicknesses $\{N\}$. Since the relaxation of each atomic layer will depend on its position relative to the film boundary, the positions of the layers from regions of different thicknesses will tend to differ. To account for this effect in the reflectivity, either the exact positions of the layers for each region of thickness need to be known, or an effective distribution in z can be used analogous to a Debye-Waller factor.

where the first term in parentheses is due to the interlayer spacing within each bilayer and the second is the three instances of the bilayer per unit cell. Equation (2.33) then becomes

$$\mathcal{A}_{\mathrm{Si}}(q_z) \propto \sigma_{\mathrm{Si}} f_{\mathrm{Si}}(q_z) e^{-M_{\mathrm{Si}}} \left(1 + e^{-iq_z a_{\mathrm{Si}}\sqrt{3}/12}\right) \sum_{j=0}^{\infty} e^{-iq_z a_{\mathrm{Si}}\sqrt{3}j/3} \qquad (2.35)$$

$$= \sigma_{\mathrm{Si}} f_{\mathrm{Si}}(q_z) e^{-M_{\mathrm{Si}}} \frac{1 + e^{-iq_z a_{\mathrm{Si}}\sqrt{3}/12}}{1 - e^{-iq_z a_{\mathrm{Si}}\sqrt{3}/3}}. \qquad (2.36)$$

The presence of lattice relaxations in the top substrate layers can be taken into account by adding additional Si layers to this amplitude that have adjustable vertical positions. Such an effect was included in analysis of some of the data; however, due to the much greater electron density of the Pb overlayers it was found that effects due to lattice relaxations of the top Si layers were not observable. As such, all of the results presented do not include any parameters describing substrate layer relaxations.

2.6.3 Film Structure Factor

Allowing for possible lattice distortions in the film in the direction of the surface normal, the amplitudes from all the film layers will be included in the structure factor of the film. The scattered amplitude from the film is

then

$$\mathcal{A}_{\text{Pb}} \propto \sigma_{\text{Pb}} F_{\text{Pb}}(q_z) \tag{2.37}$$

where σ_{Pb} is the atomic density of a bulk Pb(111) layer. Note that since Si has a diamond lattice structure and Pb has a *fcc* lattice structure, their (111)-surface atomic densities are related by

$$\frac{\sigma_{\text{Pb}}}{\sigma_{\text{Si}}} = \left(\frac{a_{\text{Si}}}{a_{\text{Pb}}}\right)^2. \tag{2.38}$$

Following prior work in the literature, the structure factor for the film is usually written as [60, 70]

$$F_{\text{Pb}}(q_z) = f_{\text{Pb}}(q_z) \sum_{j=1}^{N_{\text{max}}} \theta_j e^{iq_z z_j} e^{-\frac{1}{2}q_z^2 \zeta_j^2} \tag{2.39}$$

where N_{max} is the number of atomic layers in the thickest portion of the film and θ_j is the fractional occupancy of layer j. The last exponential term is similar to a Debye-Waller factor and accounts for a finite layer distribution in z, where ζ_j is the root-mean-square displacement of the atoms in layer j from their average position, z_j, which is measured relative to the Si surface. This term is particularly important in systems with substantial lattice relaxations since the atomic layers in regions of different thicknesses will in general not line up. This effect is expected to be larger for near surface layers, as illustrated in Fig. 2.10. The ζ_j values for these layers will have a significant component due to the static displacements of the layers in different regions, resulting in a value that depends on j. For films with significant roughness — i.e., with a wide range of thicknesses — the number of independent z_j, θ_j, and ζ_j parameters can become quite large.

Alternatively, in a model that describes the film layer structure more precisely, where the z_j parameters are different for each thickness N, the ζ_j parameters will be approximately independent of j and can be taken outside the sum as a standard Debye-Waller factor $e^{-M_{\text{Pb}}}$. In such a model, the film contribution to the structure factor is written as

$$F_{\text{Pb}}(q_z) = f_{\text{Pb}}(q_z) e^{-M_{\text{Pb}}} \sum_N p_N \sum_{j=1}^N e^{iq_z z_{j,N}} \tag{2.40}$$

where p_N is the fractional surface area covered by N Pb layers and the first

sum is over all thicknesses present in the film. That is,

$$\theta_j = \sum_{N \geq j} p_N, \qquad (2.41)$$

and

$$\sum_N p_N = 1. \qquad (2.42)$$

In this scheme, the coverage of the film, which is proportional to the total number of Pb atoms in the film and is measured in AL of Pb,[*] is

$$\Theta = \sum_N N p_N. \qquad (2.43)$$

Generalizing the z_j values to be N-dependent will add numerous additional parameters if they are taken as independent degrees of freedom, which can substantially complicate the data analysis. To avoid this difficulty, a physical model is derived in Sec. 4.4 that describes the lattice distortions. From this model, the $z_{j,N}$ are calculated using only a small number of adjustable parameters, eliminating most of the independent variables. This model for the x-ray reflectivity has far fewer degrees of freedom than the model using Eq. (2.39), yet was found to reproduce the results with a similar degree of precision, indicating that the $z_{j,N}$ values calculated with the lattice distortion model accurately reflect the actual film morphology.

2.6.4 Calculation of the Measured Intensity

As discussed in Sec. 2.6.1, any sample will have regions of different thicknesses. If the lateral distances between these regions is much smaller than the coherence length of the scattered x rays, the integrated intensity is proportional to the coherent sum of the contributions from the substrate and the Pb overlayers

$$I_{\mathrm{coh}}(q_z) \propto \mathcal{C} \left| \mathcal{A}_{\mathrm{Si}}(q_z) + \mathcal{A}_{\mathrm{Pb}}(q_z) \right|^2, \qquad (2.44)$$

where $\mathcal{C}$ is given by Eq. (2.25). Equation (2.44) is written as a proportionality relationship since in practice only the relative intensity is measured; thus, an arbitrary scale factor must be included when comparing theoretical calculations with empirical measurements.

---

[*]In other texts, coverages are often quoted in "monolayers", which may be relative to the atomic surface density of either the film or substrate. Here the unit of "atomic layer" is used, which is less ambiguous. In terms of coverage, 1 AL is equal to a monolayer in Pb units.
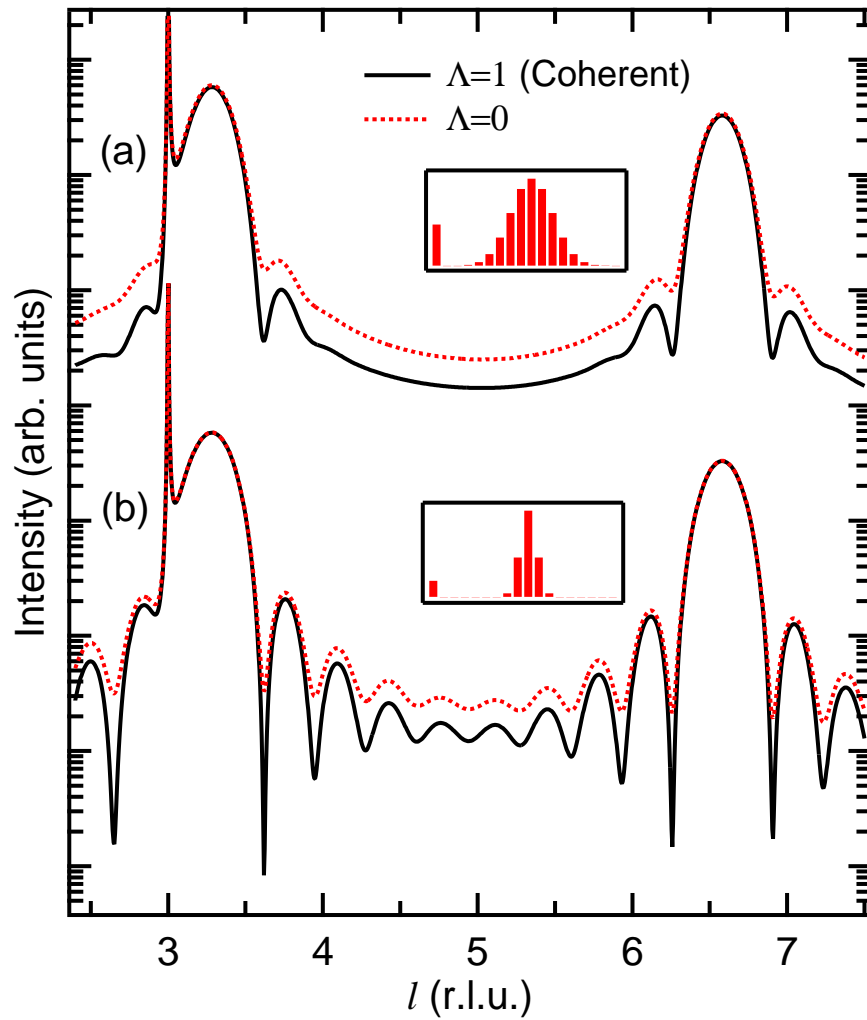
Figure 2.11: Examples of the extended reflectivity for two different Pb films on Si(111) substrates. The intensities using both the coherent and incoherent calculations are shown. (a) A film with a significant degree of roughness (5.7 Å rms). Few interference fringes are present between the Pb Bragg peaks at $l \approx 3.3$ and 6.6. (b) A film with a low degree of roughness (2.3 Å rms). More interference fringes are evident, with the profile very similar to the ideal N-slit interference function shown in Fig. 2.9(b). Taking into account the incoherent addition of regions of different thicknesses tends to raise the relative intensity of the profile between the Bragg peaks and diminish the interference fringes. In both cases, the distribution of thicknesses used to calculate the profiles, which include a wetting layer, is shown in the insets.

2. SURFACE X-RAY DIFFRACTION

If regions of different thicknesses are separated by significant lateral distances, the reflected intensity will have a component due to incoherent scattering from these different regions. In the extreme case, where all the thickness regions add up incoherently, the total intensity is the weighted sum of the intensities from each separate region, which consists of a single height island surrounded by a wetting layer. Since the wetting layer fills in the space between the different thickness regions, it will contribute coherently in each case. The structure factor for a region with islands that are N layers thick surrounded by the wetting layer is thus

$$F_{\mathrm{Pb}}^N(q_z) = f_{\mathrm{Pb}}(q_z)e^{-M_{\mathrm{Pb}}} \left[p_1 e^{iq_z z_1} + (1-p_1)\sum_{j=1}^{N} e^{iq_z z_{j,N}} \right] \qquad (2.45)$$

and the total scattered intensity is the incoherent sum of the intensities from each individual thickness region is

$$I_{\mathrm{incoh}}(q_z) \propto \mathcal{C} \sum_{N>1} \frac{p_N}{1-p_1} \left| \mathcal{A}_{\mathrm{Si}}(q_z) + \sigma_{\mathrm{Pb}} F_{\mathrm{Pb}}^N(q_z) \right|^2. \qquad (2.46)$$

Note that in the ideal case where the surface consists of islands of only one thickness separated by regions covered only by the wetting layer, Eq. (2.45) reduces to Eq. (2.40) and Eq. (2.46) reduces to Eq. (2.44); i.e., the incoherent and coherent intensities are equivalent, as one would expect.

In actuality, the reflected intensity is likely some combination of coherent and incoherent scattering from regions of different thicknesses, in which case the measured reflected intensity is

$$I(q_z) = \Lambda I_{\mathrm{coh}}(q_z) + (1-\Lambda) I_{\mathrm{incoh}}(q_z) \qquad (2.47)$$

where Λ is a partial coherence factor ($0 \leq \Lambda \leq 1$), which is treated as a fitting parameter in the analysis. The calculated extended x-ray reflectivity for two different Pb films is shown in Fig. 2.11 to illustrate the effects of roughness and the coherence factor on the rod profile. In this graph, the reflectivity is plotted as a function of l, as defined in Eq. (2.32). Figure 2.11(a) shows the reflectivity profile for a rough film (5.7 Å rms), with the p_N distribution shown in the inset. Both the coherent (solid curve) and incoherent (dotted curve) intensities are shown. The main features in both cases are the Si(111) Bragg peak at $l = 3$ and the Pb(111) and (222) Bragg peaks at $l \approx 3.3$ and 6.6, respectively. In between the Pb Bragg peaks are relatively few fringes due to the significant film roughness. In contrast, the calcula-

tion for a smooth film (2.3 Å rms), shown in Fig. 2.11(b), exhibits more pronounced interference fringes very similar to the N-slit function profile in Fig. 2.9(b). From this figure two primary effects due to the coherence factor are apparent. First, the ratio between the intensities at the in-phase (Bragg peaks) and out-of-phase conditions (midway between the Bragg peaks) for Pb is different, with the incoherent profile being on average more intense than the coherent profile. Second, the interference fringes are more pronounced in the coherent calculations than the incoherent ones.

3 Experimental Methods

3.1 Introduction

This chapter provides an overview of the methods and equipment that were used in the experimental portion of this work. Since all of the experiments involved the preparation of the samples in an ultrahigh vacuum (UHV) environment, a brief introduction to this technology as well as a general description of the vacuum setup used will be given. However, since a complete understanding of vacuum technology and UHV hardware is not necessary to understand the results presented here, the focus will be primarily on the equipment and procedures used specifically in the experiments described in this work. The interested reader is directed to other sources [71–73] for a more comprehensive discussion of UHV technology and its applications.

Next, various different methods and instruments used to detect x rays are described. Although there exists a wide range of sophisticated detectors to choose from [74–76], the discussion in this chapter will focus on those that were used in this study, which were all single-channel photon counters (point detectors).

Since x rays interact weakly with matter, the use of a high-brilliance synchrotron source is all but necessary to do high-resolution atomic-scale studies. All of the experimental data in this work were collected using monochromatic x rays from an undulator source at a third-generation synchrotron storage ring. This facility and the experimental equipment used there are described along with a brief overview of how the x-ray beam is generated and produced.

Then the methods used to prepare the samples and to grow the metal films are discussed. In particular, it was found that a pretreatment of the semiconductor substrates greatly improved the quality of the metal films. The resultant films after deposition have near-atomic uniformity in thickness that enables monolayer-resolved studies to be done. Such a pretreatment also results in a bulklike truncation of the Si substrate which simplifies the analysis and provides a sharp buried interface that enhances the quantum confinement effects that will be studied.

Finally, two different techniques for measuring the x-ray reflectivity rod are presented. The rocking curve method provides highly accurate data over the widest range of momentum transfer and is traditionally the one most widely used for high-resolution CTR measurements; however, it requires a great deal of time to acquire a single set of data. Due to the time constraints on experiments at a synchrotron facility, such a time-consuming method makes a study difficult when the measurements need to be repeated frequently for the same physical sample. The ridge scan method of collecting the extended x-ray reflectivity solves this problem by collecting the entire reflectivity rod in just 1–3 scans, which greatly reduces the amount of time needed to acquire a single set of data. Both methods have certain limitations and advantages over the other that will be discussed in detail. For the range of momentum transfer studied in this work the two methods were found to yield equivalent data.

3.2   Ultrahigh Vacuum

3.2.1   Characteristics

For a study of the atomic-scale properties of surfaces, precise control of the preparation and cleanliness of the sample surface is essential. Since a surface by definition is exposed to the ambient environment, it is always subject to contamination. In the case of a reactive surface, residual gas atoms may chemically bond with exposed atoms at the surface to form molecular compounds of the material that are not desired (an oxide layer, for instance). However, even an inert sample will have condensed layers of gas atoms or molecules adsorb onto it. Herein lies the utility of a vacuum chamber. By removing the bulk of the ambient gas in a controlled environment, a sample surface can be kept clean for an extended period of time during which it can be manipulated in a controllable and repeatable manner to study the physical processes at work. Depending on the application to be performed on the surface, different pressure ranges are needed. The highest degree of vacuum (i.e., with the lowest ambient pressure) is termed *ultrahigh vacuum* and it requires special procedures and equipment to produce and maintain. The different classes of vacuum and their pressure ranges are shown in Table 3.1.

Although the *Système International* unit of pressure is the Pascal (N/m^2, abbreviated as Pa), traditionally in high-vacuum science the unit of torr (mm Hg) is used, named after Evangelista Torricelli (1609–1647), the inventor of the mercury barometer and a contemporary of Galileo. Another unit

Name	Pressure Range (torr)	Monolayer Formation Time (s)	Mean Free Path (m)
Low (Rough)	$760 - 10^{-3}$	$10^{-9} - 10^{-4}$	$10^{-6} - 10^{-2}$
High	$10^{-3} - 10^{-8}$	$10^{-4} - 10$	$10^{-2} - 10^{4}$
Ultrahigh	$10^{-8} - 10^{-9}$ $10^{-9} - 10^{-10}$ $< 10^{-10}$	$10 - 500$ $500 - 10^{4}$ $> 10^{4}$	$10^{4} - 10^{5}$ $10^{5} - 10^{6}$ $> 10^{6}$

Table 3.1: Various pressure ranges and some of the typical characteristics of the vacuum environment in those ranges. All values should be taken as approximate orders of magnitude for a typical vacuum system.

that is commonly used is the millibar (mbar). The conversion amongst these units is 0.75 torr = 1 mbar = 100 Pa. One atmosphere (atm) of pressure is equal to 760 torr = 1013 mbar = 10^5 Pa.

A rough indication of the length of time a sensitive sample surface can be kept clean in a vacuum environment is the time it takes for a single layer of molecules to form on the surface assuming a unity probability for sticking. This quantity can be estimated by calculating the arrival rate of atoms on the surface given the molecular density of the ambient gas [71] and is called the *monolayer formation time*. The monolayer formation time for different pressure ranges is shown in Table 3.1, where it can be seen that in order to keep a sample surface in good condition for more than a few minutes, pressures on the order of 10^{-10} torr must be achieved, which is well into the UHV regime.

In addition to being able to keep a sample surface clean, a vacuum environment also enables the use of a variety of techniques essential for surface science due to the increased mean free paths. When the mean free path of particles in a system is greater than the system size, the gas molecules are said to be in the *molecular flow* regime. In this regime, the behavior of particles in the gas phase is no longer dominated by interparticle collisions, as with a gas at atmospheric pressure. This regime is in contrast with the viscous flow regime, in which a gas behaves like a fluid, with pressure differentials and possibly turbulence governing the diffusion properties of the molecules. Operating in the molecular flow regime is required for techniques that rely on focused particle beams, such as electron diffraction, ion sputtering, molecular beam epitaxy, electron microscopy, etc.

3.2.2   Vacuum Pumps

In order to achieve and maintain UHV pressures, specialized pumps must be used both to initially evacuate the chamber and then to balance the gas load that is constantly being produced by outgassing from exposed surfaces and diffusion into the chamber. In all cases, any one pump is only appropriate for a certain range of pressures; hence, a series of different pumps must be used in sequence to attain very low pressures.

Roughing pump

A "roughing" pump is so named because it is meant to bring or maintain a system at rough vacuum pressures. These pumps perform the bulk of the volume gas removal of the vacuum chamber during the initial stages of evacuation. They rely on pumping mechanisms that are appropriate for gases in the viscous flow regime. Specifically, they all generally consist of a chamber that changes its configuration in such a way that it sucks gas in one end and spits it out the other. They accomplish this by compressing the gas coming in an inlet and physically transporting it to an exhaust port. This process relies on the fluidic properties of the gas. Many ingenious designs have been developed to do this sort of pumping, which are discussed elsewhere in exhaustive detail [72, 73]. The base pressure achievable with a roughing pump is usually on the order of 10^{-3} torr. Since roughing pumps are generally sealed with oil, which is a highly undesirable substance to get in an UHV chamber (see Sec. 3.2.3), these pumps are never connected directly to the chamber but are rather used to "back" the outlet of another pump, usually a turbomolecular pump, as a final stage in a chain of pumping stations. In the experimental setup used for this research, either a rotary vane pump or a scroll pump was used as a roughing pump.

Turbomolecular pump

The turbomolecular (or "turbo") pump is often the workhorse for systems that only require high vacuum conditions and is the pump of choice to initially evacuate an UHV chamber to these pressures. It consists of a series of turbines that spin at high speeds (10 000–100 000 rpm) to impart momentum to ambient gas molecules preferentially in a certain direction (namely, toward the pump's outlet). A turbo pump has high pumping speeds, low ultimate pressures, and operates cleanly (little backstreaming of oils into the chamber) and reliably. Typically, a turbo pump can maintain pressures on the order of 1×10^{-7} torr or below. The blades of the turbines in a

46

turbo pump impart their momentum to the gas molecules most efficiently in the molecular flow regime. Therefore, they are not suitable for exhausting directly to atmospheric pressure and must be backed by a roughing pump of some sort, as described above. In the case of an UHV system, turbo pumps are generally used to get the pressure of the vacuum chamber low enough that an ion pump can be used, at which time the chamber is sealed off from the surrounding atmosphere and the turbo pump disconnected.

Titanium sublimation pump

The titanium sublimation pump (TSP) reduces the pressure inside a vacuum chamber not by moving gas molecules from the interior to the exterior of the physical system, as is done by the pumps described thus far, but rather it traps them by chemically bonding gas molecules into solid compounds in a process called *gettering*. The pump itself simply consists of a filament of titanium that is heated up using a high alternating current (∼50 amperes) that sublimates a fresh layer of titanium on the surrounding walls. The chemically reactive titanium traps (getters) the residual gases in the chamber by forming solid compounds (e.g., titanium oxide), thereby removing them from the vacuum. Eventually, the titanium film becomes saturated and a new film of the metal must be sublimated. Hence, the TSP is generally only used at very low pressures. The use of titanium as a gettering agent results from its relatively low cost, low sublimation temperature, and its chemical reactivity with a wide range of different gases. However, due to the chemical nature of the pumping mechanism, the TSP does not pump inert gases such as helium or argon.

Sputter-ion pump

A sputter-ion pump, often referred to simply as an "ion pump," is the most important pump in most UHV systems. Its general principle of operation is to ionize any gas molecules that happen to wander into the body of the pump and then accelerate those ions through a high-voltage electric field and bury them into the pump surfaces. The ions are produced through collisions with high energy electrons that are discharged from the cathode. The probability of producing a collision between these electrons and the gas molecules in the vacuum is increased by confining the electrons to spiral paths with magnetic fields produced by strong permanent magnets on the outside of the pump. Some of the cathodes in the pump are made of titanium or tantalum, which are sputtered by the high-energy gas ions impinging on

them, depositing fresh layers on the surrounding surfaces. These surfaces pump additional gas molecules by gettering, similar to a TSP. In addition, the sputtered material can further bury molecules that are already embedded near the anode. The ion pump is generally the pump of choice for the standard UHV system, for it is clean (no oils), is dependable (no moving parts), has a long service life (easily several decades if treated properly), and has a very low ultimate pressure ($\sim 10^{-11}$ torr). The ion pump will also pump all kinds of gas molecules, including inert gases such as argon. As the pressure in the chamber decreases, the ionization current decreases proportionately, which can be used to measure the pressure inside the chamber. However, usually an ionization gauge (Bayard-Alpert) is used instead, which measures an ionization current much in the same manner as an ion pump but is optimized for measuring pressures instead of pumping gases.

3.2.3 Achieving UHV

Getting a chamber down to UHV pressures is not just a matter of using the right pumps. Care must be taken to ensure that the inside surfaces of the pumping chamber and all materials inside are extremely clean and free of grease or oils. Indeed, any material that has a high vapor pressure is unsuitable for use inside an UHV chamber. In addition, since part of the process of getting to UHV pressures involves heating up the chamber and all its inner components to 100–200°C (see "Baking out" below), all the materials used in the construction of the chamber and its constituent parts (including samples and instruments) must be able to withstand heating to this temperature range for 12–24 hours. Generally, the chamber and as many of its parts as possible are made from vacuum-fired 300-series stainless steel. Other common materials used are aluminum, copper (oxygen free high-conductivity, preferably), tungsten (for filaments), glass, quartz, and ceramics. Electrical insulation is accomplished with glass beads, pieces of alumina, or sometimes sheets of mica. All removable parts of the chamber (port holes, instrument connections, windows, etc.) are connected to the chamber via flanges with copper gaskets sandwiched between opposing knife edges. To ensure that all materials that go into the UHV chamber are absolutely clean, new equipment that will be in the vacuum is either electropolished, acid etched, or at least scrubbed clean and degreased with organic solvents in an ultrasound bath. All components must be handled with surgical gloves and similarly degreased tools.

Procedure	Pump(s) Used	Pressure Range (torr)	Time (hours)
Volume gas removal	Roughing	$760 - 10^{-3}$	$0.1 - 0.2$
Pumping down to high vacuum	Turbo + Rough	$10^{-1} - 10^{-7}$	$1 - 5$
Seal off chamber, pump to unbaked base pressure	Ion	$10^{-6} - 10^{-9}$	$2 - 8$
Bakeout	Ion	$10^{-6} - 10^{-8}$	$12 - 24$
UHV experiments	Ion, TSP	$10^{-10} - 10^{-11}$	—

Table 3.2: A typical procedure for pumping down a vacuum chamber to UHV pressures, the pumps used in each step, and the typical time taken.

Pumping down

The actual pump down of the UHV chamber follows a logical progression of steps to incrementally get from atmospheric pressure down to UHV. These steps are outlined in Table 3.2. First, the bulk volume of the gas in the chamber is removed with a roughing pump through a turbo pump. In practice, the turbo pump is generally started at the same time as the roughing pump since it takes it awhile to accelerate the turbines to effective pumping velocities. By the time the turbo is up to speed, the chamber is usually roughed out and the turbo automatically takes over as the primary pumping mechanism, backed by the roughing pump. The chamber is evacuated to high vacuum using the turbo pump, which may take 1–5 hours, depending on the size of the chamber and other factors. Once the chamber pressure is in the vicinity of 10^{-5}–10^{-6} torr, the ion pump is turned on and a valve between the chamber and the turbo pump closed. At this point, the chamber is sealed from the exterior atmosphere. The ion pump is then run for a few hours to get the chamber to a modest pressure before the bakeout is started.

Baking out

The bakeout is a critical process for achieving low UHV pressures. The rate-limiting process that prevents an unbaked system from getting below around 10^{-9} torr is desorption of gases from the interior surfaces of the chamber and its components. A system that was at atmospheric pressure will have multiple layers of material (mostly water vapor) adsorbed to its internal surfaces. When the system is evacuated to low pressures, these

adsorbed layers will slowly outgas into the chamber. Left alone, these adsorbed layers can continue to outgas for years, preventing the pressure from getting below ~10^{-9} torr. Luckily, this process can be accelerated by orders of magnitude by "baking" the system at high temperatures ($> 100°$C) for an extended period of time (12–24 hours).* Following this bakeout, any samples or equipment in the chamber that may be subsequently heated up during operation (e.g., filaments, evaporation crucibles) are outgassed near their operating temperatures to minimize any contamination of the vacuum environment during the experiment. The need for baking can be partly lessened by carefully venting the system with dry nitrogen gas when bringing it back up to atmospheric pressure and keeping the chamber closed off from the ambient environment; however, in general, baking out the chamber is a requirement for reaching low UHV pressures.

After a thorough bakeout, the gas load due to desorption from the internal surfaces of the system is usually replaced by other factors that limit the ultimate base pressure of the UHV chamber. Namely, the outdiffusion of gases from the solid materials inside the system and permeation of gases through the chamber walls and seals. In particular, the stainless steel that is used to build the vacuum chamber generally contains a significant amount of hydrogen that diffuses into it during the high-temperature fabrication process. This hydrogen will slowly diffuse to the surface of the walls of the chamber and outgas into the interior. To complicate matters further, due to its low atomic weight, hydrogen is usually one of the gases pumped less efficiently by ion pumps. Hence, in a clean, well-baked UHV chamber, the dominant residual gas at base pressure is usually hydrogen.

3.3   X-Ray Detectors

3.3.1   Point Detectors

The simplest form of x-ray detector is one which simply counts photons. This type of detector is also called a point detector since it does not distinguish between photons measured at different areas of its active surface. All of these detectors rely on an ionization process of some kind, either in a gas or in a solid. In any case, the number of ionization events, which is (ideally) proportional to the intensity of the incident x rays, is quantified in the form of pulses, which are then counted by accompanying electronics. If

---

*Hence the ever-present tin foil that covers most UHV chambers, which is wrapped around the system to create an oven effect, evening out and increasing the temperature of the bakeout.

used to measure the intensity of diffracted beams from the sample, the active area of the detector is usually defined by a pair of slits that can be adjusted to change the angular resolution of the measurements. Point detectors have the advantage that their angular and directional acceptance can be easily specified, while blocking out unwanted background sources of radiation such as upstream[†] air scattering. Hence, these detectors effectively measure a "point" in reciprocal space, providing high-resolution data with a good signal-to-background ratio.

Ion chamber

The ion chamber detector is essentially a parallel plate capacitor that is held at a high voltage (a few hundred volts, usually) and with a distance between the plates large enough to allow an x-ray beam to pass through. The x rays will ionize a portion of the gas molecules between the two plates. The electron-ion pairs are separated by the electric field produced by the voltage differential and collected at the two plates. This process produces a small ionization current that is proportional to the number of ions produced. This current is then amplified and converted to a frequency that is subsequently counted by the counting electronics. The ion chamber can be simply open to the ambient environment or it can be sealed and filled with other gases, depending on the application. The linearity of the detector's response to an incident energy is dependent on the type of gas in the ion chamber as well as the wavelength of the x rays being measured. The ion chamber has the advantage that it can be easily configured as a pass-through detector where only a small portion of the x-ray beam is absorbed by the gas in the chamber and the rest is left unmolested to be used downstream. Such a detector is useful as a monitor of the intensity of the x-ray source, which will vary slightly over the duration of the experiment. In the present work, ion chambers were used in such a capacity to normalize the experimental data as described in Sec. 3.3.2.

Scintillation detector

A scintillation detector has two separate components. The initial component is composed of a (solid) material that easily fluoresces (scintillates) when exposed to x rays. The visible light photons then hit the photocathode of a photomultiplier tube, which produces an electrical pulse whose height

---

[†]The terms "upstream" and "downstream" are often used to refer to relative positions along the beamline. "Upstream" refers to the direction towards the x-ray source.

is roughly proportional to the energy of the incident x ray. Hence, a scintillation detector has a modest degree of energy resolution that can be used to filter out higher energy x rays from higher harmonics or lower energy x rays from sample fluorescence. Such filtering can be done with a discriminator, the windows of which can be set by monitoring the pulses from the detector with an oscilloscope. The accepted pules are then shaped and counted by the appropriate electronics. A scintillation detector is quick, efficient and very sensitive. In fact, one must be careful not to expose the scintillation material to the direct x-ray beam (or any other very intense beam, such as that from a Bragg peak) without reducing the intensity of the x rays, otherwise the scintillation material can be damaged. A scintillation detector was the primary detector used to collect the diffracted intensities in the experiments.

PIN diode

The final detector that will be discussed is the PIN diode. This device is a solid-state detector comprised of three adjoining pieces of silicon: a p-type portion, an intrinsic portion, and a n-type portion. This configuration is responsible for the acronym in the moniker of the detector. When the intrinsic silicon portion is exposed to x rays, electrons are excited from the valence band into the conduction band, creating an electron-hole pair. A high bias voltage across the diode separates the electron from the hole much as the high voltage in the ion chamber separates the electron-ion pairs. The PIN diode is thus a solid-state version of the gas-filled ion chamber, with the difference that it takes ∼30 eV to create a electron-ion pair in the ion chamber whereas for the intrinsic silicon it is closer to 3 eV. A PIN diode is thus much more sensitive. A PIN diode detector is very linear with a wide dynamic range (10–10^6 c/s) over a broad range of energies (5–25 keV). Like the ion chamber, though, it provides no energy resolution. In this research, a PIN diode was often used during orientation of the sample, since it is not prone to damage due to intense beams from bulk Bragg peaks.

3.3.2 Measurement Corrections

In addition to the correction factors discussed in Sec. 2.5.4, there may be additional corrections that need to be be made depending on the type of detector used and its accompanying electronics. Since these factors are specific to the equipment used in each individual experiment, all of the data presented in this work has been adjusted for the effects described in this

section.

Signal Normalization

The intensity of the x-ray source always fluctuates slightly over long time scales (minutes to hours). If nothing else, the current in the storage ring of the synchrotron will change slightly over time. More significantly though, the beamline itself is tuned to produce a highly focused beam of x rays up to 70 m from the source. Even very minute changes in the alignment of the beamline optics, such as the thermal expansion or contraction of a crystal in the monochromator, or even the passage of some heavy machinery through the experiment hall, may result in small fluctuations in the intensity of the beam. In any case, to accurately compare data collected at different times during the experiment, the relative intensity of the incident x-ray beam must be known. This can be done with a *monitor* detector, which is usually an ion chamber placed after the slits defining the incoming x-ray beam. The measured intensities are normalized to the monitor, and hence the incident beam intensity, by dividing the scattered intensity by the monitor value.

Use of Filters

Any detector used will have a limited dynamic range in which its response is linear or quasi-linear. Indeed, in some cases, prolonged exposure of a detector to an overly intense x-ray beam can cause damage to it. Since the scattered intensities from 2D diffraction features may vary by multiple orders of magnitude (for example, see Fig. 2.11), it is often necessary to adjust the incident x-ray intensity by a known factor. This can be accomplished by the insertion of one or more thin foils (filters) into the path of the incoming x-ray beam. If the intensity along a diffraction rod is collected in a single scan (see Sec. 3.6.2), different filters may be needed for different portions of the scan to keep the signal strength in the optimal range. In such cases, special homegrown scanning scripts were used in this research that monitored the intensity of the scattered x-ray beam and adjusted the number and type of filters used to keep the measured signal within the optimal dynamic range of the detector. Note that as long as the monitor detector described above is downstream of the filters in the incident beam, the normalization of the signal to the monitor value should automatically account for the relative changes in the incident intensity, provided that any nonlinearities in the response of the monitor and detector are corrected for as described below.
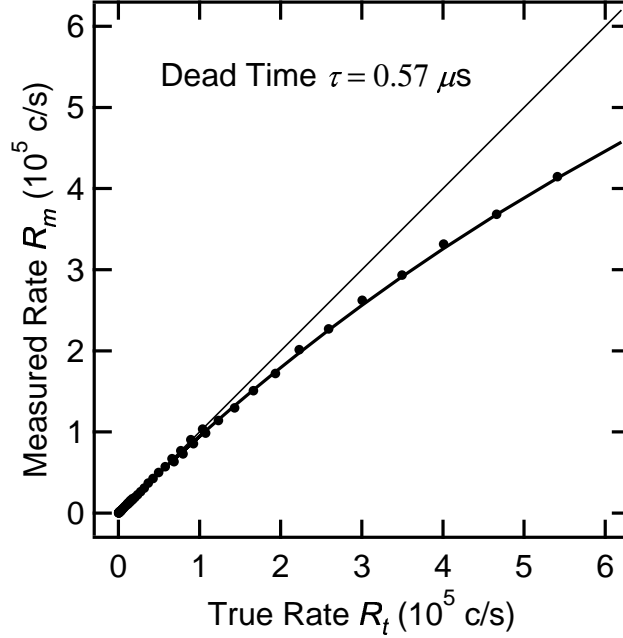
Figure 3.1: Example of the dead time effect for a scintillation detector as measured at Sector 33ID-E. At higher count rates, the detector begins to miss counts as it approaches saturation. This effect can be partially corrected for analytically if the time constant of the detector and counting electronics is measured. The solid curve is a fit using Eq. (3.1).

Dead Time

Any detector which produces pulses which are directly counted, such as the scintillation detector of Sec. 3.3.1 (but not the ion chamber or PIN diode, see below) will have a characteristic response time. If two events are registered by the detector within this time period, they will not be resolved as distinct pulses. For this reason, this response time is referred to at the *dead time* of the detector. Actually, the dead time constant is determined by the combined system of the detector and its accompanying counting electronics. For slower count rates, the detection events will be amply spaced apart from each other and the dead time will have little effect on the measured intensity; however, as the count rate increases, more and more pulses will be missed due to the detector's dead time until eventually the detector reaches its saturation point. In any case, the dead time effect is responsible for a certain degree of nonlinearity in the response of a pulse generating detector such as a scintillation detector.

It can be shown that for small deviations from linearity, the count rate

3. EXPERIMENTAL METHODS

measured by a pulse-based detector is [77]

$$R_m = \frac{R_t}{1 + R_t \tau} \tag{3.1}$$

where R_t is the true count rate and τ is the dead time constant for the system. Inverting this equation yields

$$R_t = \frac{R_m}{1 - R_m \tau} \tag{3.2}$$

for the true count rate in terms of the measured count rate. The dead time constant of the system can be determined empirically by measuring a reference intensity over a wide dynamic range for the detector. This can be done in practice by using a set of filters with known transmission rates. Multiple data points in the dynamic range of the detector can then be obtained by simply going through the series of filters and measuring how the count rate changes, as demonstrated in Fig. 3.1. The reference count rate can be found from the linearity of the lower end of the range and the dead time constant can be found by a one-parameter fit using Eq. (3.1). In this case (for a scintillation detector at Sector 33ID-E), the dead time constant was found to be 0.57 μs. In principle, if any component of the system is changed — the detector, the counting electronics, the amplifier, etc. — then the time constant of the system will change. In this research, the dead time constant was consistently found to be between 0.5–1.0 μs.

To minimize the effect of the dead time correction, count rates were generally kept below 150 000 c/s so that the detector response was as linear as possible. Nonetheless, this effect was corrected for using Eq. (3.2) in all the experimental data collected with a scintillation detector.

Dark Count

In the cases of the ion chamber and PIN diode, pulses directly from the detector are not registered by the counting electronics. Rather, the detectors themselves produce a current that is amplified and converted to a voltage. The voltage level is run through a voltage-to-frequency converter which is then fed to the counting electronics. Thus, as long as the current produced by the detector is proportional to the incident intensity, the response will be linear and no dead time correction is necessary. That being said, since the ionization currents produced are generally quite small, the initial current amplifier usually must have a high gain ($\sim 10^6$ V/A). As a result, small amounts of electrical noise and leakage current can result in a finite count

Figure 3.2: An aerial view of the APS showing the approximate location of the UNICAT beamlines.

rate being registered even when the ionization current itself is zero. This count rate is referred to as the *dark count* since it is present even when the x-ray source is turned off. The dark count can be minimized by adjusting the offset level of the current amplifier. However, depending on the dynamic range of the detector that is used (which may be quite large if the detector is a monitor that sits after a set of filters, see Page 53), the dark count may still need to be subtracted from the signal. In general, the dark count rate drifts slowly over long time periods (hours to days), and as such should be measured on a regular basis.

3.4 Experimental Setup

3.4.1 The UNICAT Beamline Sector 33ID at the APS

All of the experimental data was collected at the Advanced Photon Source (APS), Argonne National Laboratory, outside of Chicago, IL. The APS is a 7 GeV electron storage ring specifically designed for the production of synchrotron radiation. X rays are produced either using the bending magnets that keep the electrons moving in a circular orbit, or by insertion devices such as an undulator, which are tailored for the production of highly focused intense x-ray beams. The experimental data presented in this work
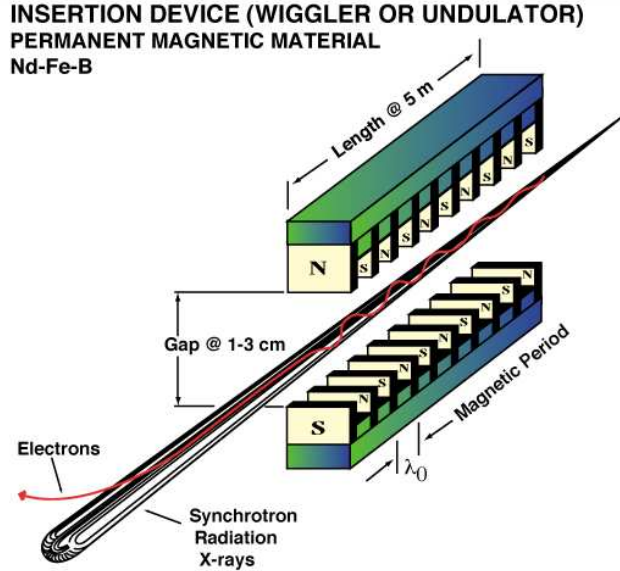
Figure 3.3: Diagram of an insertion device (wiggler or undulator). Magnetic fields of alternating polarities are placed together in a regular fashion, causing the electrons to weave back and forth through the device. In this manner the radiation from each oscillation in the path of the electrons adds up (incoherently in the case of a wiggler and coherently in the case of an undulator) to produce a more intense x-ray beam.

was obtained at Sector 33ID, operated by the UNICAT (University, National Laboratory, Industry Collaborative Access Team) collaboration. Below is a brief overview of this beamline and its respective components.

Undulator

The basic source of synchrotron radiation is the centripetal acceleration of x rays in a curved path [78]. Hence, synchrotron radiation can be easily produced simply by shooting an electron through a magnetic field. Indeed, this is the basis for bending magnet sources. However, a much more intense source of x rays can be constructed by putting a series of magnetic fields oriented in opposite directions together, as illustrated in Fig. 3.3. Such a device is commonly referred to as a wiggler. The intensity of a wiggler source is equal to $2N$ times the intensity of a single bending magnet, where N is the number of periods in the wiggler. An undulator is very similar to a wiggler except that the spacing between the magnets and their field strength (varied by adjusting the separation between the magnets) are tuned such that the radiation emitted from the electrons in one oscillation of its path is in phase with the radiation emitted from the other oscillations. The coherent sum of the amplitudes of the radiated waves from each oscillation is only valid for

Figure 3.4: A picture of an undulator while being serviced at the APS.

a very narrow band of energies (and their harmonics). Thus, the undulator effectively compresses the energy spectrum of the emitted radiation so that it is concentrated at certain energies. A picture of an actual undulator at the APS is shown in Fig. 3.4. Sector 33ID uses APS Undulator A as its insertion device, which provides high brilliance x-rays over the energy range 4–40 keV.

Monochromator

After an initial white-beam[‡] slit that is used to select the central cone of undulator radiation, the energy of the x rays is selected using a double-crystal Si(111) monochromator located approximately 45 m from the source, the first crystal of which is cooled by liquid nitrogen to disperse the large heat load of the intense white beam. Such a monochromator works by adjusting the angle of incidence of the incoming x rays with the crystal such that it is a Bragg angle for the wavelength desired, as shown in Fig. 3.5. The crystal is of extremely high quality (commonly referred to as "perfect") and as such has a very sharp Bragg peak. Since Bragg's Law [Eq. (2.3)] involves both the angle θ and the wavelength λ, only x rays of the λ corresponding to the Bragg angle will be diffracted from the crystal, yielding a beam of x rays that is essentially monochromatic (although it also contains higher harmonics, see

---

[‡]Even though the radiation from an undulator is quasi-monochromatic, the x-ray beam is still called "white" if it has not yet passed through a monochromator.
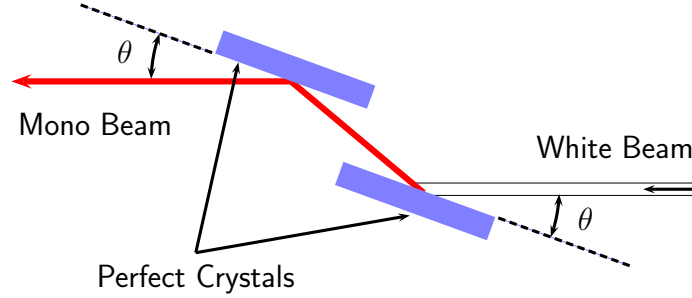
Figure 3.5: Schematic of a double-crystal monochromator. The reflection angle of each of the two crystals is adjusted such that they are equal to a Bragg angle θ. The result is that only a single wavelength (and its higher harmonics) is diffracted and passes through the monochromator. The second crystal retains the initial trajectory of the beam regardless of the angle θ chosen.

below). The second crystal of the monochromator is also tuned to the same Bragg angle and translated as needed so that the beam continues along the same trajectory regardless of the monochromator setting.

Harmonic rejection and focusing

The Bragg angle used in the monochromator to select the x ray wavelength λ is also valid for the higher harmonics in the beam ($\lambda/2$, $\lambda/3$, etc.) that will be present in the radiation from the undulator. As such, the beam will still not be entirely monochromatic after going through the monochromator. To provide harmonic rejection, the UNICAT beamline includes a set of two mirrors (arranged in the same configuration as the two monochromator crystals, Fig. 3.5, except with a much smaller reflection angle, $\sim 0.1°$). Such mirrors are designed to reflect x rays specularly from their surface with almost unit reflectivity by keeping the incident angle of the x-ray beam below the angle of total external reflection. Since this angle is energy dependent — it will be much smaller for the higher harmonics — the lowest harmonic of the beam (λ, the wavelength wanted) can be selectively reflected by choosing the reflection angle appropriately. In addition, at Sector 33ID, the first mirror is dynamically bent to allow vertical collimation or focusing of the beam. Horizontal (sagittal) focusing or collimation is done by bending the second crystal of the monochromator.

3.4.2   The SXRD Station at Sector 33ID

The actual instrument used to collect the x-ray diffraction data was the surface x-ray diffraction station in Hutch E at Sector 33ID. This end station
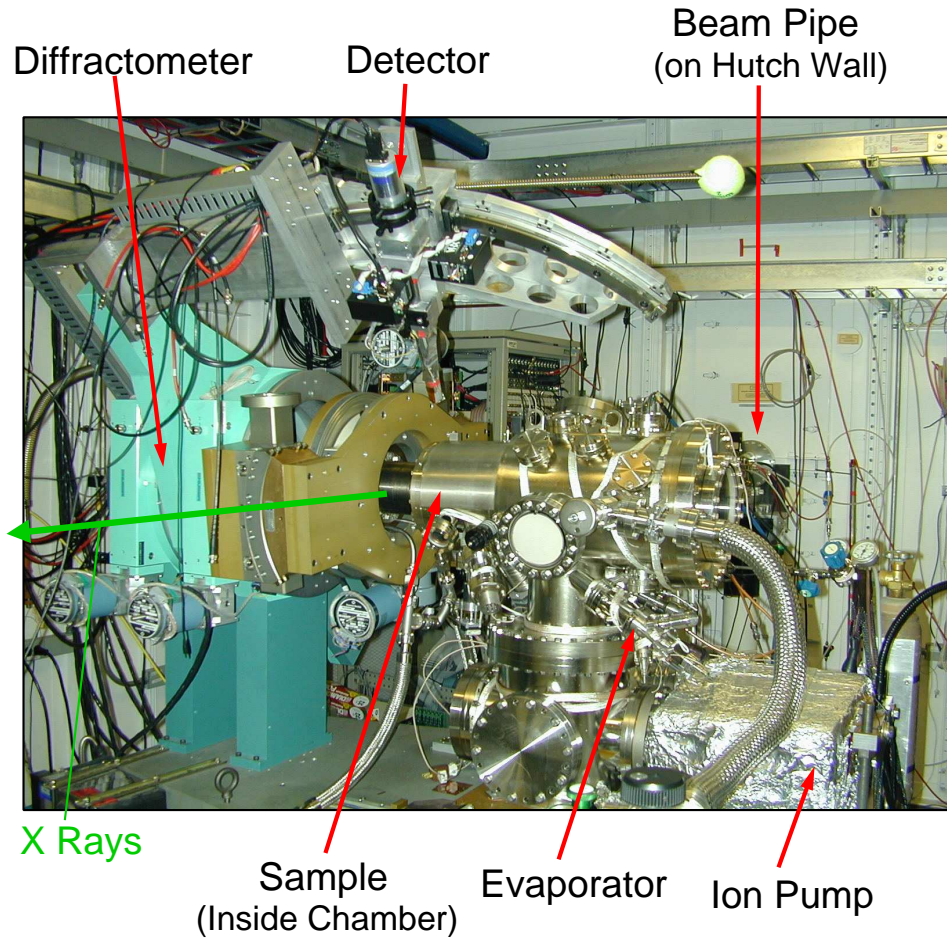
Figure 3.6: The surface x-ray diffraction station at Sector 33ID-E. The UHV chamber was specially designed and built to be integrated with a six-circle diffractometer. Various components of the setup are marked.

is shown in Fig. 3.6 with some of its components marked. It consists of a six-circle diffractometer coupled with an UHV chamber including a standard complement of surface analysis tools. The center of the chamber is located approximately 70 m from the undulator source and 23 m from the last focusing element (the first mirror) in the beamline. The x-ray beam size is defined by a pair of slits at the front of the hutch (back wall in Fig. 3.6), with typical cross-sections being about 0.5×0.5 mm^2. A nitrogen-filled ion chamber placed immediately after these slits was used as the monitor by which the scattered intensity was normalized (see Sec. 3.3.2). A removable beam pipe filled with helium gas extends from the exit of this ion chamber to within 0.3 m of the UHV chamber to reduce air scattering.

3. EXPERIMENTAL METHODS

UHV chamber and diffractometer

The UHV chamber is equipped with an ion pump and TSP and has a base pressure of approximately 6×10^{-11} torr. Under typical operating conditions pressure inside the chamber was approximately 1.5×10^{-10} torr. The system is also equipped with a reflection high-energy electron diffraction (RHEED) gun, which is used to examine the initial quality of sample surfaces or to observe different surface reconstructions while preparing the sample. Two different evaporation sources are available, mounted approximately 30° below the horizontal on the end (right side of Fig. 3.6) of the UHV chamber — a four-pocket electron-beam evaporation source and a single Knudsen cell thermal evaporator (see Sec. 3.5.1). Evaporation rates can be calibrated using a water-cooled quartz crystal thickness monitor, which can be extended from a side arm of the chamber to sit in place of the sample.

The sample is mounted vertically behind a large semi-cylindrical beryllium window that allows the incident and exiting x-ray beams to pass into and out of the UHV chamber. Two of the diffractometer angles are used to orient the surface normal of the sample such that it is horizontal and coincident with the ϕ axis of the diffractometer. These two angles are then left fixed for the rest of the experiment while the ϕ axis can be used to rotate the sample about its normal. This orientation is accomplished by reflecting a laser beam from the sample surface through a large window on the end (right side of Fig. 3.6) of the UHV chamber and rotating ϕ. When the reflected beam remains stationary through a full rotation, the sample normal is aligned with the ϕ axis of rotation. The remaining three degrees of freedom of the diffractometer are a rotation of the entire table about a vertical axis to select the incident angle α and two perpendicular rotation axes for the detector: one to select the exiting angle β and an additional horizontal rotation axis coincident with the ϕ axis for measurements of large in-plane components of momentum transfer (the δ axis). This mode of operation of the diffractometer is called the z-axis mode and its configuration is described in detail elsewhere [68].

Since all of the data is this research consists of reflectivity measurements, the δ angle was nominally set to zero and the scattering plane is then horizontal. In Fig. 3.6, the δ axis is set to a large ($\sim$45°) angle so it does not obscure the view. The detector is mounted behind a pair of slits located approximately 600 mm from the center of rotation of the diffractometer (the intersection of all its various rotation axes), to which the sample surface is oriented using survey equipment. Speed-reducing gear boxes are used on all
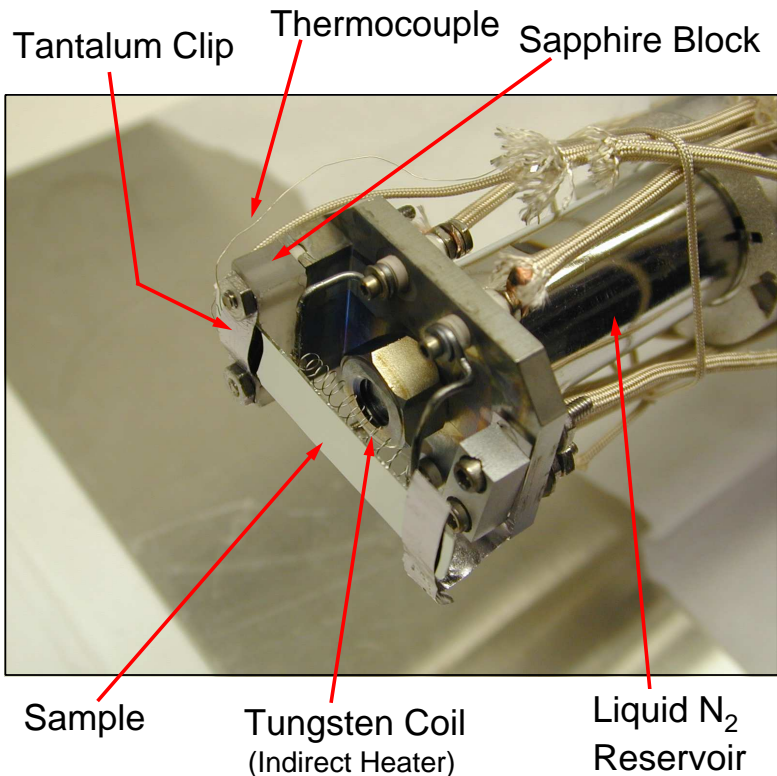
Figure 3.7: The sample mount with various components labelled.

of the stepping motors of the diffractometer to provide an angular resolution of approximately 2 arcseconds ($0.0005°$).

Sample mount

The sample mounting arm is attached to the diffractometer and is coupled to the rest of the UHV chamber via a two-stage differentially pumped rotary seal. The inner seal is pumped down to $\sim 10^{-9}$ torr via a low-volume ion pump whereas the outer seal is pump down to high vacuum pressures with a turbo pump. No bursts of pressure are observable during rotation of the sample degrees of freedom on the diffractometer. The position of the mounting arm is adjustable via an xyz stage that allows precise positioning of the sample surface with respect to the diffractometer rotation axes. Currently, no sample transfer capability is available, so to mount the sample the chamber must be brought up to atmospheric pressure and the mounting arm removed.

The actual mount for the sample is shown in Fig. 3.7 with various components labelled. The sample is thermally anchored to an open-cycle liquid nitrogen cryostat built into the end of the sample arm via a sapphire block

at one end of the sample. Due to sapphire's good thermal conductivity at low temperatures, this arrangement allows for cooling of the sample to base temperatures of $\sim$100–110 K while keeping the sample electrically isolated from the mounting arm. The temperature of the sample is monitored by a pair of thermocouples attached to the two tantalum mounting clips. The sample can be heated either by passing a direct current through the sample itself or via indirect heating from a tungsten coil positioned behind the sample. Quoted temperatures are the average of the readings from the two thermocouples, with errors in the sample temperature ranging from approximately $\pm 5°$ at base temperature (110 K) up to $\pm 20°$ at the highest annealing temperatures (300 K) during the experiment. Discrepancies in the readings of the two thermocouples indicated the presence of a thermal gradient across the sample; however, due to the small footprint of the beam — about 0.5 mm parallel to the thermal gradient — compared to the 40 mm length of the sample, the measured region of the sample can be considered to be of uniform temperature to within $\lesssim 1°$, with the quoted errors representing the confidence interval of the absolute temperature.

3.5 Sample Preparation

3.5.1 Molecular Beam Epitaxy

Deposition of elemental Pb on the substrates was done using molecular beam epitaxy (MBE). The long mean free paths in an UHV environment permit the existence of well-formed beams of atoms or molecules. MBE is the use of such beams to deposit atoms on the surface of a sample. The beam itself is produced by evaporation or sublimation of the source material from a crucible heated to high enough temperatures. The crucible itself must therefore be made from material with a high melting point, low vapor pressure, and little propensity to alloy or react with the evaporant. Common choices are molybdenum, tungsten or a ceramic such as alumina or pyrolytic boron nitride (PBN). The crucible is brought to the requisite temperature either through resistive heating (an effusion or Knudsen cell), or by electron bombardment of the crucible itself (an e-beam evaporator). Since the vapor pressure, and hence the rate of evaporation, of the source material is highly dependent on temperature, care must be taken to ensure that the temperature of the crucible is uniform and stable. For an effusion cell, this is accomplished by enclosing the crucible in multiple layers of thermal shielding and using a temperature controller with feedback from a thermocouple

near the crucible. For an e-beam evaporator, a feedback circuit monitors the emission current between the filament and crucible, which is proportional to the power dissipated by the crucible and is thus also related to its temperature, and attempts to keep it constant. In both cases, excess heat and thermal isolation of the source is maintained by water-cooling of its encasement.

The "beam" aspect of MBE can be realized by leaving only a small opening in the end of the crucible, effectively collimating the molecular beam, which can then be directed at the sample. The uniformity of the deposited film is dependent on the shape of the crucible, the distance from the source to the sample, and the position of the sample in the plume of the beam. In this research, Pb was evaporated from a PBN crucible in a Knudsen cell held at a temperature of $650 \pm 0.1°$C. The uniformity of the deposit on the sample given the distance from the evaporator (250 mm) is estimated to be within 1% across the width of the sample. The rate of deposition was calibrated with a quartz crystal oscillator — as the evaporant collects on the crystal, its resonance frequency will change slightly, which can be measured and converted to a thickness given certain physical parameters of the material.

3.5.2 Sample Pretreatment

The 10×40 mm Si(111) substrates were cut from P-doped commercial wafers with a nominal resistivity of 1–30 Ω·cm. They were attached to the sample mount as shown in Fig. 3.7 and degreased using an ultrasonic cleaner while submerged in a methanol bath. After mounting in the chamber and being pumped down to UHV pressures, any residual contaminants on the sample were removed by prolonged (4–24 hours) outgassing at $\sim$600°C. The oxide layer covering the sample surface was then removed by flashing the substrate to $\sim$1250°C for approximately 13 seconds, which reliably results in a high quality (7×7) reconstruction as verified by examining RHEED patterns and the in-plane x-ray superstructure peaks from the reconstruction. The surface was then pretreated by depositing 4.5 Å Pb on it by thermal evaporation, followed by a 10 minute anneal at $\sim$415°C to desorb the excess Pb and to form the Pb/Si(111)-$(\sqrt{3} \times \sqrt{3})R30°$ phase with an initial coverage of approximately 1.1 Pb monolayer, which is equivalent to $\frac{4}{3}$ monolayer in Si units. This pretreatment has been shown to result in bulklike termination of the Si(111) interface [48, 49, 79, 80] upon which smooth Pb films can be grown at low temperatures [41, 81]. In subsequent chapters, this initial Pb
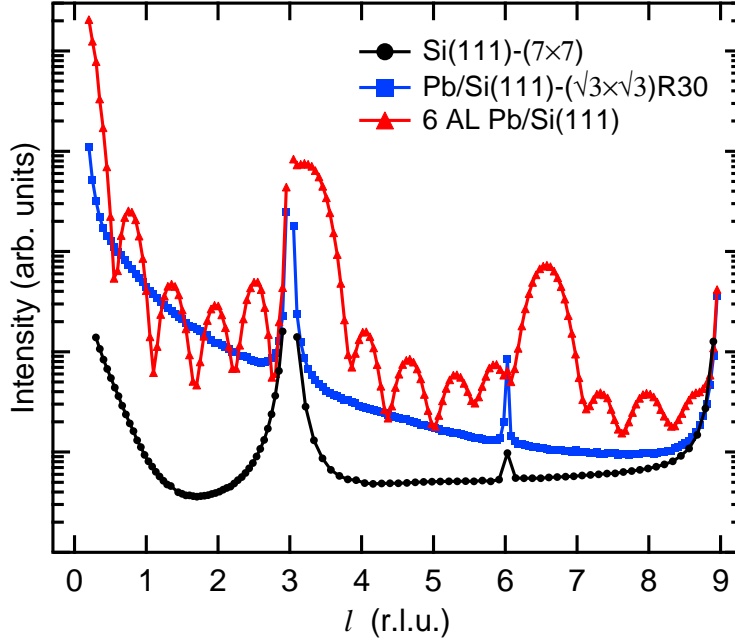
Figure 3.8: The raw specular reflectivity rod for the initial Si(111)-(7 $\times$ 7) surface (black dots), the pretreated Pb/Si(111)-($\sqrt{3} \times \sqrt{3}$)$R30°$ surface (blue squares), and a 6 AL Pb/Si(111) film grown on the Pb/Si(111)-($\sqrt{3} \times \sqrt{3}$)$R30°$ interface (red triangles).

wetting layer is included as part of the total thickness or coverage of a film.

Quality of the initial Pb/Si(111)-($\sqrt{3} \times \sqrt{3}$)$R30°$ surface was monitored by examination of the strength, width and exact location of the x-ray superstructure peaks due to the surface reconstruction [82] as well as with scans of the specular reflectivity rod. Examples of the reflectivity for a sample in various stages of treatment are shown in Fig. 3.8. The abscissa in the graph is the momentum transfer in Si(111) reciprocal lattice units, Eq. (2.32). The data shown are the raw reflectivity data as collected using the ridge scan method (see Sec. 3.6) — no background subtraction has been done and the geometric corrections discussed in Sec. 2.5.4 have not been applied. The only modifications that have been made to the data are the detector corrections discussed in Sec. 3.3.2. The reflectivity rod of the Si(111)-(7 $\times$ 7) surface is shown with black circular dots. The shoulders of the Si(111) and Si(333) Bragg peaks are clearly seen, as well as the pseudo-forbidden Si(222) peak discussed in Sec. 2.5.1. The relative intensity scale is the same for each set of data. The flat portion of the curve between $l \approx 4$ and $l \approx 8$ is due to the large background signal at higher momentum transfers.

After the pretreatment described above, the intensity between the Bragg peaks is increased significantly (blue squares), consistent with a single layer

of Pb atoms on the surface of the sample. The lack of any other peaks in the spectrum indicates that the surface is free of any buildup of Pb crystallites or islands. After deposition of approximately 5 AL of additional Pb (thus forming a film with a total thickness of 6 AL), the appearance of the Pb(111) and Pb(222) Bragg peaks is evident at $l \approx 3.3$ and $l \approx 6.6$, respectively, with four interference fringes in-between. Such a profile is similar to the N-slit interference function shown in Fig. 2.9. The Pb Bragg peaks indicate that the film has grown epitaxially with a (111) orientation. The deep minima between the interference fringes, which are shown actually going below the level of the Pb/Si(111)-($\sqrt{3}\times\sqrt{3}$)$R30°$ curve in places, are due to destructive interference from the film overlayers and indicate a high degree of uniformity in the thickness of the Pb film. Away from the Si Bragg peaks, the scattered intensity along the reflectivity rod of the 6 AL film is approximately two orders of magnitude greater than that of the bare substrate. This effect is due to the much larger electron density of Pb ($Z = 82$) compared to Si ($Z = 14$). Since the measured intensity is roughly proportional to Z^2, it will be dominated by scattering from the Pb atoms on the surface.

3.6 Collection of X-Ray Reflectivity Data

3.6.1 The Rocking Curve Method

As discussed in Sec. 2.5.3, the 2D nature of thin films results in rod-like features in reciprocal space. Although in principle these rods are one-dimensional, in reality they have a finite width due to the non-ideal nature of the sample (surface roughness, sample mosaicity, etc.). To compare experimental measurements with the intensity calculated by a kinematical model, the intensity integrated over the rod's transverse extent must be measured. In addition, the background intensity due to inelastic (Compton) scattering and TDS must be accounted for. Both of these requirements can be met by measuring the transverse rod profile at each point along the rod. In the case of the specular rod, such a scan is termed a *rocking curve* since it consists in a rotation of the sample about the y axis, defined as the axis in the plane of the surface and normal to the scattering plane (the plane formed by the vectors $\mathbf{k}_i$ and $\mathbf{k}_f$) while leaving the detector position fixed. In this manner, a cross-sectional profile of the rod is obtained as described below.

In a rocking curve scan, the momentum transfer vector is swept across the rod, measuring the intensity at positions slightly offset from the specular condition. The scattering geometry for such off-specular measurements is
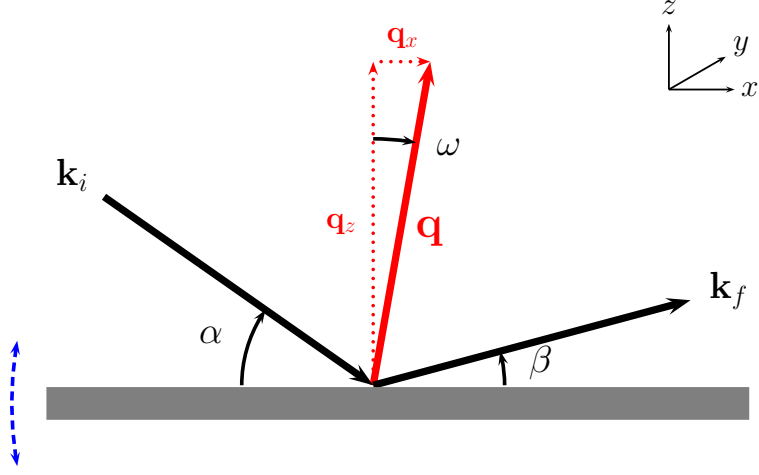
Figure 3.9: A diagram showing the scattering geometry slightly offset from the specular condition. Since $\alpha \neq \beta$, the momentum transfer has an in-plane component whereas the out-of-plane component remains nearly the same. In a rocking curve, the sample is rotated about the y axis (into the page).

shown in Fig. 3.9. In this geometry, the angle the incident x-ray beam makes with the sample surface, α, is close but not equal to the exiting angle β. If the sample normal is in the scattering plane, as it is with a rocking curve, then the scattering angle is $2\theta = \alpha + \beta$ and the momentum transfer vector has the components

$$q_x = k(\cos\beta - \cos\alpha) \tag{3.3a}$$

$$q_z = k(\sin\alpha + \sin\beta). \tag{3.3b}$$

Note that from these equations, the magnitude of **q** is

$$q = \sqrt{q_x^2 + q_z^2} \tag{3.4}$$

$$= k\sqrt{2 + 2\left(\sin\alpha\sin\beta - \cos\alpha\cos\beta\right)} \tag{3.5}$$

$$= 2k\sin\left(\frac{\alpha + \beta}{2}\right), \tag{3.6}$$

which is consistent with Eq. (2.14).

For measurements close to the specular condition, it is convenient to describe the components of **q** in terms of the offset angle $\omega = (\alpha - \beta)/2$, the
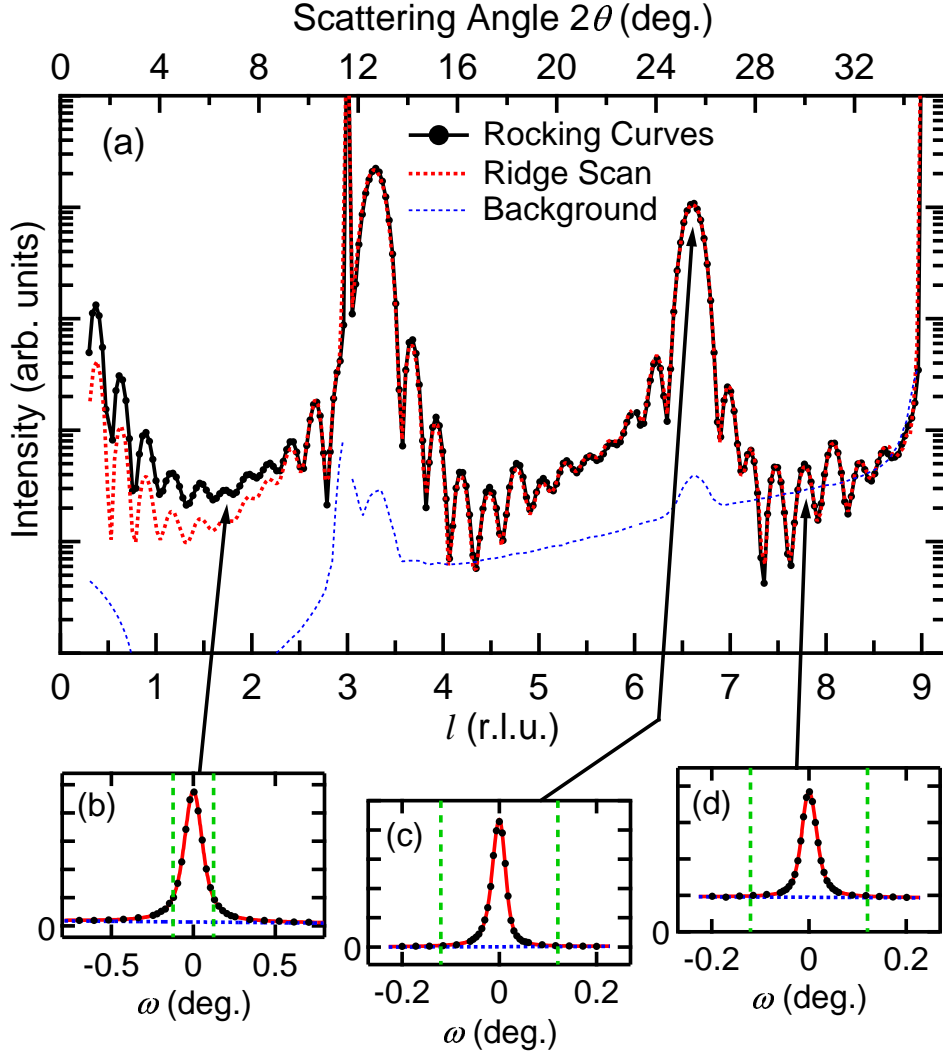
Figure 3.10: (a) comparison of the data for the reflectivity rod measured with the rocking curve method (solid black curve with points) and the ridge scan method (dotted red curve). The background found with the ridge scan method is shown as a dotted blue curve. (b)–(d) Rocking curves at $l = 1.595$, 6.62, and 7.775, respectively. The angular range integrated by the ridge scan method is shown with vertical dashed green lines. The red curves are fits to the rocking curve data with an asymmetric Voigt line shape with a linear background (blue dotted curves).

angle between $\mathbf{q}$ and the surface normal. From Fig. 3.9 is can be seen that

$$q_x = 2k \sin\left(\frac{2\theta}{2}\right) \sin\omega \tag{3.7a}$$

$$q_z = 2k \sin\left(\frac{2\theta}{2}\right) \cos\omega. \tag{3.7b}$$

If the offset angle is small, $q_z \sim q$ and $q_x \sim q\omega$. Thus, a transverse scan of
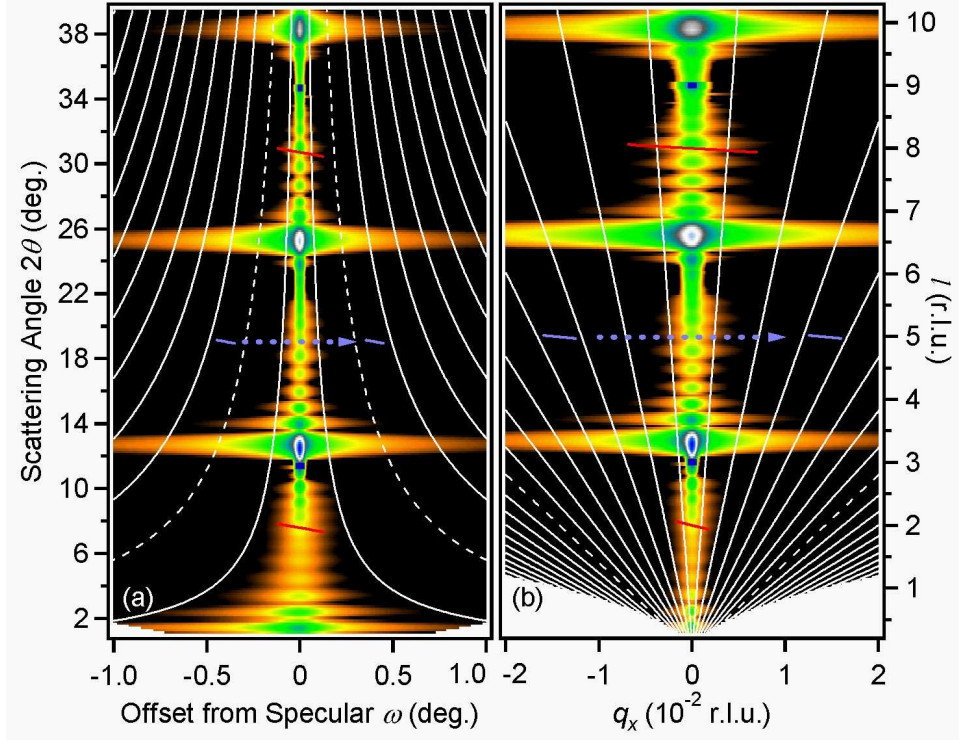
Figure 3.11: Maps of a Pb/Si(111) reflectivity rod in (a) angular space and (b) reciprocal space. The color scale represents the logarithm of the background-subtracted intensity with about five orders of magnitude represented. The white curves represent contours of constant q_x in (a) and constant ω in (b), with the dashed contours indicating the range of the x axis in the opposing image [$q_x = \pm 0.02$ r.l.u. in (a) and $\omega = \pm 1°$ in (b)]. The blank areas in the bottom corners are regions inaccessible to the diffractometer ($\alpha < 0$ or $\beta < 0$). The four slanted red lines show the cross-section of the rod measured by a 4 mm-wide detector slit, as used in the ridge scans whereas the blue lines with dashed arrows show the effect of performing a rocking curve scan with a narrower (1 mm) slit setting.

the reflectivity rod for a given q_z can be accomplished by scanning the offset angle ω at the proper 2θ. Since this procedure does not change the scattering angle, the detector remains fixed in such a scan while the sample is "rocked" about the specular condition. From the transverse profile, the rod intensity can be separated from the background and integrated. The diffraction rod resulting from a set of such rocking curves is shown as a solid black curve in Fig. 3.10(a) for a Pb/Si(111) film with a nominal thickness of 13 AL. The abscissa is this plot is l, which is q_z measured in Si(111) reciprocal lattice units, Eq. (2.32). The data points indicate l values at which rocking curves were performed, with selected examples shown in Figs. 3.10(b)–(d).

It should be noted that although the perpendicular momentum transfer is directly related to 2θ (since ω is generally very small), the transverse component is strongly coupled to both ω and 2θ. Specifically, for small

scattering angles $q_x \propto \omega \, 2\theta$. This fact results in a difference in the topology of angular (ω-2θ) and reciprocal (q_x-q_z) space. Figure 3.11(a) shows the results of the rocking curves used to determine the data in Fig. 3.10. Each rocking curve is an ω scan for a specific value of 2θ and thus corresponds to a single horizontal row in the image. In this manner, a map of the diffraction rod in angular space can be created. Since the width of the rod varies along its length, rocking curves at different 2θ values require different step sizes. To create an evenly spaced grid of points for the image, each rocking curve was fit to an asymmetric Voigt curve (a convolution of a Gaussian and Lorentzian). To illustrate the different topology of angular space with respect to reciprocal space, the white lines in the image show contours of constant q_x, calculated using Eq. (3.7a). As can be seen, the width of the rod appears to follow the q_x contours, which is especially noticeable as $2\theta \rightarrow 0$, where the rod appears to flare out. The reason for this effect is that the diffraction rod is really a feature in reciprocal space, and as such will follow its topology. This fact is explicitly demonstrated in Fig. 3.11(b), which shows the same data as Fig. 3.11(a) but transformed into reciprocal space. The white lines in this case show contours of constant ω. In reciprocal space, the flaring-out effect is not present and the rod width is nearly uniform as a function of l.[§] Since the rod is measured in angular space, it will appear to be broader at smaller scattering angles. Since scattering at $\alpha < 0$ or $\beta < 0$ cannot be measured (blank areas in the bottom corners of Fig. 3.11), eventually the width of the rod in angular space is so large that the background cannot be accurately determined. This widening of the rod in angular space also has important ramifications for the ridge scan method discussed in Sec. 3.6.2.

It is important to understand exactly what portion of reciprocal space is being measured by a rocking curve scan. The detector has a finite active area defined by a pair of slits. This active area itself effectively integrates the intensity over a 2D surface in reciprocal space. During the rocking curve scan, this surface is swept through reciprocal space to integrate over a 3D volume. The dimensions of this integration volume will determine the resolution of the rod measurement. This effect is illustrated in Fig. 3.12, which shows a diagram representing the scattering geometry projected onto the scattering (xz) plane. For a given incident angle α, a range $d\beta$ of exiting beams will be collected by the detector, corresponding to the angular ac-

---

[§]A slight broadening is evident at high values of l; however, this effect is due to the convolution of the signal with the finite angular width of the slit used to measure the rocking curves and is not due to actual broadening of the diffraction rod itself.
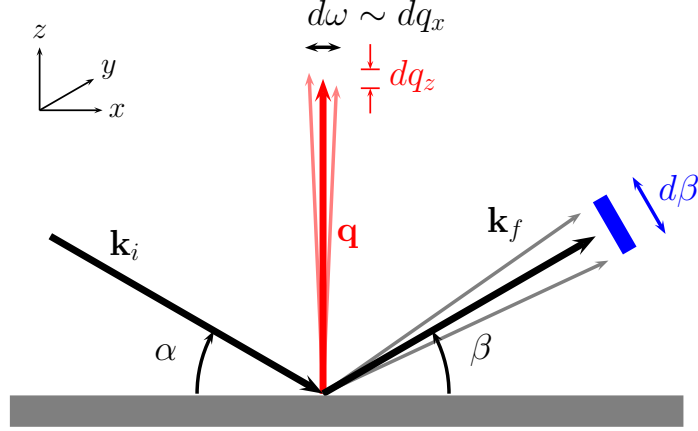
Figure 3.12: A diagram showing the range of momentum transfer collected by the detector slits. For different β values, the orientation and length of the **q** vector is different, which collects a slightly diagonal slice of reciprocal space that has a finite width in q_z and effectively integrates over a range of ω (or q_x).

ceptance of the slits. Each of these beams corresponds to a slightly different **q** vector. The orientation of each **q** vector will be slightly offset from the surface normal (z axis) by an amount $d\omega = -d\beta/2$, which from Eq. (3.3a) corresponds to a variation

$$dq_x = -k\,d\beta\sin\beta \tag{3.8}$$

in reciprocal space. Similarly, from Eq. (3.3b) the range of q_z values which are collected by the detector throughout the scan is

$$dq_z = k\,d\beta\cos\beta. \tag{3.9}$$

The surface in reciprocal space over which the slits integrate is thus approximately a rectangle that extends in the y direction (perpendicular to the page in Fig. 3.12) due to the width of the slits normal to the scattering plane, and whose other edge is a slanted line segment in the xz plane. The values of dq_x and dq_z indicate the reciprocal space lengths between the endpoints of this line segment. Examples of the projection of this 2D rectangular surface onto the scattering plane (i.e., the line segment profile of the rectangle) are shown in Fig. 3.11 as red and blue lines. A rocking curve scan is therefore equivalent to sweeping one of these rectangles across the diffraction rod in the x direction, as shown with the blue dashed arrows. Such a scan will integrate a slice of the rod that has a thickness of dq_z. Since $dq_z \propto \cos\beta$, the thickness of this rod slice will vary as we move along the rod. This is

the origin of the rod interception correction factor discussed in Sec. 2.5.4.

In the case of 3D crystallography, where rocking curves are commonly used to measure the integrated intensities of Bragg peaks, the detector slits are opened relatively wide for the scan to maximize the integration volume. In that case, the Bragg peak is nominally a zero-dimensional feature (point) in reciprocal space. However, in surface diffraction, the features of interest are quasi-1D objects (rods), along which the intensity as a function of q_z is desired. In addition, the background surrounding these rods can be significant and must be taken into account. In this case, the preferred integration volume is a 2D cross-sectional slice of the rod that retains as much resolution in q_z as possible. As a result, the detector slits are generally narrowed to minimize $d\beta$ and hence dq_z.

To summarize, the rocking curve method measures a cross-sectional profile of the diffraction rod for an approximately constant q_z value. From this profile, the background can be found and the rod intensity integrated. This method provides accurate rod intensities for a wide range of q_z values. However, since an individual scan must be carried out for each q_z point along the rod, it requires a great deal of time both to collect the data and in its analysis. Since a high-demand synchrotron is generally used to do the experiment, this limitation may be significant.

3.6.2 The Ridge Scan Method

As mentioned in the last section, the acceptance area of the detector itself integrates over a 2D surface in reciprocal space. If the diffraction rod is sufficiently sharp in the transverse directions, a 2D cross-sectional slice of the rod can be measured without rocking the sample at all by using sufficiently wide detector slit settings. In this manner, the integrated intensity of a point on the rod is obtained directly with a single setting of the diffractometer. This type of measurement is illustrated in Fig. 3.11 with slanted red lines. This cross-section is truly a 2D slice of the rod, unlike the 3D volume that is integrated with a rocking curve. In that case, the (narrower) slits were scanned across the diffraction rod, as shown with the blue lines and arrows. In the ridge scan method, a wider slit setting is used (hence the longer line in the figure) and the measurement is taken directly at each point along the rod. Since the rod is integrated over a 2D surface instead of a 3D volume, the rod interception factor described in Sec. 2.5.4 is not needed.

The integrated intensity of the rod as a function of q_z can thus be obtained by scanning α and β simultaneously while keeping $\alpha = \beta$ ($\omega = 0$).

3. EXPERIMENTAL METHODS

This type of scan is commonly referred to as a θ-2θ scan, since both the scattering angle and the incident angle (which is equal to half the scattering angle for the specular rod) are varied during the scan. This type of scan is equivalent to sweeping the slit profile shown at the bottom of Fig. 3.11(a) in a straight line up the middle of the map. The background level for each point along the rod can be obtained by performing a similar type of scan with an offset between α and β; i.e., with $\omega \neq 0$. In this work, the background for each ridge scan was obtained by taking the average of two scans, one with $\omega = 1°$ and another with $\omega = -1°$. Such background scans can be visualized in Fig. 3.11(a) as sweeping up straight vertical lines in angular space at the edges of the map. The results of using the ridge scan method to measure the Pb/Si(111) specular rod in Fig. 3.11 is shown in Fig. 3.10 as a red dotted curve. In both cases, the curves represent the background subtracted integrated intensity of the specular rod, with the experimental corrections described in Secs. 2.5.4 and 3.3.2 applied. Since the two methods measure intensities on incompatible scales (the rocking curves integrate over a 3D volume of reciprocal space whereas the ridge scan integrates over a 2D surface), the ridge scan curve was multiplied by a scale factor to show the two results on the same scale. The average of the two background scans that were subtracted from the ridge scan is also shown in the figure as a light dotted blue curve.

The results from the two methods are essentially equivalent for $l > 2.5$. However, for the lower portion of the rod, the ridge scan method consistently measures a lower intensity than the rocking curve method. The reason for this discrepancy is that the size of the 2D surface used to integrate the transverse profile of the diffraction rod is defined by the angular acceptance of the detector slits. It is therefore a constant size in *angular space*. That is, the ridge scan samples a vertical swath of constant width in Fig. 3.11(a). However, as discussed in the last section, the diffraction rod appears to broaden considerably in angular space as $l \to 0$, following the contours of constant q_x. At lower momentum transfers, the 2D integration surface is no longer wide enough in reciprocal space to sample the entire rod cross-section. This effect is illustrated in Figs. 3.10(b)–(d), where the angular range sampled by the slits used to obtain the ridge scan data is shown with vertical dashed green lines. In Figs. 3.10(c) and (d), the range collected by the slits clearly integrates over the full rod width whereas in Fig. 3.10(b), part of the rod intensity is not collected (note the different scale for ω). Therefore, the ridge scan method is only effective for obtaining integrated rod intensities for larger momentum transfers (in our case, for $l > 2.5$).

Since this study focuses on the extended reflectivity, this limitation is not overly restrictive.

Even though the ridge scan method is limited in the range of momentum transfer that it can measure, it also possesses certain advantages over the rocking curve method. First, since the diffraction rod is integrated over a 2D surface, the ridge scan method provides exceptionally high-resolution data in q_z. In contrast, the rocking curve method always integrates a rod slice of finite thickness which limits its resolution in q_z. More significantly though, the ridge scan method requires only a fraction of the amount of time to acquire a full set of extended reflectivity data compared to the rocking curve method. With the ridge scan method, the background-subtracted integrated intensity of the full rod can be measured with just three scans (one for $\omega = 0$ for the specular intensity and two background scans at $\omega = \pm 1°$), whereas a separate scan must be done for each point along the rod with the rocking curve method. For example, the data in Fig. 3.10 represents the results of 280 individual rocking curves, each of which needed to be individually analyzed to determine the background and to remove any spurious data points. Measuring the full diffraction rod using the rocking curve method may take 10–20 hours, depending on the spacing desired between the points along the rod. In contrast, measuring the diffraction rod using the ridge scan method only takes about 20–40 minutes. For experiments such as those conducted in Chapters 5 and 6, where the specular rod of the same sample may need to be measured dozens of times (at different temperatures or thicknesses), the ridge scan method is a necessity given the time constraints of a synchrotron facility.

The ridge scan method provides a technique for measuring the upper portion of the reflectivity rod (the extended reflectivity) at high resolution and in a short amount of time. For lower momentum transfers, the width of the diffraction rod must be measured to ensure that the detector slits in the ridge scan collect the full integrated intensity of the rod. In practice, this can be verified by doing sample rocking curves to measure the transverse rod profile. The angular width of the slits needed to integrate the entire rod width is then approximately twice the full width of the peak in the rocking curve ($d\beta \approx 2d\omega$). In our case, it was found that with the slit setting used, the full rod intensity was collected for $l > 2.5$. For this reason, only data for these momentum transfers were used in the experimental analyses.

3.6.3 Error Analysis

Since the diffraction data were collected with a scintillation detector, which produces pulses that are counted, the statistical distribution of the raw intensity data should follow a Poisson distribution with a standard error of $\sqrt{N_0}$ where N_0 is the number of pulses counted before background subtraction and signal normalization. The fractional error in this case is thus $1/\sqrt{N_0}$. Since typical count rates were on the order of 10^4–10^5 c/s, the fractional errors due to statistical deviations were only about 0.3–1.0%. To account for a certain degree of systematic error in the measurements (sample misalignments, etc.), the statistical errors were combined quadratically with a 5% systematic error. Due to the high count rates, generally the bulk of the standard deviations for each data point are due to systematic errors.

In the process of doing the least-squares fits to the experimental data, a reduced χ^2 measure of the fit quality was used:

$$\chi^2 = \frac{1}{\mathcal{N} - \mathcal{M}} \sum_{i=1}^{\mathcal{N}} \frac{[y_i - f(x_i)]^2}{\sigma_i^2} \qquad (3.10)$$

where $\mathcal{N}$ is the number of points in the data set, $\mathcal{M}$ is the number of free parameters in the model (thus, $\mathcal{N} - \mathcal{M}$ is the number of degrees of freedom), $y_i = N_0/N_m$ is the normalized count rate for data point i (N_m is the monitor count discussed in Sec. 3.3.2), x_i is its corresponding abscissa value, $f(x)$ is the model function, and σ_i is the standard error for data point i. As described above, in our case the standard error is

$$\sigma^2 = \frac{\left(\sqrt{N_0}\right)^2 + (0.05\, N_0)^2}{N_m^2}, \qquad (3.11)$$

so

$$\sigma_i^2 = \frac{y_i}{N_m} + 0.025\, y_i^2. \qquad (3.12)$$

Thus, when $\chi^2 \approx 1$ the model function describes the data to within the experimental error of the measurements. Due to the multitude of different factors that influence the form of a reflectivity curve, typical χ^2 values for the best fits to the experimental data in Chapters 5 and 6 were generally in the range $\chi^2 = 5$–10.

4 Free-Electron Models

4.1 Introduction

In an attempt to capture the essential physics of an ultrathin metal film, it is reasonable to approximate the system as a free-electron gas confined to a one-dimensional quantum well. This chapter develops a set of such models to describe some of the various thickness-dependent effects that arise due to quantum confinement of a metal film's itinerant electrons by its physical boundaries (QSE) [83, 84]. The free-electron assumption in itself limits the direct applicability of the unmodified models for the quantitative analysis of actual experiments. However, as will be seen, the addition of certain phenomenological factors can be done to mimic some of the physical realities of the system. The modified models are found to provide an adequate description of the actual films studied, as long as they are interpreted within the proper context.

Adhering to the theme of simplicity, most of the models presented are based upon a quantum well with infinite bounding potentials. Such a simplification enables us to derive analytic formulas for the wave functions of the confined electrons and the surface energy. The availability of an analytic solution is conducive to incorporating the results of the model calculation into a fitting algorithm with adjustable parameters that can be used to interpret experimental data. Since such a routine may need to recalculate the model results thousands or even millions of times before arriving at an acceptable fit to the data, models that rely upon first-principles calculations or that are purely numerical are not well-suited for incorporation into such algorithms due to their computationally intensive nature.

That being said, the finite quantum well model is explored at the end of the chapter for the sake of comparison. Conceptually it lacks the simplicity of the infinite well model. However, the finite well model offers an alternative perspective within the free-electron framework. In the end, the results of the finite well model are very similar to those found using the modified infinite well model and as such offer a certain degree of validation that they are accurate and physically reasonable.

Before the specific models are presented, a certain theoretical base is developed. First, in Sec. 4.2 the effects of quantum confinement on the charge density inside an infinite well are described. Second, due to the discrete quantum well states that arise, the Fermi level in a film is not necessarily equal to that in the bulk material. This effect and different viewpoints on how to approach it are discussed in Sec. 4.3, where it is found that the charge density oscillations of Sec. 4.2 provide valuable insight as to the physical phenomena involved.

In the last two sections of the chapter, two different physical effects are discussed in detail. The first is related to the Friedel-like oscillations in the electronic charge density that arise at the film boundaries. Since the ionic cores in the film's crystalline lattice have a net positive charge, it is reasonable to expect them to respond to these electron density oscillations, causing lattice distortions with a corresponding periodicity. Two similar models are developed to describe these lattice distortions, which are used in Chapter 5 to help explain the atomic-layer structure of thin Pb/Si(111) films.

The second effect is oscillations in the surface energy as a function of thickness. These oscillations will be studied experimentally in Chapter 6, where it will be found that films annealed to a state of quasi-equilibrium have a wide distribution of thicknesses. The distributions are not smooth, though, indicating that some thicknesses are more stable than others, corresponding to variations in the surface energy of the film. In Sec. 4.5, a model for this effect within the free-electron context is presented, the functional results of which are used in Chapter 6 to aid in the data analysis.

4.2 Charge Density

In the infinite well model, the free-electron wave function is subject to the boundary conditions

$$\Psi \to 0 \qquad \text{at} \qquad z = 0, D \qquad (4.1)$$

where D is the width of the quantum well. The Fermi sphere of allowed electronic states is correspondingly reduced to a series of subbands, as shown in Fig. 4.1, each having a wave function

$$\Psi_{\mathbf{k}}(\mathbf{r}) = \sqrt{\frac{2}{V}} e^{ik_x x + ik_y y} \sin(k_z z) \qquad (4.2)$$
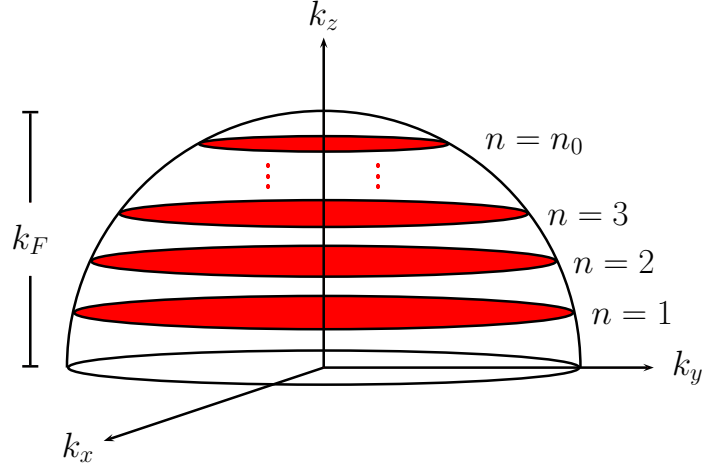
Figure 4.1: Due to confinement of the itinerant electrons in the film to a quantum well, the Fermi sphere of allowed states is reduced to a set of subbands along the direction of confinement. The quantum number of the highest occupied subband is denoted with n_0.

where V is the volume of the system, the index k_z can take on the values

$$k_z = \frac{\pi n}{D} \qquad n = 1, 2, 3, \ldots, n_0, \tag{4.3}$$

and the quantum number of the highest occupied subband is

$$n_0 = \text{int}\left(\frac{k_F D}{\pi}\right). \tag{4.4}$$

Thus, the wave functions for the electrons in each subband are that of a free particle in the xy plane (the plane of the film) and a standing wave in the z direction. The electronic charge density at a point in a free-electron gas is in general found by integrating over the Fermi sphere,

$$\rho_e(\mathbf{r}) = \frac{2V}{8\pi^3} \int_{|\mathbf{k}|<k_F} (-e)|\Psi_{\mathbf{k}}(\mathbf{r})|^2 d^3\mathbf{k}, \tag{4.5}$$

where e is the magnitude of the charge of an electron and k_F is the Fermi wave vector. However, in this case, $|\Psi_{\mathbf{k}}(\mathbf{r})|^2 = \frac{2}{V}\sin^2(k_z z)$, which is only a function of z, as required by the translational symmetry of the system in the xy plane. In addition, the Fermi sphere is no longer uniformly occupied, but is divided up into a series of discrete Fermi disks. Thus, the electronic

charge density at a point $0 \leq z \leq D$ in the quantum well is

$$\rho_e(z) = -\frac{e}{2\pi^3} \int_0^{k_F} dk_z \, \pi \left(k_F^2 - k_z^2\right) \sin^2(k_z z) \sum_{n=1}^{n_0} \frac{2\pi}{D} \delta\left(k_z - \frac{\pi n}{D}\right) \quad (4.6)$$

$$= -\frac{e}{\pi D} \sum_{n=1}^{n_0} \left[k_F^2 - \left(\frac{\pi n}{D}\right)^2\right] \frac{1}{2} \left[1 - \cos\left(\frac{2\pi nz}{D}\right)\right]. \quad (4.7)$$

The summation can be divided up into a portion which is constant with respect to z and an oscillatory component:

$$\rho_e(z) = -\frac{e}{2\pi D} \left[C_D - \left(k_F^2 + \frac{1}{4}\frac{\partial^2}{\partial z^2}\right) S_D\left(\frac{2\pi z}{D}\right)\right] \quad (4.8)$$

where C_D is given by

$$C_D = \sum_{n=1}^{n_0} \left[k_F^2 - \left(\frac{\pi n}{D}\right)^2\right] \quad (4.9)$$

$$= n_0 k_F^2 - \left(\frac{\pi}{D}\right)^2 \frac{1}{6} n_0(n_0 + 1)(2n_0 + 1), \quad (4.10)$$

and S_D is the dimensionless geometric sum

$$S_D(x) = \sum_{n=1}^{n_0} \cos(nx) \quad (4.11)$$

$$= \frac{1}{2}\sin(n_0 x) \cot\left(\frac{x}{2}\right) - \sin^2\left(\frac{n_0 x}{2}\right). \quad (4.12)$$

The subscripts on S_D and C_D are a reminder that both of these quantities will change with the size of the quantum well. The oscillatory behavior of ρ_e is thus captured in S_D, which gives rise to a n_0-slit interference pattern with a characteristic wavelength of $D/n_0 \approx \pi/k_F = \lambda_F/2$ (one half of the Fermi wavelength). To focus on the oscillatory component, the self-normalized charge density variations may be considered:

$$\delta\rho(z) \equiv \frac{\rho_e(z) - \langle\rho_e(z)\rangle}{\langle\rho_e(z)\rangle} \quad (4.13)$$

$$= -\frac{1}{C_D} \left(k_F^2 + \frac{1}{4}\frac{\partial^2}{\partial z^2}\right) S_D\left(\frac{2\pi z}{D}\right) \quad (4.14)$$

where $\langle\cdots\rangle$ indicates the average over z. An example of this quantity is shown in Fig. 4.2 as a solid curve, where it exhibits sinusoidal oscillations that dampen away from the film boundaries (vertical dashed lines).

Note that in the limit $D \to \infty$, our system changes from a quasi-two-
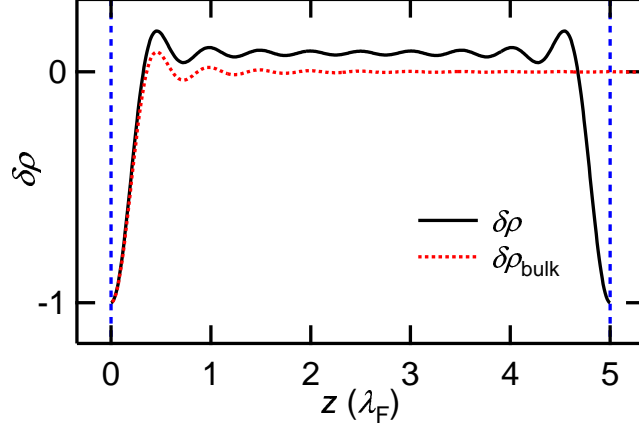
Figure 4.2: The self-normalized charge density variations in a metal film (solid curve) exhibit strong oscillations with a wavelength of $\lambda_F/2$, which dampen away from the film boundaries. In the bulk limit (red dotted curve), they are identical to the normal Friedel oscillations found near the surface of bulk metals.

dimensional film into a semi-infinite slab. In this limit,

$$S_D(x) \rightarrow \int_0^{k_F} \cos\left(\frac{k_z Dx}{\pi}\right) \frac{D}{\pi} dk_z \tag{4.15}$$

$$= \frac{1}{x} \sin\left(\frac{k_F Dx}{\pi}\right) \tag{4.16}$$

$$C_D \rightarrow \int_0^{k_F} \left(k_F^2 - k_z^2\right) \frac{D}{\pi} dk_z \tag{4.17}$$

$$= \frac{D}{\pi} \frac{2}{3} k_F^3 \tag{4.18}$$

and Eq. (4.14) becomes

$$\lim_{D \to \infty} \delta\rho(z) = -\left(\frac{4}{3}k_F^3\right)^{-1} \left(k_F^2 + \frac{1}{4}\frac{\partial^2}{\partial z^2}\right) \frac{1}{z} \sin(2k_F z) \tag{4.19}$$

$$= -\frac{3}{2}\left(1 + \frac{\partial^2}{\partial u^2}\right) \frac{\sin u}{u} \tag{4.20}$$

$$= 3\left(\frac{\cos u}{u^2} - \frac{\sin u}{u^3}\right) \tag{4.21}$$

where the substitution $u = 2k_F z$ has been made. This equation is the familiar form of the Friedel oscillations in the electron density near the surface of a bulk metal, which one would expect to recover in this limit. For comparison, these regular Friedel oscillations are shown in Fig. 4.2 for a semi-infinite bulk metal (dotted curve).

When D is sufficiently large, the charge density variations are well rep-

resented by the superposition of the Friedel oscillations due to the two film boundaries. Intuitively, the Friedel oscillations derived from the two boundaries can overlap and interfere as D becomes small, but the situation is actually more complicated. The Friedel oscillations in a bulk metal arise due to the upper limit to the wave vector (the Fermi level) of electronic states available as Fourier components and the pinning of their relative phases due to the loss of translational symmetry. The states that are available, though, form a continuum from $k = 0$ to k_F. In the case of a thin film, the electron wave functions are pinned in phase by both boundaries, giving rise to interference effects. Furthermore, the continuum of k states is reduced to a set of subbands, as shown in Fig. 4.1. This reduction in the Fourier basis set can also lead to differences from the bulk. In short, charge oscillations in $\rho_e(z)$ and $\delta\rho(z)$ for a film are the result of a phased sum of a discrete set of subband wave functions. One distinct difference between the film's density oscillations and the bulk Friedel oscillations is that the charge density variations in the film do not oscillate about the *average* charge density of the film (which would correspond to $\delta\rho = 0$), but a value slightly larger. This effect will have important consequences for the Fermi level.

4.3 Fermi Level

As the size of the quantum well gets smaller, the separation between the subbands will get wider and the number of available states will decrease. There are two consequences of this that need to be recognized. First, the number of occupied electronic states (i.e., the total number of electrons) in the quantum well will not necessarily be proportional to the film thickness if one assumes a fixed Fermi level. Second, as can be seen in Fig. 4.2, the charge density variations have tails at the film boundaries. As a result, regions of electron depletion are present near the film boundaries. To compensate, a net charge builds up in the rest of the film, which produces a charge imbalance. Both of these effects can be compensated for by an appropriate adjustment of the Fermi level as a function of thickness and by letting the quantum well width expand slightly at the film boundaries so that the electron density can tunnel slightly past the classical boundaries of the film. Specifically, there are two different constraints that can be applied to the model:

Constraint #1: Charge neutrality. The number of electrons in the theoretical quantum well is required to be equal to the number of electrons one expects to find in the film given the bulk electron density of the material.

This constrains the film to be electrically neutral overall, which is appropriate for free-standing slab calculations, but not necessarily for supported films, where an interface charge layer can form.

Constraint #2: Charge balance. The average electronic charge density in the middle of the quantum well is balanced with the constant positive background due to the ion cores; i.e., the total charge density oscillates about zero. This constraint minimizes the net electric field in the film and hence also its Coulomb energy.

Although similar, these two constraints are distinct from each other — charge neutrality (Constraint #1) is not necessarily equivalent to charge balance (Constraint #2). In the bulk, there is no distinction since boundary effects are negligible, but in the case of a film, both constraints are satisfied only under very special circumstances, as will be seen below.

In the simplest case, the width of the quantum well is $D = Nt$, where t is the average interlayer spacing of the film. This width is also the extent of the positive uniform background in the jellium model and will be referred to as the classical width of the film since it ignores any boundary effects and is appropriate in the $D \to \infty$ limit. However, in this case the infinite boundary potentials do not allow any of the electronic charge density to spill past the classical boundaries of the film. Nonetheless, such a scheme represents a reasonable starting point for discussion. A more realistic treatment of the boundary conditions will be introduced later.

To enforce charge neutrality (Constraint #1), the diminishing number of occupied states for decreasing film thickness must be compensated by an appropriate adjustment of the Fermi level. Given the thickness, the total number of electrons in the film is

$$N_e = N_{\text{val}} N \frac{A}{A_{\text{cell}}} \tag{4.22}$$

where N is the number of atomic layers in the film, A is the surface area of one film interface, N_{val} is the number of itinerant valence electrons per atom of film material ($N_{\text{val}} = 4$ for Pb), and A_{cell} is the area of the surface unit cell. In contrast, the total number of electrons in the theoretical quantum
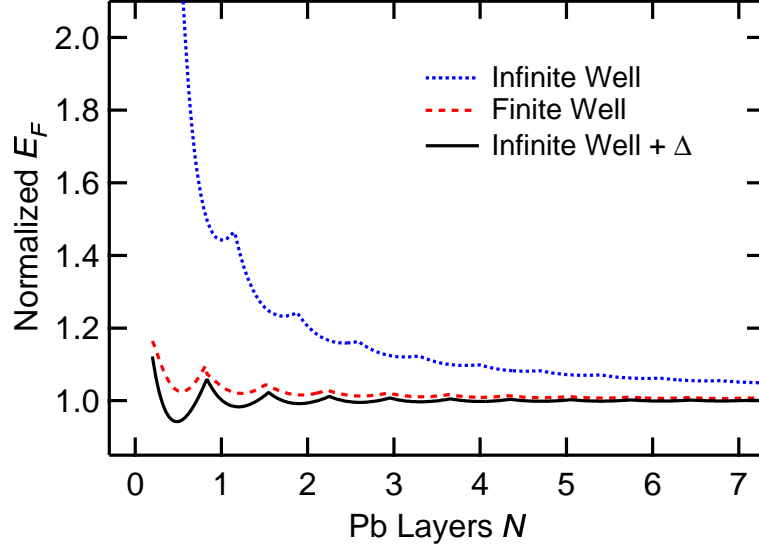
Figure 4.3: The Fermi energy of a Pb(111) film as a function of thickness, normalized to its bulk free-electron value. In the infinite well model, when the quantum well width is exactly equal to Nt, the Fermi level rises drastically as the film thickness decreases (dotted curve) to compensate for the areas of electron depletion near the film boundaries (see Fig. 4.4). However, if the electron density is allowed to spill past the classical film boundaries, such compensation is unnecessary and the Fermi level oscillates about its bulk value (solid curve). This Fermi level is very similar to that found in a model where the bounding potentials are finite (dashed curve).

well is calculated by summing over the allowed subbands

$$N_e^{\mathrm{QW}} = \frac{2V}{8\pi^3} \int_{|\mathbf{k}|<k_F} d^3\mathbf{k} \sum_{n=1}^{n_0} \frac{2\pi}{D} \delta\left(k_z - \frac{\pi n}{D}\right) \tag{4.23}$$

$$= \frac{V}{2\pi^2 D} \sum_{n=1}^{n_0} \pi \left[k_F^2 - \left(\frac{\pi n}{D}\right)^2\right] \tag{4.24}$$

$$= \frac{A}{2\pi} C_D \tag{4.25}$$

where C_D is defined in Eq. (4.10). Setting $N_e^{\mathrm{QW}} = N_e$ yields the constraint

$$\boxed{C_D = \frac{2\pi N_{\mathrm{val}} N}{A_{\mathrm{cell}}}.} \tag{4.26}$$

The results of solving this constraint for the Fermi energy, $E_F = \frac{\hbar^2 k_F^2}{2m_e}$, are shown in Fig. 4.3 (dotted curve) normalized to the bulk free-electron value. As $D \to 0$ the Fermi energy rises steeply and for the first few integer N thicknesses, the Fermi level is up to $\sim$40% larger than its bulk value. Cusps are also evident at thicknesses where an additional subband becomes occupied
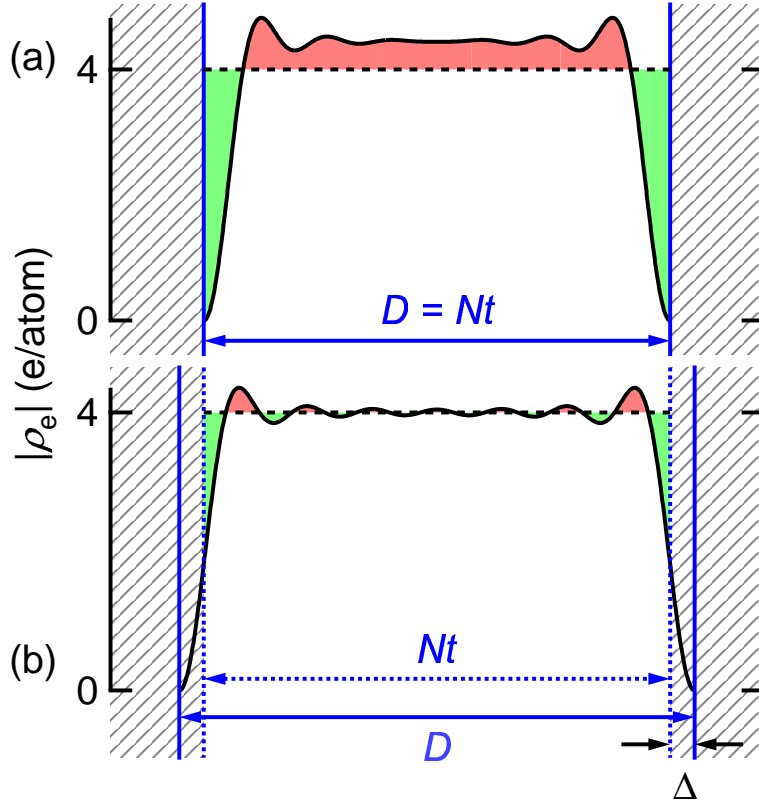
Figure 4.4: Charge density profiles for a quantum well with $N = 5$. (a) Assuming the boundary potentials are infinite in magnitude, the electronic charge density is forced to zero at the film boundaries, causing an area of electron depletion (shaded areas below $|\rho_e| = 4$, the background charge density from the Pb ion cores). To compensate, the inner portion of the film takes on a net charge. (b) If the charge density is allowed to spill past the classical boundaries of the film, as happens in a real film, this effect can be minimized.

(i.e., when n_0 increases discontinuously) as the film thickness increases.

The steep rise in E_F is specific to the infinite boundary potentials, since it is not present in a finite well model (dashed curve in Fig. 4.3, see Sec. 4.5.3). The infinite boundary potentials force the wave functions of all the quantum well states to go to zero, creating an area of electron depletion near the film boundaries, as illustrated in Fig. 4.4(a) with electron density profiles as calculated in Sec. 4.2. In order to satisfy the condition of overall charge neutrality, Eq. (4.26), the electron density in the center portion of the quantum well must get ever larger with respect to the positive background as the film thickness decreases to compensate for these areas of electron depletion. This charge imbalance leads to a net electric field inside the metal film. However, in a real metal film the confining potentials are not infinite and the electron density will spill slightly past the classical boundaries of

the film, reducing the region of electron depletion. To simulate this aspect of the system, define the well width to be

$$D = Nt + 2\Delta \tag{4.27}$$

where Δ is the distance the quantum well is allowed to expand at each boundary to allow for some charge spillage. This procedure is analogous to the boundary phase shifts that are often employed in quantum well analyses [36]. For now, the symmetric case will be considered where the charge spillage at each interface is the same, which is not the case for an actual supported film.

The charge imbalance that results in the steep rise in E_F is minimized when the electronic charge density oscillates about the constant positive background level due to the ionic cores; i.e., when Constraint #2 is satisfied. This condition is obtained by extracting the non-oscillatory component of Eq. (4.8)

$$\overline{\rho_e} = -\frac{e}{2\pi D}\left(C_D + \frac{1}{2}k_F^2\right). \tag{4.28}$$

Note that this quantity is distinct from the *average* electronic charge density, $\langle\rho_e(z)\rangle$, which is equal to the first term only — the quantity S_D has a zero integral between $z = 0$ and D, but oscillates about the value $-\frac{1}{2}$ away from the boundaries, as can be seen from Eq. (4.12). This difference results from the charge spillage tails in $\rho_e(z)$ at the film boundaries, as seen in Fig. 4.4. In the limit $D \to \infty$, the effects of the interfaces become negligible, $C_D \propto D$ and $\overline{\rho_e} \to \langle\rho_e(z)\rangle$. This discrepancy is also evident in Fig. 4.2, where the self-normalized charge density variations for the film can be seen to oscillate about a value slightly larger than zero. The condition of charge balance is thus obtained when $\overline{\rho_e}$ is equal to the magnitude of the constant positive (jellium) background

$$\overline{\rho_e} = -\frac{N_{\mathrm{val}}\,e}{A_{\mathrm{cell}}t}, \tag{4.29}$$

which when combined with Eq. (4.28) yields

$$\boxed{C_D = \frac{2\pi N_{\mathrm{val}}D}{A_{\mathrm{cell}}t} - \frac{1}{2}k_F^2.} \tag{4.30}$$

This constraint is very similar in form to Eq. (4.26). Note that if $D = Nt$, both constraints are only satisfied in the limit $N \to \infty$. However, with $D \neq Nt$ there are two degrees of freedom that can be used to meet these two constraints: k_F and Δ.
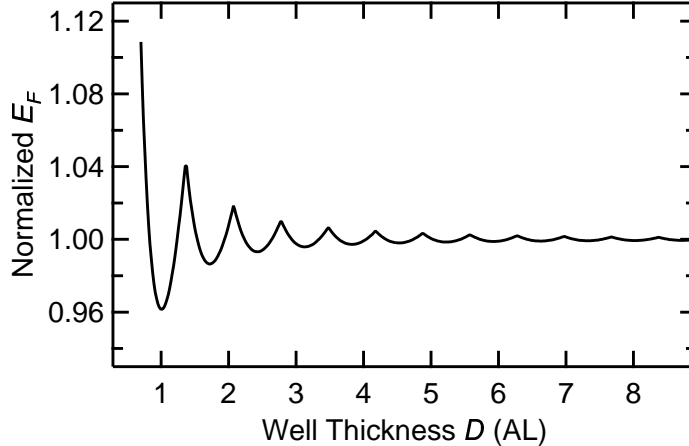
Figure 4.5: The Fermi energy for a Pb(111) film as a function of thickness applying only the condition of charge balance (Constraint #2) inside the film, normalized to the free-electron bulk value.

Solving Eqs. (4.26) and (4.30) simultaneously along with Eq. (4.27), one finds that the charge spillage is proportional to the Fermi energy

$$\Delta = \frac{A_{\text{cell}}t}{4\pi N_{\text{val}}} \frac{m}{\hbar^2} E_F. \qquad (4.31)$$

Using the bulk Fermi level for Pb(111) gives a charge spillage of $\Delta = 0.262t$. The Fermi level for the infinite well model with this charge spillage is shown in Fig. 4.3 as a solid curve, which is within 1% of its bulk value for integer $N \geq 1$. Figure 4.4(b) shows the electronic charge density profile inside the quantum well in this case, where it can be seen that the tails in the density lie partially outside the classical boundaries defined by the positive background, thus reducing the region of electron depletion within the classical boundaries. The result is a surface dipole layer. Note that the issue of charge spillage is automatically accounted for in a model with finite bounding potentials. Such a model is developed in Sec. 4.5.3, which yields results very similar to the present model, as shown in Fig. 4.3 with a dashed curve.

It is also possible to enforce the charge balance condition (Constraint #2) while relaxing the charge neutrality constraint (Constraint #1). In this case, since Eq. (4.30) only explicitly contains the variables D and k_F [as opposed to Eq. (4.26), which also explicitly depends on N], the Fermi level can be found for a given well thickness. Solving Eq. (4.30) for k_F in this case results in the Fermi level shown in Fig. 4.5. Note that here the Fermi level is only dependent on the width of the quantum well, which is distinct from the values shown in Fig. 4.3, which are determined by N, the number of atomic layers in the film. Of course, if the charge neutrality constraint

is relaxed, then the theoretical film can take on a net charge. However, in practice the charge spillage parameter is still used, only it is utilized as an adjustable parameter. As long as it is close to the value given by Eq. (4.31), the discrepancy between total charge of the film and that of the quantum well is small. For a film supported on a substrate and in contact with a reservoir of electrons, this effect is accounted for by the formation of an interface charge layer. For such a system, charge conservation must be considered for the entire system, not for the film alone.

In summary, if only Constraint #1 is enforced, without taking into account the charge spillage of the electron density past the classical boundaries of the film, the Fermi level rises steeply for small film thicknesses, a situation that does not reflect reality. When charge spillage is added to the model and charge balance is approximately achieved, the Fermi level is very close to its bulk value. In this case, Constraint #1 is enforced while Constraint #2 is only approximately obeyed. Alternatively, in some instances it may be more appropriate to enforce the charge balance condition while relaxing the condition of charge neutrality. In this case, Constraint #2 is enforced strictly and the Fermi level is close to the bulk value as shown in Fig. 4.5. Constraint #1 will be approximately satisfied as long as the charge spillage is a reasonable value. In this case, the film takes on a net total charge; however, such an effect is justified if the experimental reality of the substrate is taken into account.

4.4   Lattice Distortions

4.4.1   Overview

In Chapter 5, an analysis of x-ray diffraction data is presented that indicates the presence of significant lattice distortions (strain) in the atomic-layer structure of ultrathin Pb/Si(111) films. These distortions are then correlated with the free-electron charge density oscillations described in Sec. 4.2. In this section, the free-electron models used in the experimental analysis are derived. In principle, the models are valid for any sufficiently free-electron-like metal film; however, the discussion and examples will concentrate on the effects specific to Pb films since they are most applicable to the present work.

To relate the lattice distortions to the charge density variations, there are two models that can be followed. Either one can recognize that any lattice distortions due to variations in the charge density will be propor-

tional to the local gradient of the charge density near each atomic plane, or one can calculate the electrostatic force on each atomic plane due to the charge distribution of the entire system. Within the local gradient approximation, the positively charged atomic cores move toward regions of higher electronic charge, but the charge distribution away from the point of interest is ignored. The two models actually yield very similar functional forms for the electronic forces, which is to be expected. The electrostatic field corresponds to an integral of the charge density, while the local gradient corresponds to a derivative of the charge density. Since the charge density variations within the film are dominated by sinusoidal oscillations (at a wavelength of $\lambda_F/2$), its integral and derivative should be similar. Numerical results to be presented below confirm that the differences (with proper choices of normalization constants) are small and well within the errors of our analysis.

In Sec. 4.3 it was noted that the electronic charge density will tunnel into the classically forbidden regions slightly and accounted for this reality with symmetric charge spillage parameters at the well boundaries. However, for the purpose of describing lattice distortions in the film, the asymmetry in the properties of the two film interfaces is important. Thus, in this section the width of the quantum well is defined to be

$$D = \Delta_s + Nt + \Delta_0 \tag{4.32}$$

where Δ_s and Δ_0 are the charge spillage distances into the substrate and vacuum, respectively. Given this definition, the coordinate positions of each atomic plane in the absence of any lattice distortions would be

$$z_j = \Delta_s + (j - \tfrac{1}{2})t \qquad j = 1, 2, \ldots, N, \tag{4.33}$$

where $j = 1$ corresponds to the atomic layer closest to the substrate. The introduction of independent charge spillage parameters into the model is essentially equivalent to introducing one phase shift function at the surface $z = D - \Delta_0$, and another at the buried interface $z = \Delta_s$. For an infinite barrier, the phase shift has a fixed value of $-\pi$, but by moving the film boundaries by Δ_s and Δ_0, the phase shifts become adjustable and can be made to mimic the actual system [36].

The presence of the substrate is therefore being taken into account explicitly in these models. Thus, the application of Constraint #2 is more appropriate in this case and the Fermi level shown in Fig. 4.5 will be used. Charge is conserved for the film-substrate system but not necessarily for the
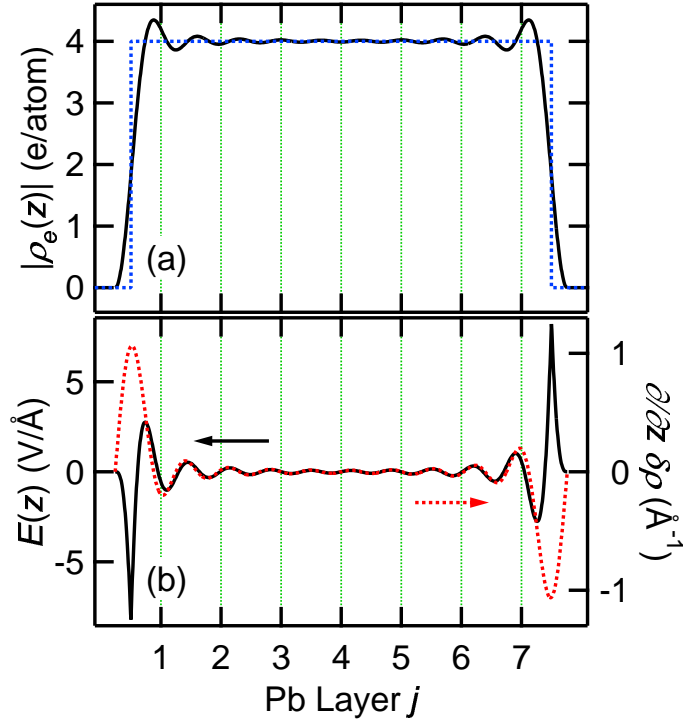
Figure 4.6: (a) The electronic charge density (solid curve) with a positive uniform background (dotted lines) for a Pb(111) film with a nominal thickness of 7 AL. (b) The electric field inside the quantum well (solid curve) compared to the first derivative of the self-normalized charge density variations (dotted curve). Vertical dotted lines indicate the positions of atomic planes in the well where the functions are sampled. The two curves are functionally similar at the atomic planes but differ in the boundary regions.

film alone; thus, the condition of charge neutrality for the film (Constraint #1) is not necessarily strictly obeyed. Since the values for Δ_0 and Δ_s were both found to be close to the value given by Eq. (4.31), the magnitude of the interface charge layer will be small and well within reasonable expectations (a fraction of e per interface atom is typical, depending on the charge transfer [85]).

4.4.2 The Local Charge Density Gradient

In calculating the local gradient of the charge density, any uniform positive background (as in the jellium model) can be ignored since it does not contribute to the derivative of the charge density anywhere except the two discontinuities at the film boundaries. Similarly, the constant portion to the electronic charge density, C_D, does not contribute to the charge density gradient. Thus, for simplicity the self-normalized charge density variations,

Eq. (4.14), are considered. Under the assumption that the displacement of each atomic plane is proportional to the local gradient of the calculated charge density, the change in atomic layer spacing between layers j and $j+1$ is

$$\Delta t_{j,j+1} = K \left[\frac{\partial}{\partial z} \delta\rho(z_{j+1}) - \frac{\partial}{\partial z} \delta\rho(z_j) \right] \tag{4.34}$$

where a linear response coefficient K has been included. Since this quantity involves a local difference, the local gradient approximation is expected to work well. In other words, electrostatic fields derived from charges far away from the two atomic layers of interest should have little effect. This method of calculating the lattice distortions results in a model with four adjustable parameters: K, Δ_s, Δ_0, and t. The last quantity should be close but not necessarily identical to the value found in the bulk material.

An example of the charge density inside the quantum well in this model is shown in Fig. 4.6(a) (solid curve) along with its first derivative in Fig. 4.6(b) (dotted curve with scale on the right axis). Since the displacement of each atomic plane in this model follows the first derivative of the charge density variations, this is the quantity that will determine the form of the lattice distortions. Since it is the derivative of an oscillatory function with a periodicity of $\lambda_F/2$, the lattice distortions will also have this periodicity. For Pb(111), $\lambda_F/2 \approx \frac{2}{3}$ AL and so every two interlayer spacings of the film will correspond to approximately three full oscillations in the derivative of $\delta\rho$. Since the lattice consists of discrete atomic planes, any distortions due to the electronic charge density variations are therefore expected to have an approximately bilayer periodicity.

Note that our numbering convention for the atomic layers differs from that used in many other studies in the literature, where the notation d_{12} is often used to denote the interlayer distance between the two layers closest to the *vacuum*. Hence,

$$d_{12} = \Delta t_{N-1,N} + t$$
$$d_{23} = \Delta t_{N-2,N-1} + t$$
$$\vdots$$
$$d_{N-1,N} = \Delta t_{1,2} + t.$$

4.4.3 The Electrostatic Force

To calculate the electrostatic force, the total charge density is needed, including contributions from the positive atomic cores. In keeping with the

spirit of the free-electron model, a uniform positive (jellium) background is used. The total charge density is then

$$\rho(z) = \rho_e(z) + \frac{N_{\text{val}}\, e}{A_{\text{cell}}\, t}\left[H(z - \Delta_s) - H(z - D + \Delta_0)\right], \tag{4.35}$$

where $H(x)$ is the Heaviside step function

$$H(x) = \begin{cases} 0 & x < 0 \\ 1 & x > 0. \end{cases} \tag{4.36}$$

The electric field is related to the charge density by

$$\frac{\partial}{\partial z} E(z) = \frac{1}{\epsilon_0}\rho(z) \tag{4.37}$$

where E is the z component of the electric field (the only non-zero component by symmetry). Integrating this equation and using Eqs. (4.8) and (4.35) yields

$$
\begin{aligned}
E(z) &= \frac{1}{\epsilon_0}\int_0^z \rho(z')dz' + E(0) \\
&= -\frac{e}{2\pi\epsilon_0 D}\left[C_D z - \sum_{n=1}^{n_0}\left(\frac{Dk_F^2}{2\pi n} - \frac{\pi n}{2D}\right)\sin\left(\frac{2\pi n z}{D}\right)\right] \\
&\quad + \frac{N_{\text{val}}\, e}{A_{\text{cell}}\, t}\left[R(z - \Delta_s) - R(z - D + \Delta_0)\right] + E(0) \tag{4.38}
\end{aligned}
$$

for the electric field, where $R(x)$ is the ramp function

$$R(x) = \begin{cases} 0 & x < 0 \\ x & x > 0. \end{cases} \tag{4.39}$$

The atomic cores each have a net charge of $N_{\text{val}}e$ so the change in the interlayer spacing between layers j and $j + 1$ is

$$\Delta t_{j,j+1} = \frac{N_{\text{val}}\, e}{K'}\left[E(z_{j+1}) - E(z_j)\right] \tag{4.40}$$

where K' is a force constant. Note that the term $E(0)$ in Eq. (4.38) has no effect on the interlayer spacings.

The electric field model for the lattice distortions also has four adjustable parameters, as with that of the last section, with the role of the linear response coefficient K taken by $1/K'$. A comparison of the electric field to the first derivative of the charge density variations is shown in Fig. 4.6(b). As

would be expected, they have a similar functional form over the range where atomic planes are located. The differences can become significant outside the atomic layers due to the tail of charge spillage, but these differences are irrelevant to our analysis of atomic layer strain.

4.5 Surface Energy

4.5.1 Overview

In Chapter 6 a stability analysis is presented of Pb/Si(111) films that have been annealed to a state of quasi-equilibrium. Such experiments provide information on the relative stability of different film thicknesses over a wide range of thicknesses. In this section, two different free-electron models for the surface energy of a metal film are discussed. The first model is based upon an infinite quantum well model like that of the previous sections of the chapter, whereas the second model is based upon a quantum well with finite bounding potentials, the results of which are compared with the infinite well model and are found to be similar.

These models are meant only to illustrate some of the thickness-dependent effects due to confinement of the itinerant electrons in a metal film (QSEs) and are not meant to describe the surface energy in quantitative detail. Hence, only the functional form of the surface energy will be used in the experimental analysis, with adjustable parameters included to account for the specific phenomenology encountered in the actual experiment. For simplicity, only the symmetric case is considered where the charge spillage at each interface is the same; i.e., the calculation is for a free-standing slab. Thus, the Fermi level shown in Fig. 4.3 as a solid curve is used where both constraints are approximately obeyed by using the charge spillage given by Eq. (4.31) for the bulk free-electron Fermi energy. Since this calculation does not take into account the differences in the two film boundaries (i.e., no substrate), it should only be considered correct to within an unknown phase shift with respect to the interface (that will henceforth become an adjustable parameter).

4.5.2 Infinite Well

The point of departure for calculating the surface energy of a metal film is the same as it was in Sec. 4.2; namely, the film is modelled by a free-electron gas confined to a quantum well with infinite potential barriers. In general,

the energy of a free-electron gas is

$$E = \frac{2V}{8\pi^3} \int_{|\mathbf{k}|<k_F} d^3\mathbf{k} \frac{\hbar^2|\mathbf{k}|^2}{2m_e}. \tag{4.41}$$

However, when the gas is confined to a quantum well, the Fermi sphere of allowed states is reduced to a series of subbands, as shown in Fig. 4.1. The total electronic energy of the film then becomes

$$E = \frac{2V}{8\pi^3} \int_{|\mathbf{k}|<k_F} d^3\mathbf{k} \frac{\hbar^2|\mathbf{k}|^2}{2m_e} \sum_{n=1}^{n_0} \frac{2\pi}{D} \delta\left(k_z - \frac{n\pi}{D}\right) \tag{4.42}$$

$$= \frac{A\hbar^2}{4\pi^2 m_e} \sum_{n=1}^{n_0} \int_0^{\sqrt{k_F^2-k_z^2}} 2\pi k_{\parallel} \left(k_{\parallel}^2 + k_z^2\right) dk_{\parallel} \tag{4.43}$$

$$= \frac{A\hbar^2}{8\pi m_e} \sum_{n=1}^{n_0} \left(k_F^4 - k_z^4\right) \tag{4.44}$$

where A is the surface area of one interface of the film such that $V = DA$. In the last two expressions it is implicit that k_z is the discrete index given by Eq. (4.3). Substituting the explicit values for k_z into the formula yields

$$E = \frac{A\hbar^2}{8\pi m_e} \left[n_0 k_F^4 - \left(\frac{\pi}{D}\right)^4 \sum_{n=1}^{n_0} n^4\right] \tag{4.45}$$

$$= \frac{A\hbar^2}{8\pi m_e} \left[n_0 k_F^4 - \left(\frac{\pi}{D}\right)^4 \frac{1}{30} n_0(n_0+1)(2n_0+1)(3n_0^2+3n_0-1)\right]. \tag{4.46}$$

The total energy can be separated into contributions from the bulk and surface [71]

$$E = \varepsilon_b V + 2\varepsilon_s A, \tag{4.47}$$

where ε_b and ε_s are the bulk and surface energy densities, respectively. The factor of two results from the two separate surfaces of our model system slab. The bulk contribution can be found by taking the $D \to \infty$ limit of Eq. (4.46), when boundary effects are negligible,

$$\varepsilon_b = \lim_{D\to\infty} \frac{E}{V} \tag{4.48}$$

$$= \frac{\hbar^2 \left(k_F^{\text{bulk}}\right)^5}{10\pi^2 m} \tag{4.49}$$

$$= \frac{3}{5} \frac{N_e}{V} E_F^{\text{bulk}}, \tag{4.50}$$

where the free-electron results for the electron density $\frac{N_e}{V} = \frac{1}{3\pi^2}\left(k_F^{\text{bulk}}\right)^3$ and the bulk Fermi energy $E_F^{\text{bulk}} = \frac{\hbar^2\left(k_F^{\text{bulk}}\right)^2}{2m_e}$ were used to arrive at the last expression, which may be more familiar to the reader. Note that this same expression can be obtained by integrating Eq. (4.41) without the quantization condition, Eq. (4.3). Using Eqs. (4.46) and (4.47), the surface energy density is then

$$
\varepsilon_s = \frac{\hbar^2}{16\pi m}\left[n_0 k_F^4 - \frac{4}{5\pi}\left(k_F^{\text{bulk}}\right)^5 D \right.
$$
$$
\left. - \left(\frac{\pi}{D}\right)^4\left(\frac{1}{5}n_0^5 + \frac{1}{2}n_0^4 + \frac{1}{3}n_0^3 - \frac{1}{30}n_0\right)\right]. \quad (4.51)
$$

Using the Fermi level as found in Sec. 4.3 (solid curve in Fig. 4.3), the relative surface energy per surface atom, $E_S = A_{\text{cell}}\varepsilon_s$, for a Pb(111) film calculated with Eq. (4.51) is shown in Fig. 4.7(a) as a continuous function of N (solid curve). A constant offset, which is irrelevant in a discussion of the relative stability of different thicknesses, has been subtracted off so that the amplitude of the oscillations is more apparent. The oscillations have a wavelength of $\pi/k_F = \lambda_F/2$. This behavior, which is characteristic of quantum size effect phenomena, can be understood as follows. The number of subbands, or Fermi disks (see Fig. 4.1), that falls below the Fermi level is $n_0 = \text{int}\left(\frac{k_F D}{\pi}\right)$, so every expansion of the well $D \to D + \pi/k_F$ results in an additional subband crossing the Fermi level. This periodic addition of subbands results in oscillations in the surface energy that dampen as the subbands get closer together with increasing film thickness. Since the Fermi level shown in Fig. 4.3 is relatively constant, the oscillations in the surface energy have a regular periodicity of π/k_F.

Since the film must be composed of an integer number of atomic layers, the surface energy of an actual film will only take on the values at integer N, which are shown in Fig. 4.7(b) as open circles. Even-odd alternations in the values are evident with a phase reversal (even-odd crossover) occurring periodically. This effect is due to interaction of the discrete nature of the atomic lattice structure of the film with the oscillations in the surface energy. Half the Fermi wavelength for Pb(111) is very close to $\frac{2}{3}$ an atomic interlayer spacing; thus, every two film layers corresponds to approximately three full oscillations in the surface energy. Since the relationship is not exact, the bilayer alternations will have a beating pattern superimposed over them causing the phase reversal effect. The envelope of this beating function is shown in Fig. 4.7(b) with dashed curves.
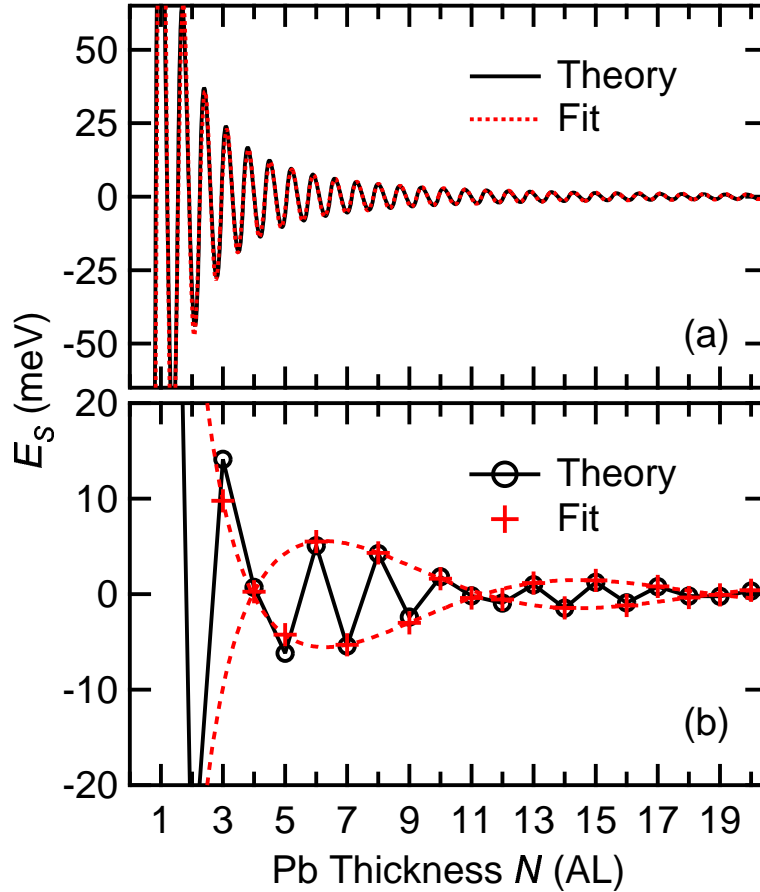
Figure 4.7: (a) The surface energy for a Pb(111) film calculated using a model based on a free-electron gas confined to an infinite quantum well with charge spillage (solid curve). Oscillations are evident that are well-described by a damped sinusoidal form (dotted curve). (b) The same data for thicknesses of an integer number of atomic layers. Bilayer oscillations within an overlying beating pattern (the envelope for which is shown with dashed curves) result from interference of the oscillations shown in (a) and the discrete lattice of the crystalline film.

The relative surface energy is well-described by the phenomenological sinusoidal form

$$E_S = A \frac{\sin(2k_F^{\text{bulk}} N t + \phi)}{N^\alpha} + B \qquad (4.52)$$

where A is an amplitude parameter, ϕ is a phase shift factor that will be dependent on the interface properties of the film, α is a decay exponent, and B is a constant offset, which was subtracted off from E_S to obtain the values in Fig. 4.7. A fit of this function to the surface energy is shown as a dotted curve in Fig. 4.7(a) and as crosses in Fig. 4.7(b). The decay exponent, which is the only parameter value used in the experimental analysis, was found to be $\alpha = 1.77 \pm 0.09$ over the range of N relevant to this work (it can vary
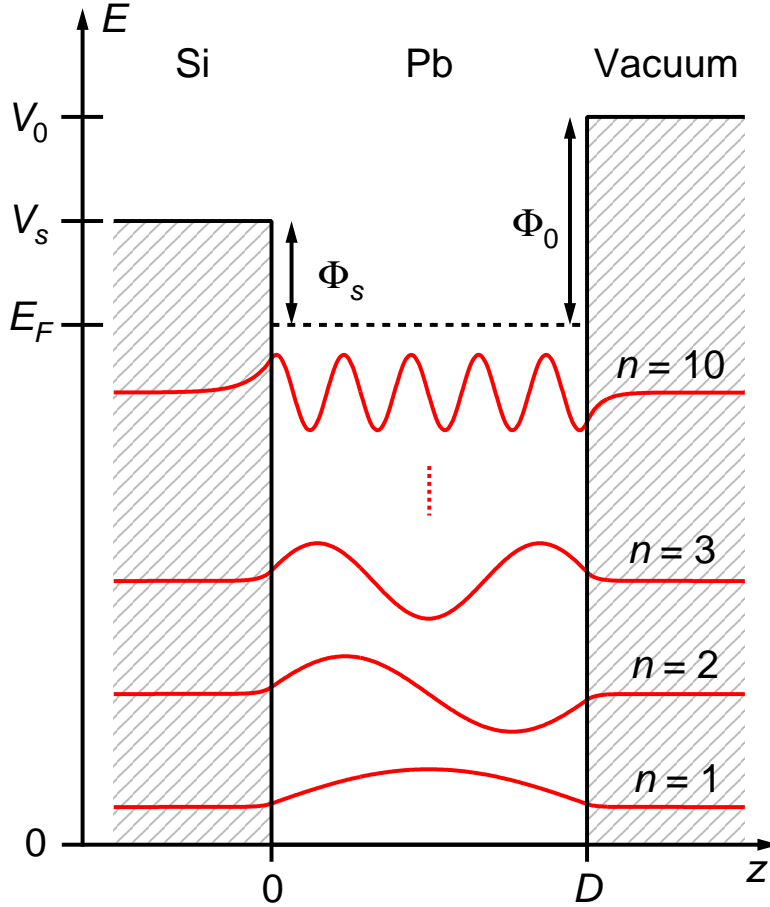
Figure 4.8: A schematic of the finite quantum well used to calculate the surface energy. Two potential barriers confine the quantum well states to the Pb film in the middle of the diagram. The wave functions are shown for $n = 1$, 2, 3, and 10.

slightly for different ranges of N).

4.5.3 Finite Well

An alternative model for the surface energy of a thin metal film can be constructed with finite potential barriers. The quantum well for such a model is shown schematically in Fig. 4.8, where V_s is the confining potential at the buried interface, and V_0 is the vacuum confinement potential. These potentials can be broken up into the components

$$V_s = E_F + \Phi_s$$
$$V_0 = E_F + \Phi_0$$

(4.53)

where Φ_0 is the work function of the film material and Φ_s is an effective potential step encountered by an electron travelling between the film and substrate. In an actual physical system, the electrons in the film material are confined by the band gap of the semiconductor substrate, which does not behave like a simple potential barrier [36]. Thus, a simple step-potential model is not expected to accurately describe the system. Nonetheless, the finite quantum well model provides an alternative to the infinite well and illustrates some of the general strengths and weaknesses of using a free-electron model. In all subsequent calculations, the values $\Phi_0 = 4$ eV, the work function of Pb, and $\Phi_s = 0.6$ eV, the Schottky barrier of the Pb/Si(111) interface [85], will be used.

The z components of the wave functions for the confined states in this model are of the form

$$\psi(z) = \begin{cases} C_1 \exp\left(\kappa_s z\right) & z < 0 \\ C_2 \sin(k_z z) + C_3 \cos(k_z z) & 0 < z < D \\ C_4 \exp\left[-\kappa_0(z - D)\right] & z > D \end{cases} \tag{4.54}$$

where C_1–C_4 are constants subject to normalization and boundary conditions, and κ_s, κ_0, and k_z are all real quantities for confined states. Enforcing energy conservation at the well boundaries (i.e., the three regions of the wave function must have the same energy) leads to the two relations

$$\begin{aligned} \kappa_s &= \sqrt{\frac{2mV_s}{\hbar^2} - k_z^2} \\ \kappa_0 &= \sqrt{\frac{2mV_0}{\hbar^2} - k_z^2}. \end{aligned} \tag{4.55}$$

Requiring continuity of ψ and its first derivative at the boundaries $z = 0$ and $z = D$ results in four more conditions

$$\begin{aligned} C_1 &= C_3 \\ C_1 \kappa_s &= C_2 k_z \\ C_4 &= C_2 \sin(k_z D) + C_3 \cos(k_z D) \\ -C_4 \kappa_0 &= C_2 k_z \cos(k_z D) - C_3 k_z \sin(k_z D), \end{aligned} \tag{4.56}$$

which can be solved algebraically to yield the transcendental equation

$$\tan(k_z D) = \frac{\kappa_s + \kappa_0}{k_z^2 - \kappa_s \kappa_0} k_z. \tag{4.57}$$

Due to the periodic nature of the tangent function on the left side of this

equation, there will be a series of discrete solutions to this equation for k_z (and thus also κ_s and κ_0) corresponding to the discrete subbands or Fermi disks shown in Fig. 4.1. Using the trigonometric identities

$$\arctan\left(\frac{x+y}{1-xy}\right) = \arctan x + \arctan y$$

and

$$\arctan x = \frac{\pi}{2} - \arctan\left(\frac{1}{x}\right),$$

yeilds the result

$$k_z D = n\pi - \arctan\left(\frac{k_z}{\kappa_s}\right) - \arctan\left(\frac{k_z}{\kappa_0}\right), \qquad (4.58)$$

which can be solved numerically for the discrete solutions indexed by the integer n, which is the quantum number of the corresponding subband. Note that in the limit $V_s, V_0 \to \infty$, this equation reduces to Eq. (4.3), the quantization condition for the infinite well. Equation (4.58) is the usual Bohr-Sommerfeld quantization rule, with the two arctangent terms related to the phase shifts at the two boundaries.

Finally, if one wishes to fully solve for the wave function given in Eq. (4.54), the values for the constants C_1–C_4 can be determined by solving the normalization condition

$$\int_{-\infty}^{\infty} |\psi(z)|^2 dz = 1, \qquad (4.59)$$

which yields

$$\frac{C_1{}^2}{2\kappa_s} + \frac{C_4{}^2}{2\kappa_0} + \frac{D}{2}\left(C_2{}^2 + C_3{}^2\right) + \frac{1}{4k_z}\left(C_3{}^2 - C_2{}^2\right)\sin(2k_z D)$$
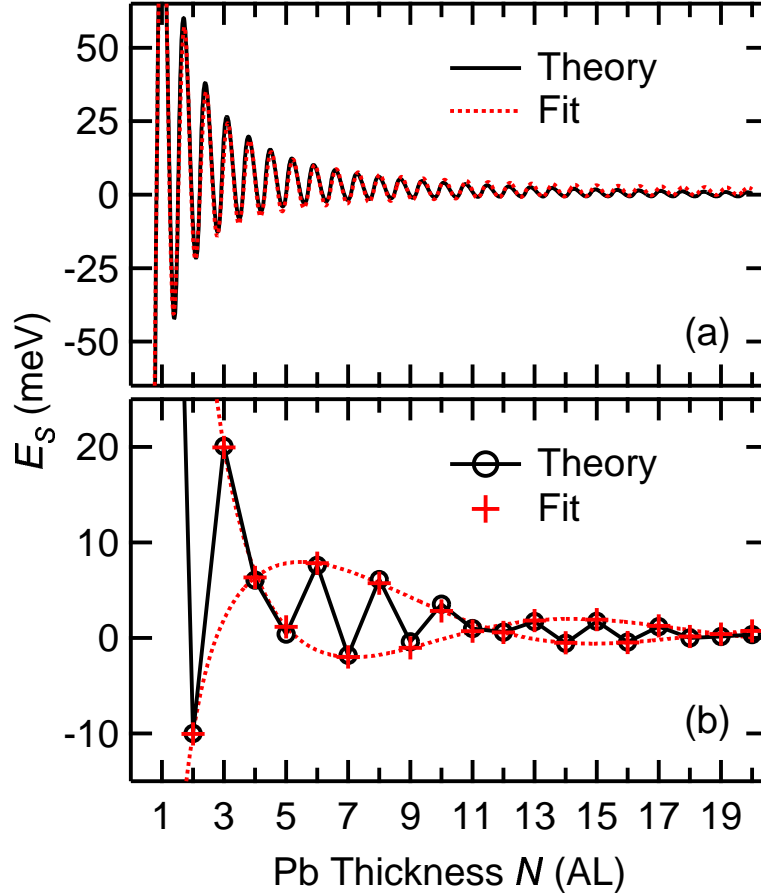$$+ \frac{C_2 C_3}{2k_z}\left[1 - \cos(2k_z D)\right] = 1. \quad (4.60)$$

Sample wave functions are shown in Fig. 4.8 for different subbands.

As in Sec. 4.3, the Fermi level must be appropriately chosen so that the number of electrons in the quantum well,

$$N_e^{\mathrm{QW}} = \frac{A}{2\pi} \sum_{k_z < k_F} \left(k_F^2 - k_z^2\right), \qquad (4.61)$$

remains equal to the number of free electrons given the amount of film

Figure 4.9: (a) The surface energy for a Pb(111) film calculated using a model based on a free-electron gas confined to a finite quantum well (solid curve), along with a fit to a damped sinusoidal function (dotted curve). (b) The same data for integer numbers of atomic layers. Bilayer oscillations similar to those in Fig. 4.7(b) are evident with a slightly different envelope function.

material, Eq. (4.22). The resulting Fermi level for a Pb(111) film is shown in Fig. 4.3 as a dashed curve, which is very similar to that found in the infinite well model with charge spillage. In this case, the Fermi energy remains above the bulk value for all thicknesses, though, with its value about 4% larger than the bulk for $N = 1$ and much closer thereafter.
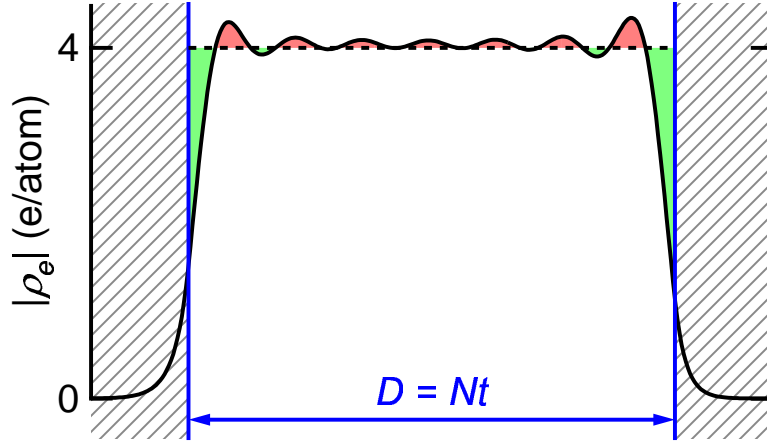
A completely analogous procedure can be used to reach Eq. (4.44) for the total electronic energy of the film and

$$\varepsilon_s = \frac{\hbar^2}{16\pi m} \left[\sum_{k_z < k_F} \left(k_F^4 - k_z^4 \right) - \frac{4}{5\pi} \left(k_F^{\text{bulk}} \right)^5 D \right] \tag{4.62}$$

for the surface energy density. The relative surface energy per surface atom

Figure 4.10: The electronic charge density inside the film calculated with the finite well model. The profile is very similar to that from the infinite well model with charge spillage, Fig. 4.4(b). However, the average density inside the film does not exactly cancel with the positive ionic background, resulting in the upwards bend in the surface energy as $N \to 0$.

is shown in Fig. 4.9(a) with the values for integer N shown in Fig. 4.9(b). It exhibits oscillations similar to those seen with the infinite well in Fig. 4.7. In addition, a slight upwards bend to the surface energy is apparent as $N \to 0$, which is particularly noticeable in the integer N data of Fig. 4.9(b). This effect can be accounted for by adding an additional parameter to Eq. (4.52)

$$E_S = A \frac{\sin(2k_F^{\text{bulk}} Nt + \phi) + C}{N^\alpha} + B. \qquad (4.63)$$

A fit to the surface energy with this equation is shown in Fig. 4.9(a) with a dotted curve and Fig. 4.9(b) with crosses. The decay exponent in this case was found to be $\alpha = 1.74 \pm 0.05$, consistent with the decay exponent of the infinite well model. The amplitude was also found to be similar. Both models exhibit quasibilayer oscillations that decay as $\sim N^{-1.75}$ with thickness, which is the primary result taken from the free-electron calculations. The extra parameter C in Eq. (4.63) was found to be unimportant in our fit to the experimental data and is therefore not used.

An explanation for the upwards bend in the surface energy as the thickness gets smaller can be found by examination of the electronic charge density in the finite quantum well, which can be calculated in the same manner as for the infinite well. The full wave function is this case is

$$\Psi_{\mathbf{k}}(\mathbf{r}) = \frac{1}{\sqrt{A}} e^{ik_x x + ik_y y} \psi_n(z) \qquad (4.64)$$

where $\psi_n(z)$ is the properly normalized wave function for the subband indexed by the quantum number n, defined in Eq. (4.54). The electronic charge density as a function of z is then

$$\rho_e(z) = -\frac{e}{2\pi} \sum_{k_z < k_F} \left(k_F^2 - k_z^2\right) \left|\psi_n(z)\right|^2. \qquad (4.65)$$

A plot of the electron density for $N = 5$ is shown in Fig. 4.10. As one would expect, the electron density spills past the classical boundaries of the film due to the finite potential barriers, similar to the curve in Fig. 4.4(b). However, no condition of charge balance has been imposed analogous to that done for the infinite well model with Eq. (4.30). Since the charge spillage is automatically accounted for in this model, there is no additional parameter such as the Δ used in the infinite well model that can be adjusted to meet such a constraint. As a result, the oscillations in the electron density inside the film do not exactly cancel with the positive background from the ion cores and a net electric field is present in the film. This situation is similar to that in Fig. 4.4(a), but to a much lesser degree. In that case, the charge imbalance in the quantum well resulted in an upwards bend in the Fermi level as $N \to 0$, which translates into a similar effect in the surface energy.

# 5 Lattice Distortions in Pb/Si(111) Films

5.1 Experiment Overview

As mentioned in Chapter 1, Pb/Si films serve as prototypical metal-on-semiconductor systems that have already proved to exhibit strong effects due to QSE. Most previous studies have focused on the interesting "nanomesa" morphology illustrated in Fig. 1.2. For this study, though, a lower growth temperature was used at which it was found that the films follow a layer-by-layer growth mode. Such a growth mode allows examination of thicknesses that are metastable with respect to the overall energy landscape (i.e., not preferred or "magic") as well as stable thicknesses. When the structure of these films is studied in detail, quasibilayer distortions are found in the atomic layer structure of the films consistent with a period of half the Fermi wavelength [83, 86], which is characteristic of QSE phenomena.

For the experiment, Pb films were grown *in situ* using molecular beam epitaxy at a rate of 0.53 Å/min. The sample temperature was maintained at 110 K during deposition and for all subsequent measurements. Time-resolved information on the growth behavior and evolving film morphology was obtained by monitoring the reflectivity of the sample at the out-of-phase condition for Pb(111). In addition, at near-integer coverages, film growth was interrupted and the extended specular x-ray reflectivity rod profile measured to determine the detailed film morphology. The integrated intensity of the reflectivity rod was measured both with the rocking curve and ridge scan methods, which were found to be equivalent for the range of momentum transfer studied (see Sec. 3.6). All of the experimental data presented here were obtained via the ridge scan method since they represent the more comprehensive set.

5.2 Growth Behavior

During deposition, the growth of the Pb overlayers was monitored by measuring the reflected x-ray intensity at $l = 1.65$, where l is the perpendicular momentum transfer in Si(111) reciprocal lattice units as defined in
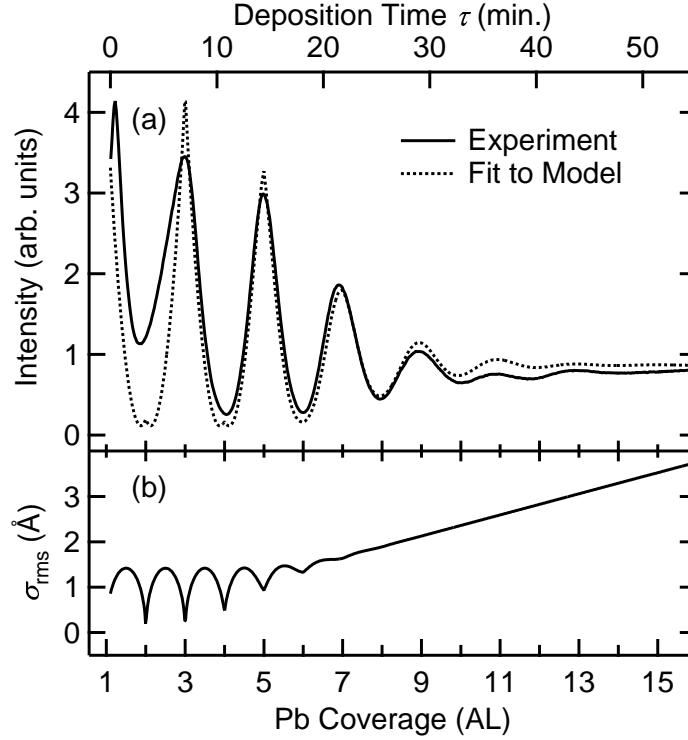
Figure 5.1: (a) Experimentally observed oscillations in the reflected x-ray intensity at the out-of-phase point for Pb(111), $l = 1.65$, and a fit using the model described in the text. The oscillations every two atomic layers indicate that the growth is layer-by-layer whereas the decay of the oscillations is an indication of increasing roughness, which is shown in (b).

Eq. (2.32). This point in reciprocal space, halfway between the origin and the Pb(111) Bragg condition, is the lowest-order out-of-phase condition for the Pb overlayers and as such is highly sensitive to changes in the surface structure. The initial portion of such a growth curve is shown in Fig. 5.1. The regular oscillations in the intensity are indicative of layer-by-layer growth [48,49,70], which in this case is independently supported by photoemission measurements [81]. The decay of the oscillations is a result of increasing surface roughness in the film. Quantitative information can be extracted from these data using the model of Sec. 2.6 for the reflected intensity with a number of simplifying assumptions. First, since only one point in reciprocal space is measured, the influence of lattice distortions on the data will be minimal and it may be assumed that the atomic positions of the Pb atoms are bulklike. Second, to reduce the number of parameters,

it is assumed that the distribution of thicknesses, $\{p_N\}$, is Gaussian:

$$p_N(\tau) = \frac{B(\tau)}{w(\tau)} \exp\left\{ -\frac{\left[N - \Theta(\tau)\right]^2}{w(\tau)^2} \right\} \tag{5.1}$$

where w and Θ are the width of the distribution and the total film coverage (in AL), respectively, B is a normalization factor selected such that Eq. (2.42) is satisfied, and τ is the deposition time. Third, it is assumed that both w and Θ are linear functions of τ. Note that the parameter w is only obliquely related to the rms roughness, which is defined as

$$\sigma_{\mathrm{rms}}(\tau) = t\sqrt{\sum_N p_N(\tau)\left[N - \Theta(\tau)\right]^2}. \tag{5.2}$$

The results of a fit to this model are shown in Fig. 5.1(a) as a dotted curve, with the corresponding roughness shown in Fig. 5.1(b). Considering the simplicity of the model and the number of assumptions it entails, the fit describes the data quite well after about 3 AL. Monitoring of an in-plane superstructure peak from the $(\sqrt{3} \times \sqrt{3})R30°$ interface reconstruction shows it decaying rapidly during the initial phase of deposition. Thus, the behavior of the data for $\Theta < 3$ AL is probably affected by the transition of the initially compressed 1.1 monolayer interface layer of the $(\sqrt{3} \times \sqrt{3})R30°$ reconstruction to one of bulklike density. This interpretation is consistent with previous studies that have shown that the reconstruction is removed upon burial [48, 49, 80].

Using this method, one can determine the initial coverage, the rate of deposition, and the roughness of the film as a function of time while the film is being grown. With this information, a film of a specific thickness can be obtained by interrupting the deposition at the desired coverage. High quality films with precise coverages up to 29 AL have been grown using this method. As an additional check, independent measurements of the deposition rate with a quartz crystal thickness monitor agree with the rates deduced from the fits to the growth curves to within 5%.

A layer-by-layer growth mode with small roughness is important for a study of the thickness-dependence of a film's structure. In the case of Pb, this can be problematic due to quasibilayer oscillations in the surface energy as shown in Fig. 1.3, which is the underlying cause of the "preferred thickness" effect that has been previously reported [21–28, 44, 45]. In fact, even at 110 K, the temperature for this study at which the growth is layer-by-layer, some indication of variations in the film stability are evident when the
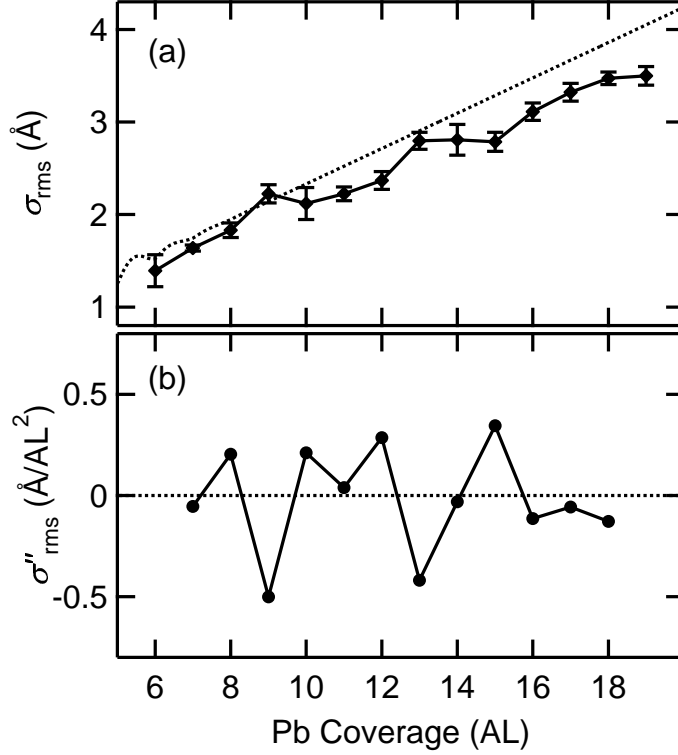
Figure 5.2: (a) The deduced roughness of a single film (solid curve) where deposition was interrupted at integer coverages and the extended x-ray reflectivity measured. Error bars are indicative of the range of values obtained using different fitting methods. The dotted curve is the roughness predicted by a fit to the growth curve of the film as in Fig. 5.1. (b) The discrete second derivative of the data in (a), which shows approximately quasibilayer oscillations in the relative film stability, consistent with oscillations in the surface energy found empirically in Chapter 6 (see Fig. 6.8).

film roughness is examined in detail. Figure 5.2(a) shows the roughness of a film whose growth was interrupted at integer coverages and the extended x-ray reflectivity measured. From fits to the reflectivity, the p_N parameters are determined and a value of the roughness is calculated with Eq. (5.2). The trend of the roughness values follows closely that predicted from the fit to the deposition curve (dotted curve); however, they do not increase smoothly or even monotonically, with noticeable deviations from the overall trend. This effect is indicative of differences in the relative stability of different film thicknesses. For layer-by-layer growth, the distribution of p_N values is peaked about the thickness closest to the coverage, as in Eq. (5.1), but if that thickness is relatively unstable compared to neighboring thicknesses, the system will tend to be rougher, with the p_N distribution broader than it would be due to normal stochastic effects. Thus, the discrete second

derivative of the roughness, σ''_{rms}, is an approximate indicator of the relative stability of the film as a function of thickness. Thicknesses with $\sigma''_{\mathrm{rms}} > 0$ are relatively stable whereas thicknesses with $\sigma''_{\mathrm{rms}} < 0$ are only metastable. These data are shown in Fig. 5.2(b), and indicate that Pb/Si(111) films of thicknesses $N = 8$, 10, 12 and 15 AL are relatively stable and $N = 9$, 13, 16, and 18 are only metastable, with σ''_{rms} too close to zero for the other thicknesses to make a prediction. These results are consistent with observations of films grown or annealed at higher temperatures [21–23, 25, 26], and correspond well with the empirical form of the surface energy found in Chapter 6. It can be therefore concluded that Pb grown on Si(111) at 110 K follows a metastable layer-by-layer growth mode.

5.3 Quasibilayer Lattice Distortions

Films of integer coverages were grown using the process described above for $\Theta = 6 - 19$ AL. The extended x-ray reflectivity was then measured for each coverage and fit using the formulas of Sec. 2.6. Since the films were not annealed, the surface was assumed to be of relatively uniform thickness over large lateral distances and no partial coherence factor was included [i.e., Eq. (2.44) was used]. The full set of extended x-ray reflectivity data is shown in Fig. 5.3, with selected coverages shown in more detail in Fig. 5.4. The reflectivity profiles show some unusual features due to the distorted layer structure of the Pb overlayers. Approximately halfway between the Pb(111), (222) and (333) Bragg peaks at $l \approx 3.3$, 6.6 and 9.9 (the last one not shown), respectively, one of the interference fringes is consistently larger than its neighbors (marked with inverted triangles). Since they appear near the half-order position for Pb(111), these features are indicative of a bilayer or quasibilayer superperiodicity in the structure of the film. This effect is similar to the superstructure peaks often encountered with surface reconstructions (see Sec. 2.4), except in this case the "reconstruction" is in the direction normal to the surface. Since these half-order peaks are much weaker in magnitude than the Pb Bragg peaks, the bilayer distortions are weak and possibly only present in regions near the surface and buried film interface. As can be seen from the dashed curves in Fig. 5.4, these features cannot be reproduced by a model that does not include lattice distortions in the film layer structure.

The origin of the quasibilayer distortions can be attributed to the variations in the charge density discussed in Sec. 4.2. Such variations are damped oscillations with a characteristic wavelength of $\lambda_F/2$. For bulk Pb(111),
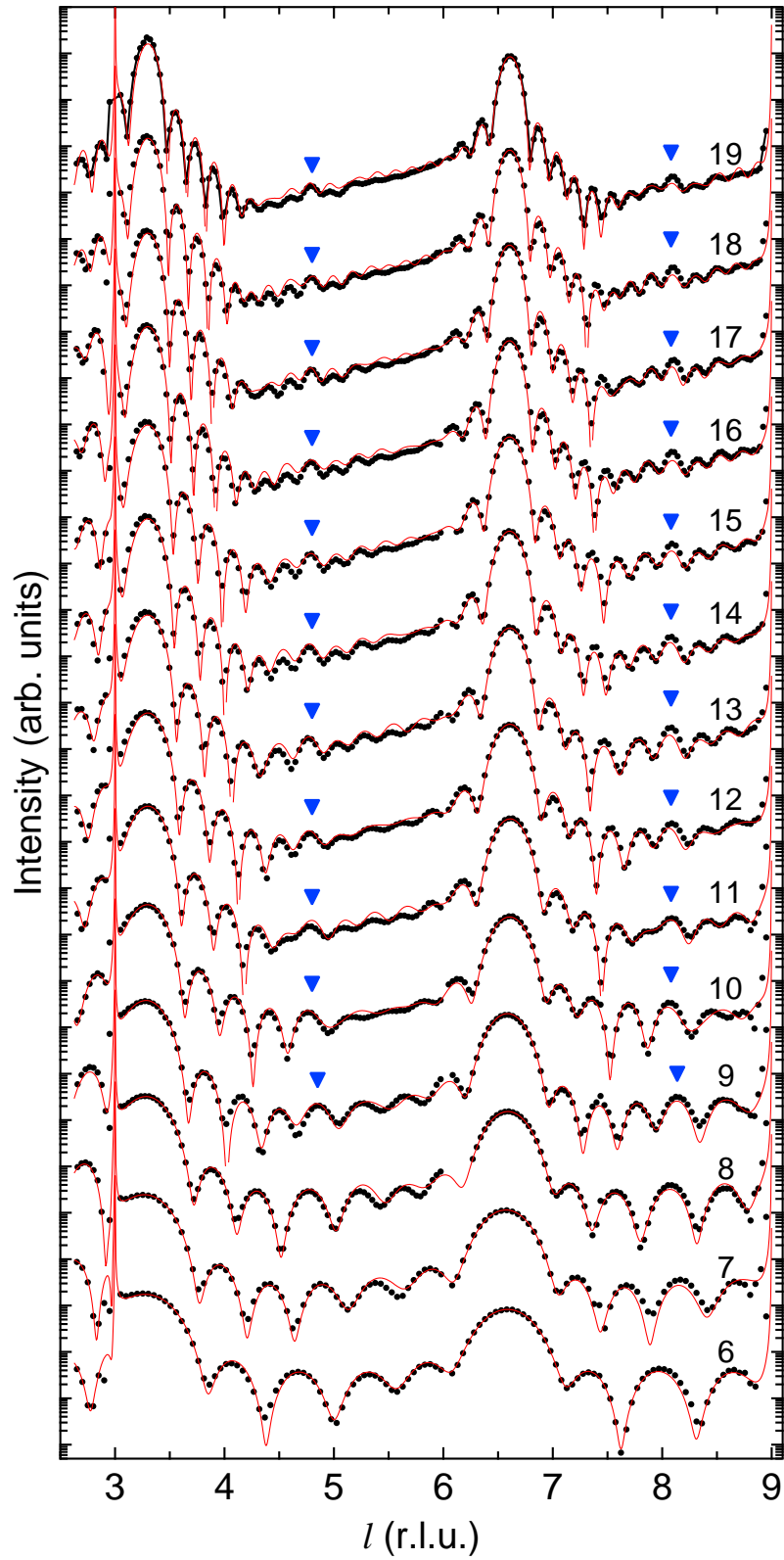
Figure 5.3: The full extended x-ray reflectivity data set.
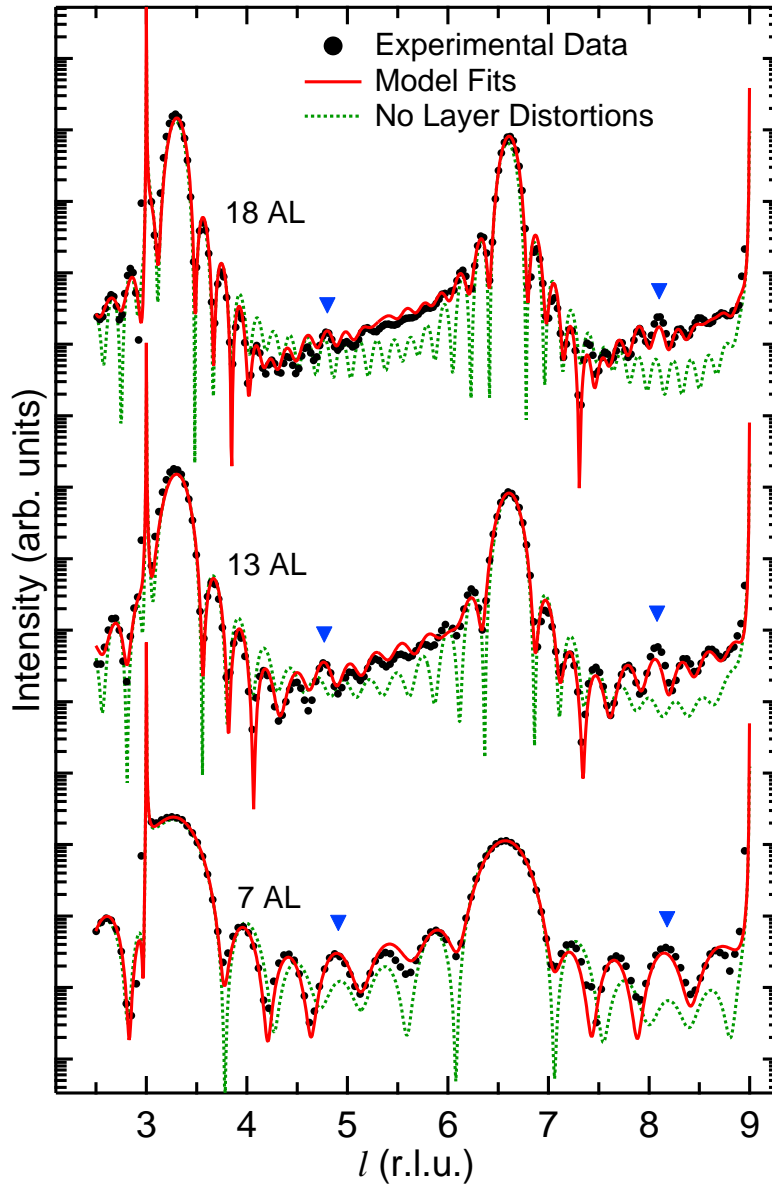
Figure 5.4: Extended x-ray reflectivity data (points) for selected coverages. The sharp peaks at $l = 3$ and 9 are the Si(111) and (333) Bragg peaks, respectively, while the interference fringes in-between are due to the Pb overlayers. The areas marked by inverted triangles are half-order features indicative of a quasibilayer periodicity to the lattice structure of the Pb film. Solid curves are fits using Method B described in the text. Dotted curves are fits with uniform interlayer spacing in the film, which do not represent the data well, especially near the half-order features.
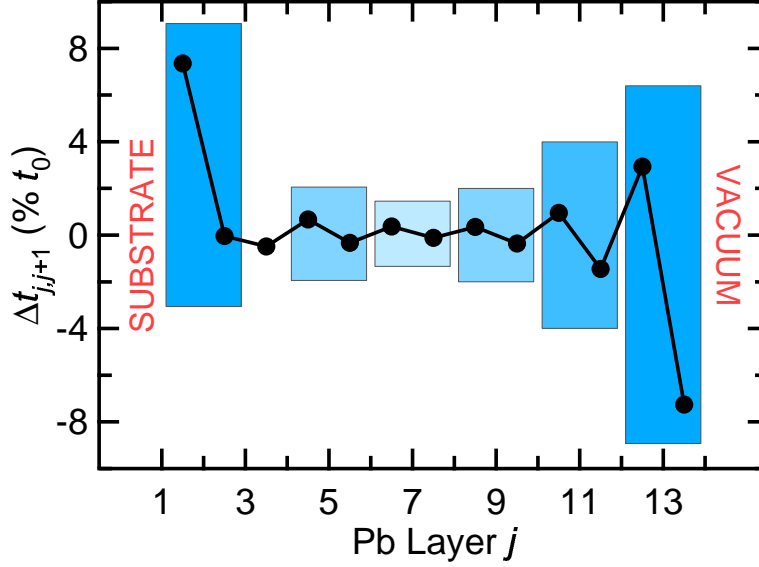
Figure 5.5: The internal lattice distortions for $N = 14$, calculated using Eq. (4.40) with the parameters from a fit to the extended x-ray reflectivity. Alternations in the distortions are evident, which leads to a quasibilayer superperiod in the lattice structure, as shown with shaded boxes. This effect manifests itself as a weak half-order superstructure peak in the x-ray profiles, as seen in Figs. 5.3 and 5.4.

this wavelength is 1.98 Å, which is close to $\frac{2}{3}$ the bulk interlayer spacing $t_0 = 2.84$ Å. Thus, every 2 AL of Pb roughly corresponds to an integral number of oscillations in the charge density. Since the relationship is not exact, the superperiodicity is quasibilayer, and the phase of even-odd oscillations can reverse over a sufficiently wide range of thicknesses.

Oscillations are evident in the lattice distortions resulting from the fits to the x-ray reflectivity, an example of which is shown in Fig. 5.5 for $N = 14$. Most of the lattice relaxation occurs in the atomic layers closest to the two film boundaries, but the quasibilayer distortions penetrate deep into the film as well. An instance of phase reversal (even-odd crossover) is also evident. The overall behavior reflects the force variations as shown in Fig. 4.6(b). The asymmetry of the values in Fig. 5.5 is due to different values for the two charge spillages Δ_s and Δ_0. The results for other thicknesses are qualitatively similar. The thickness dependence of these lattice distortions or relaxations is shown in Fig. 5.6, where the different sets of data points correspond to four different methods that were used to fit the x-ray data. In all cases, the film structure factor was calculated using Eq. (2.40) with the intensity given by Eq. (2.44).
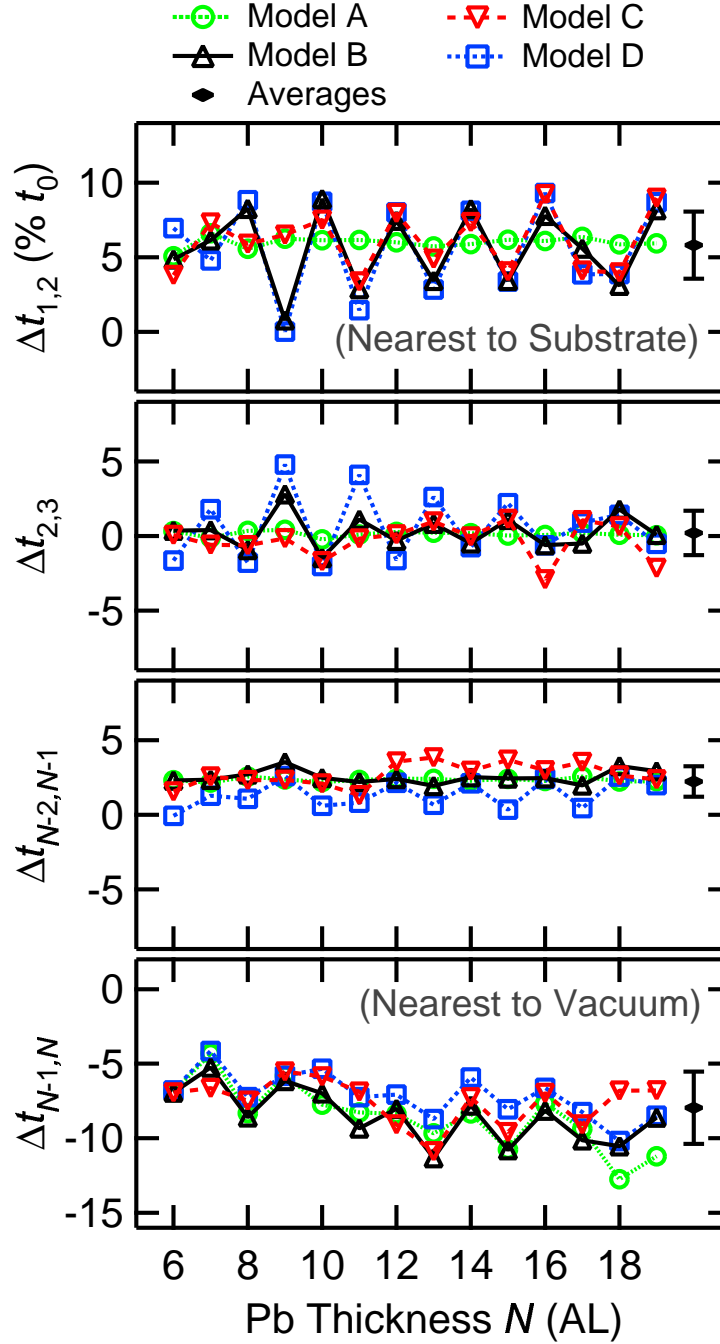
Figure 5.6: The lattice relaxations for the outer atomic layers for each thickness N, where all values are in $\%\ t_0$. The different sets of data points correspond to different fitting methods described in the text. The values for Method A are the values calculated using the parameters for the data set with coverage $\Theta = N$ AL. The points on the far right of each graph represent the values averaged over N for all four methods, along with error bars deduced from the spread in the results.

Method A

The data for each coverage were fit separately with the lattice distortions described by Eq. (4.34), the local charge gradient model. To reduce the number of independent variables, parameters for the lattice distortion model were assumed to be independent of N for any particular coverage, but were allowed to be different for different coverages. This assumption is valid for perfectly smooth films, but can be inaccurate for rough films. Since these parameters do depend on thickness and the film roughness is not necessarily negligible, the Debye-Waller parameter in Eq. (2.40) was replaced with ζ_j factors, as in Eq. (2.39), but only for the Pb layers close to the film boundaries. As a result, this method will be less reliable for extracting the thickness dependence of the lattice distortions, especially for higher coverages since they have the greatest degree of roughness. The results for the two outermost Pb atomic layers at each film interface are shown in Fig. 5.6 as open circles, where the values for any particular thickness N are taken from the data set whose coverage is N AL (with a distribution of p_N values peaked at that thickness).

Method B

The data for all 14 coverages were fit simultaneously using Eq. (4.34) for the lattice distortions. With this method, the parameters for the lattice distortion model were N-dependent and shared amongst all of the data sets. The other parameters needed to fit the data — the p_N values, Debye-Waller factor, etc. — were separate for each coverage. The results for the lattice relaxations of the outermost layers are shown in Fig. 5.6 as open upright triangles. Compared to Method A, this method involved fewer fitting parameters since no ζ_j factors were needed. Since the parameters of the lattice distortion model were N-dependent, this method is more likely to extract the thickness dependence of the interlayer relaxations.

Method C

As with Method B, all of the data sets for different coverages were fit simultaneously, but with the lattice distortions calculated using the electrostatic force model, Eq. (4.40). The same number of parameters were used in the fits as with Method B. The results from this method are shown with open inverted triangles in Fig. 5.6.

Method D

No model was used for the lattice distortions. Instead it was assumed that any relaxations of the lattice would be limited to the atomic layers closest to the interfaces. The two interlayer spacings closest to the substrate and the vacuum (four total) were fit as free parameters and were allowed to vary for different N. To keep the number of parameters reasonable, all 14 data sets for different coverages were fit simultaneously as with Methods B and C, sharing the layer expansion parameters. The interlayer spacings for the other Pb layers were assumed to be equal to a separate parameter, t, which introduces one additional parameter per data set to the fit compared to Methods B and C. The results from this fit are shown as open squares in Fig. 5.6.

5.4   Discussion and Comparison with Other Studies

All four methods of analysis can be justified on physical grounds as reasonable models to describe the essential features of the system. They involve different constraints on some aspects of the system and, in some cases, very different numbers of fitting parameters, yet they all resulted in fits of comparable quality (measured by χ^2). This is a strong indication that the models reflect the physical system. The spread in the results is an indication of the standard error or level of confidence in the results. The black diamonds and error bars at the right side of the panels in Fig. 5.6 show that, averaged over the thickness range of study, the top layer spacing of the Pb film is contracted by $8.0 \pm 2.4\%$ relative to the bulk, while the next layer spacing is expanded by $2.2 \pm 1.0\%$. These values are substantially larger than those reported for bulk Pb(111) [87], but are closer to those resulting from recent first-principles calculations [88]. The layer spacing closest to the Si substrate is expanded by $5.8 \pm 2.2\%$, and the next layer spacing is essentially bulk-like to within $\pm 1.5\%$. In addition to these general trends that are related to Friedel oscillations associated with the film boundaries, the layer relaxations exhibit quasibilayer oscillations as a function of film thickness that can be attributed to confinement and interference effects.

Results of the fits are shown as solid curves in Figs. 5.3 and 5.4. The fits reproduce the aforementioned half-order features very well, especially compared to the example fits with no lattice distortions, shown as dotted curves in Fig. 5.4. That being said, it was found that other solutions ex-

isted with χ^2 values only slightly larger than the best fits. Such solutions primarily differed in the lattice relaxations for $\Delta t_{1,2}$ and $\Delta t_{2,3}$, the two interlayer spacings closest to the substrate. All solutions exhibited strong quasibilayer oscillations as a function of thickness; however, they differed in where the crossover from even to odd occurs — i.e., the phase of the oscillations is weakly determined. For example, the turning point that is evident at around $N \approx 17$ in the data for $\Delta t_{1,2}$ in Fig. 5.6 was found at $N \approx 13$ and $N \approx 11$ in two other solutions with comparable χ^2 values as the best fit. All solutions exhibited similar relaxation values for $\Delta t_{N-1,N}$ and $\Delta t_{N-2,N-1}$, the relaxations of the layers closest to the vacuum. The greater uncertainty in the lattice distortions near the substrate may be due to interfacial roughness from the underlying Si(111) substrate, whose step heights will be incommensurate with the interlayer spacing of the Pb overlayers. However, these errors are no larger than the spread of values determined based on the four different methods of analysis.

In this study, the penetration depth of the x rays used greatly exceeded the thicknesses of all the films studied, so the interference patterns in the data are due to scattering from all the film overlayers. However, a technique such as STM or HAS, with a short probing depth, will primarily measure the step heights on the surface of the film (see for example Fig. 1.1). To compare with the results of such studies, Fig. 5.7 shows the deviation of the net film thicknesses from their ideal bulk values and the deduced step heights as functions of N. Each thickness deviation value is the sum of all the lattice distortions (i.e., the $\Delta t_{j,j+1}$ values) for any given N and the step height values are defined as the difference between two net thicknesses differing by 1 AL. The error bars indicate the spread in values from the different fitting methods. These values show clear quasibilayer oscillations, particularly for the smaller thicknesses. For larger thicknesses, the error bars get progressively wider, commensurate with the increase in film roughness as shown in Figs. 5.1 and 5.2.

It should be noted that the term "step height" as used here refers to the vertical distances between the terrace heights of two thicknesses differing by 1 AL. The local step height encountered by an atom diffusing across the surface of the sample may be different, since additional lattice distortions in the regions very near to the step edges probably occur to minimize the local strain and shear energies. That is, the diagram in Fig. 2.10 is not indicative of the local region around a step edge, but rather a schematic showing how the atomic layers in the (terraces of) different regions of thickness may be misaligned. Furthermore, lateral Friedel oscillations originating from the
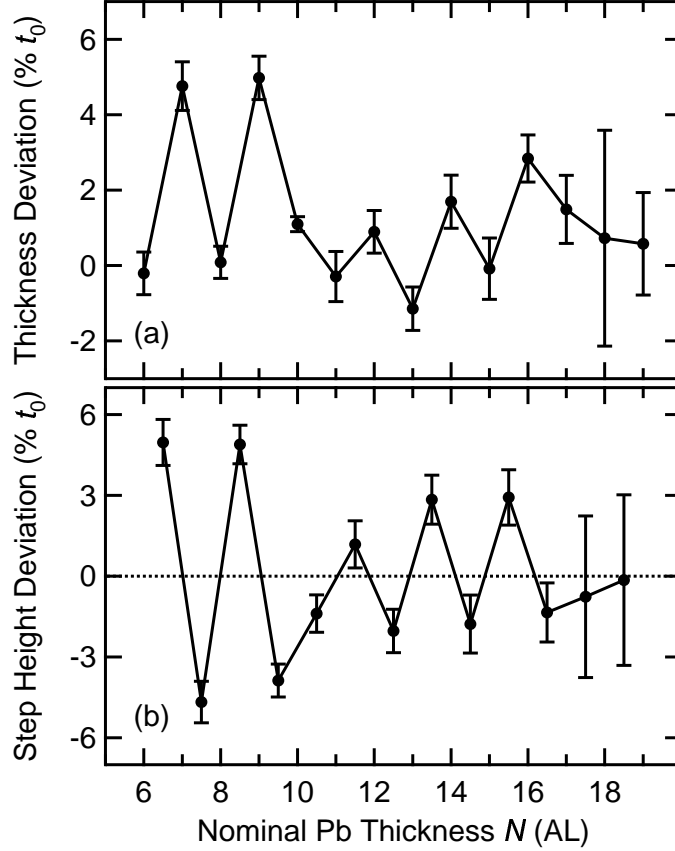
Figure 5.7: (a) The net thicknesses calculated from the lattice distortions. Values are the deviation from the ideal thickness, Nt_0, in % t_0. Error bars are representative of the spread in values from the different fitting methods described in the text. (b) The deduced step heights at the surface, defined as the difference between every two adjacent points in (a).

step edges have been observed in the electron density [89, 90], which can also affect the lattice structure. However, such edge effects will be limited to a relatively local region (within a few lattice spacings) near the step edges. Since HAS is a scattering technique, it measures the statistical average of the scattering from the atomic planes, and STM studies generally measure the heights of atomic terraces over an extended range. Thus, edge effects can be neglected in such comparisons.

The oscillations in Fig. 5.7(b) are consistent with the STM results shown in Fig. 1.1, where it should be noted that the N values differ from those presented here by 1 AL since we have included the wetting layer in N. However, the amplitude of the oscillations in Fig. 5.7 is much smaller than that in Fig. 1.1(b), which may be partly attributable to the fact that STM measures the electron density at the surface, which may not reflect the true

positions of the atomic cores. Similarly, our results are also consistent with those found in the HAS study of Ref. 18.

5.5   Summary

This chapter presented surface x-ray diffraction results of the growth and layer structure (strain) of Pb/Si(111) films with thicknesses of 6–19 AL. At 110 K the system is found to follow a metastable layer-by-layer growth mode with increasing roughness. The extended x-ray reflectivity profiles were found to have distinctive half-order features present that are indicative of a quasibilayer periodicity to the lattice structure. To describe the lattice distortions in the context of QSE, the free-electron models developed in Chapter 4 are used that take into account the formation of quantum well states in the film and describe the Friedel-like oscillations in the electronic charge density of the film. The free-electron models are found to explain the quasibilayer lattice distortions of the film and enable a detailed fit of the experimental data.

Extended x-ray reflectivity profiles at integer coverages were obtained and analyzed to reveal the thickness dependence of the structural properties of the film. Quasibilayer oscillations are also observed in the outermost lattice relaxations as a function of thickness, similar to oscillations seen in other physical properties of the films due to QSE. Finally, the deviations from the ideal film thicknesses are deduced and compared with previous STM and HAS studies, where the present results are found to qualitatively agree, albeit with a smaller amplitude of oscillation. It can be concluded that quantum confinement has important effects on the physical structure of a nanoscale film.

6 Surface Energy of Pb/Si(111) Films

6.1 Experiment Overview

The relative stability of thin metal films has been shown to exhibit strong variations as a function of thickness that have been attributed to electronic contributions to the surface energy [26, 41, 44]. In addition, for certain temperature ranges, some systems exhibit a peculiar film morphology where steep-sided, flat-topped islands of uniform height form on the surface (Fig. 1.2). Using x-ray diffraction and scanning tunneling spectroscopy, the formation of these "nanomesas" has been correlated with the electronic structure of the films [15, 19, 20, 22–26]. This chapter presents a study of the morphological evolution of Pb films as a function of temperature. This evolution is explained in terms of QSE in the surface energy of the films, for which quantitative empirical information is obtained [84, 91].

The experiment is a study of the structural evolution of smooth Pb films grown on Si(111) at 110 K as they are annealed to a state of local equilibrium near room temperature. By frequently interrupting the annealing process and examining the film morphology, the system is effectively observed exploring the local energy landscape as it evolves. Detailed discussions are presented for two different samples, one with an initial thickness that corresponds to a relatively stable configuration (low surface energy), and one with an initial thickness that is relatively unstable (high surface energy). The structural evolution and thermal stability of the two films differ markedly; however, analysis of their final quasi-equilibrium states produces the same form for the surface energy, as expected. The annealing behavior of the films also reveals an additional effect; namely, after the initially smooth film breaks up, further annealing results in the formation of increasingly taller islands. This effect is also attributed to quantum electronic effects. First principles calculations show that the most energetically favored configuration of the system consists of a single layer wetting the substrate (see Fig. 1.3); due to the initial volume of deposited film material, to conserve mass the film morphology thus phase separates into surface regions covered only by a wetting layer, which has the lowest surface energy, and regions

with islands of preferred heights. As the annealing temperature increases, the system has more thermal energy with which to rearrange the atoms on the surface, resulting in the formation of taller islands and a corresponding increase in the area covered by the wetting layer.

As in the experiment of Chapter 5, Pb films were grown *in situ* at 110 K using molecular beam epitaxy at a rate of 0.84 Å/min. At this temperature the system follows a metastable layer-by-layer growth mode that allows for monitoring of the coverage of the films during deposition by collecting the reflected x-ray intensity at the lowest-order out-of-phase condition for Pb(111), which exhibits layer-by-layer oscillations as described in Sec. 5.2. This technique allows for smooth films of precise coverage to be grown. After deposition, the films were slowly annealed to progressively higher temperatures in increments of approximately 5–10 K. After reaching each desired annealing temperature, the sample was quenched back to 110 K for measurement of the specular extended x-ray reflectivity, which was obtained using the ridge scan method described in Sec. 3.6.
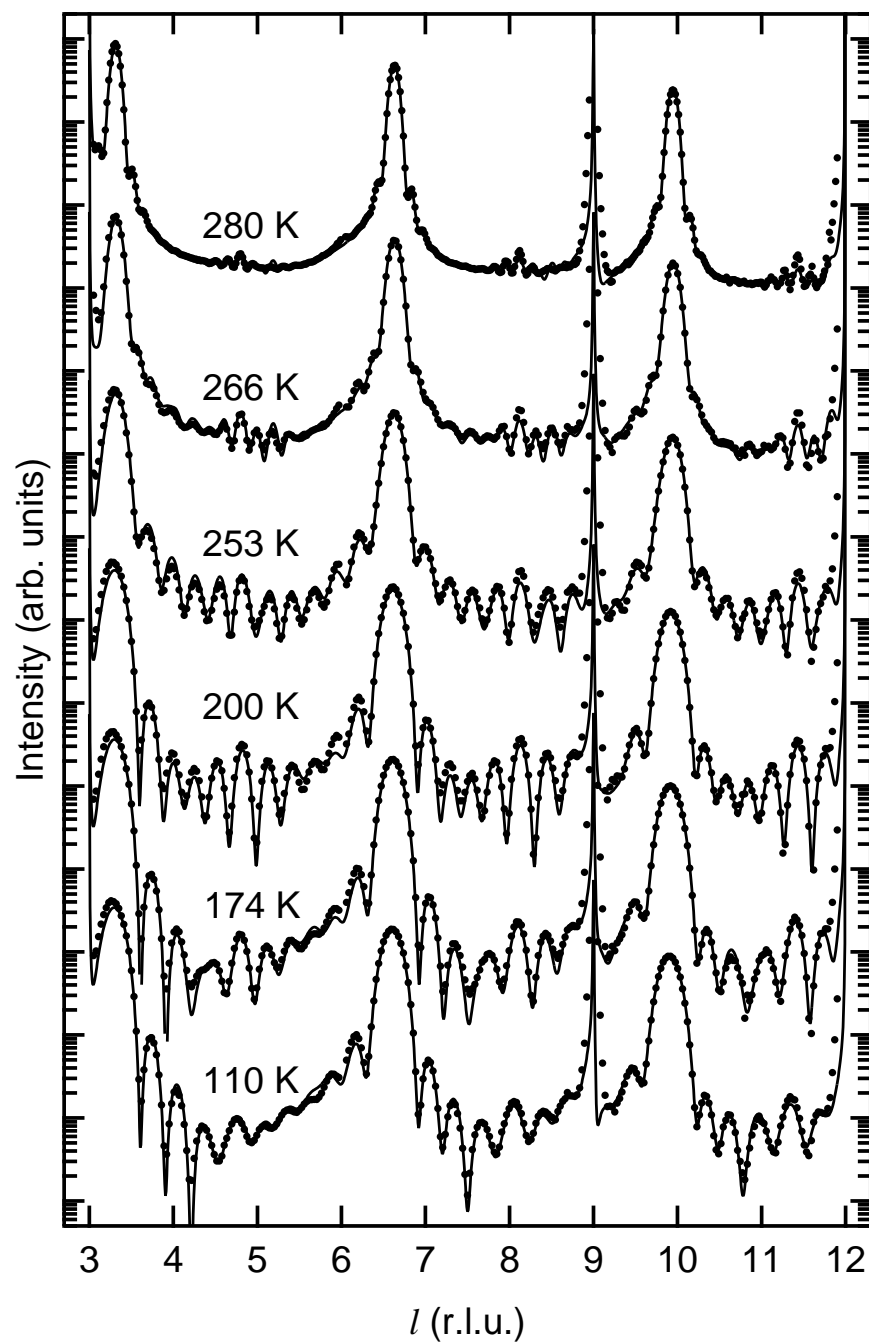
6.2 Extended X-Ray Reflectivity Analysis

Figures 6.1 and 6.2 show extended x-ray reflectivity data (points) for two samples with initial coverages of 6 AL and 11 AL, respectively. The reflectivity profiles measured after annealing to the temperatures indicated are shown in progressive order starting from the base temperature at the bottom. Although data was collected every 5–10 K, only select temperatures are shown to illustrate the major morphological changes. The sharp peaks at $l = 3$, 9, and 12 are the Si(111), (333), and (444) Bragg peaks, respectively, and the interference fringes in-between are due to the Pb overlayers. The broader peaks at $l \approx 3.3$, 6.6, and 9.9 are the Pb(111), (222), and (333) Bragg peaks, respectively. The number and spacing of the fringes between these peaks are an indication of the center of the thickness distribution of the film and its roughness. The reflectivity profiles for smooth films exhibit well-defined fringes with deep minima, similar to the N-slit interference function shown in Fig. 2.9. In such a profile, the number of fringes is equal to the number of atomic layers in the film minus two. For example, the four well-defined fringes evident between the Pb Bragg peaks in the 110 K data in Fig. 6.1 are indicative of a smooth film with a thickness of 6 AL. Thus, the appearance of additional fringes at intermediate temperatures indicates that Pb islands with larger thicknesses form on the surface. Detailed analysis of the data indicates that the average island height tends to get larger. That
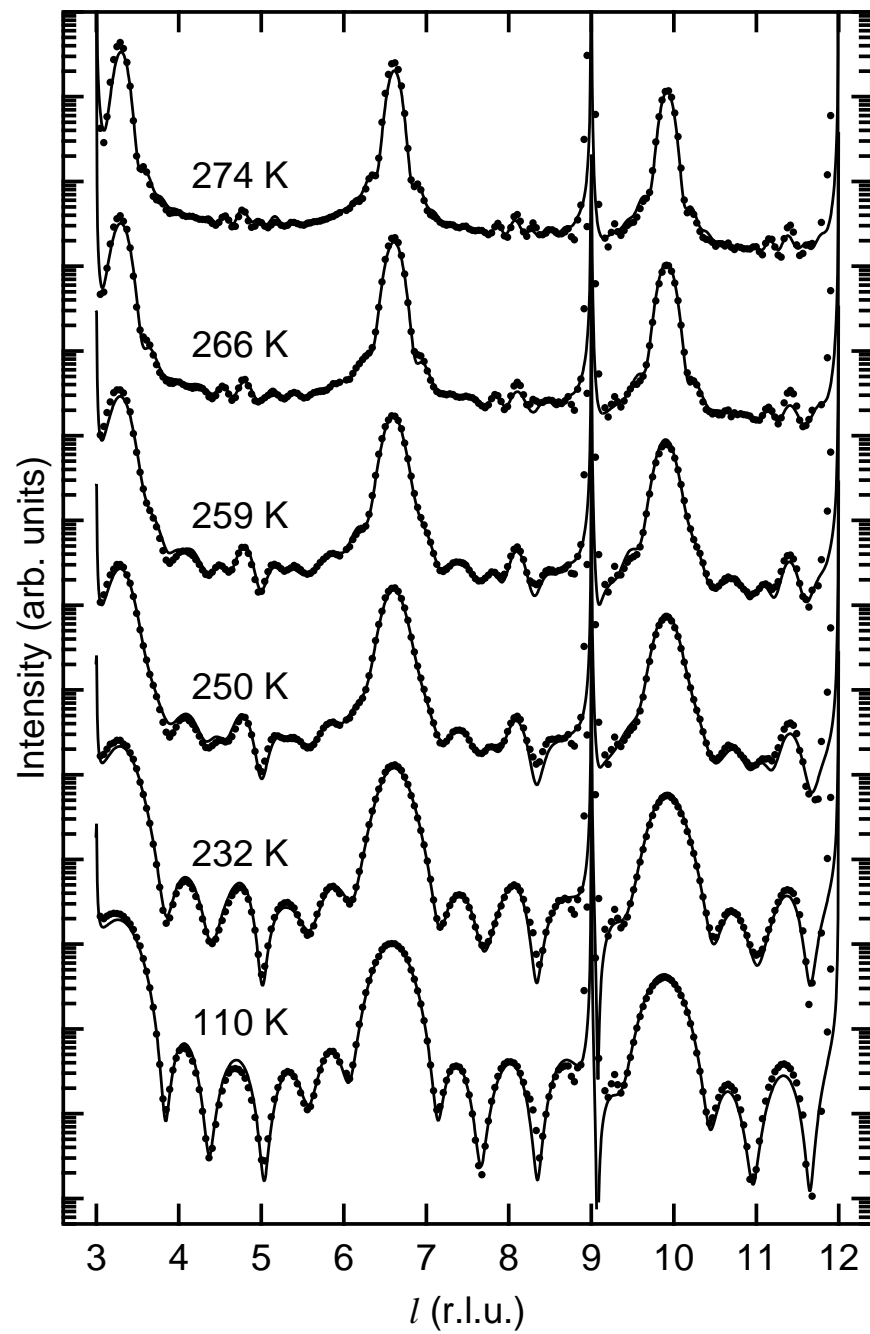
Figure 6.1: Extended x-ray reflectivity data (points) for a sample with a coverage of 6 AL after annealing to the temperatures indicated. Fits are shown as solid curves.

Figure 6.2: Extended x-ray reflectivity data (points) for a sample with a coverage of 11 AL after annealing to the temperatures indicated. Fits are shown as solid curves.

is, the smooth film at 110 K breaks up into nanostructures that get higher with increasing temperature. As discussed below, this curious behavior is related to a tendency for the system to favor the formation of surface regions covered by only a single wetting layer and oscillations in the surface energy similar to those calculated in Sec. 4.5 that favor the formation of islands of specific thicknesses.

The diminished fringes at the highest annealing temperatures indicate a relatively rough film. A broad distribution of thicknesses present on the surface should result in a relatively featureless reflectivity profile in-between the Pb Bragg peaks. However, in both sets of data small oscillations are evident roughly halfway between these peaks. Since these features occur close to the half-order position for Pb, they are indicative of a bilayer or quasibilayer periodicity in the film structure. In Chapter 5, enhanced half-order features due to quasibilayer distortions in the film layer structure were observed in smooth Pb films. However, as is shown below, due to film roughness such lattice distortions do not explain the half-order oscillations in this case. Rather, they can be attributed to a bilayer or quasibilayer periodicity in the thickness distribution p_N.

To illustrate the information content of these near-half-order oscillations and to show this effect is not due to lattice distortions, simulated reflectivity profiles were calculated for various thickness distributions with the atomic layer positions calculated using the local density gradient model of Sec. 4.4.2, which was found to accurately describe the lattice structure of Pb films in Chapter 5. Figure 6.3(a) shows the reflectivity for a rough sample with a Gaussian distribution of thicknesses as shown in Fig. 6.4(a). Even with the presence of quasibilayer lattice distortions, the broad distribution of thicknesses in the film obscures any half-order feature in the curve of Fig. 6.3(a). However, half-order oscillations are present in the simulated reflectivity of a sample that has a preference for either even or odd thicknesses, as shown in Fig. 6.3(b) with the distribution used shown in Fig. 6.4(b). However, the positioning of the oscillations in this case, exactly centered at the half-order position of $l \approx 5$, does not coincide with the positioning of the oscillations in the experimental data shown at the bottom of Fig. 6.3 (which is the 280 K data from Fig. 6.2), as is highlighted with the vertical dotted line. The shifting of the near-half-order oscillations observed can be reproduced by modifying the bilayer distribution of thicknesses so that the preference for even or odd thicknesses switches periodically, as shown in Fig. 6.4(c). Such an effect is expected due to the beating patterns found in the surface energy in Sec. 4.5. The corresponding reflectivity for such a simulation is shown in
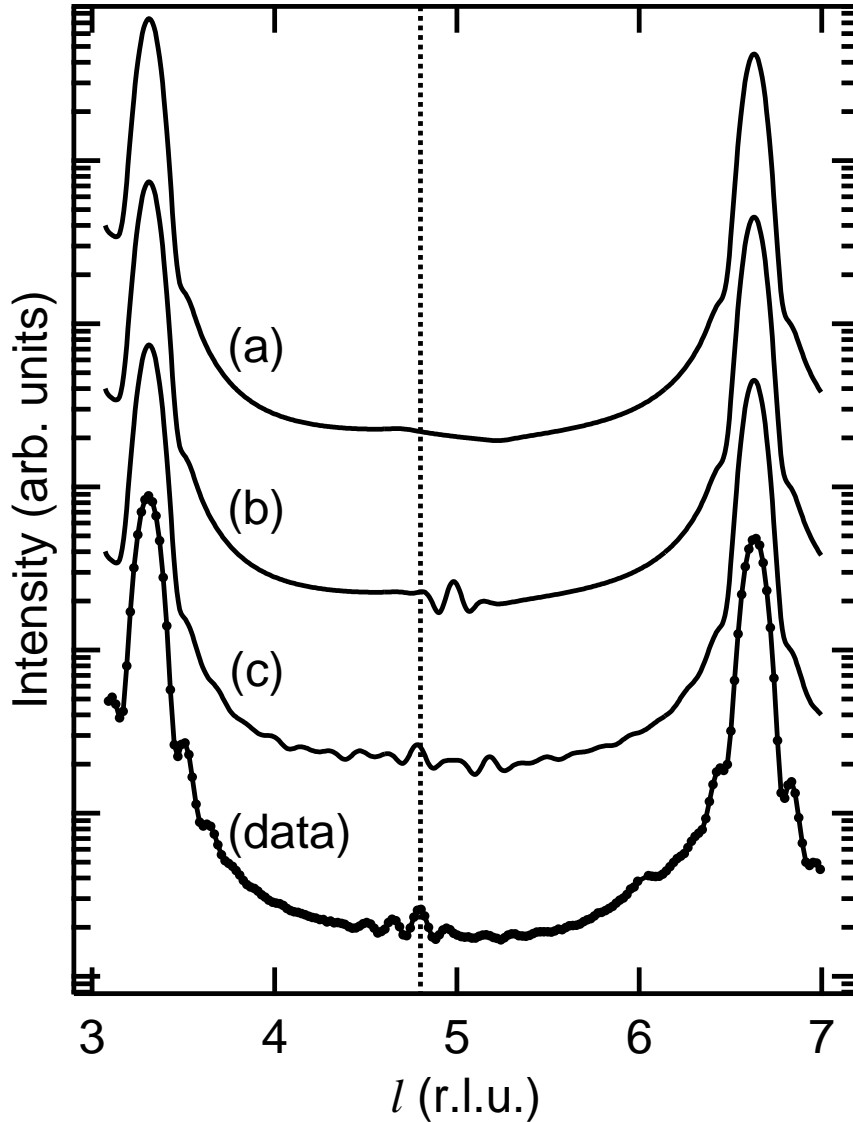
Figure 6.3: Simulations showing that the near-half-order oscillations in the reflectivity of samples annealed to high temperatures contain a significant amount of information. The corresponding thickness distributions are shown in Fig. 6.4. (a) The reflectivity from a surface whose thickness distribution follows a simple Gaussian. There are no oscillations in the reflectivity near the half-order point for the film overlayers. (b) A bilayer preference is added to the thickness distribution which results in oscillations at the half-order point, $l \approx 5$. (c) Phase reversal (even-odd crossover) is added to the bilayer distribution with the periodicity expected (every 9 AL). The oscillations are shifted slightly from the exact half-order position, coinciding more with those in the experimental data shown at the bottom, as highlighted with the vertical dotted line.
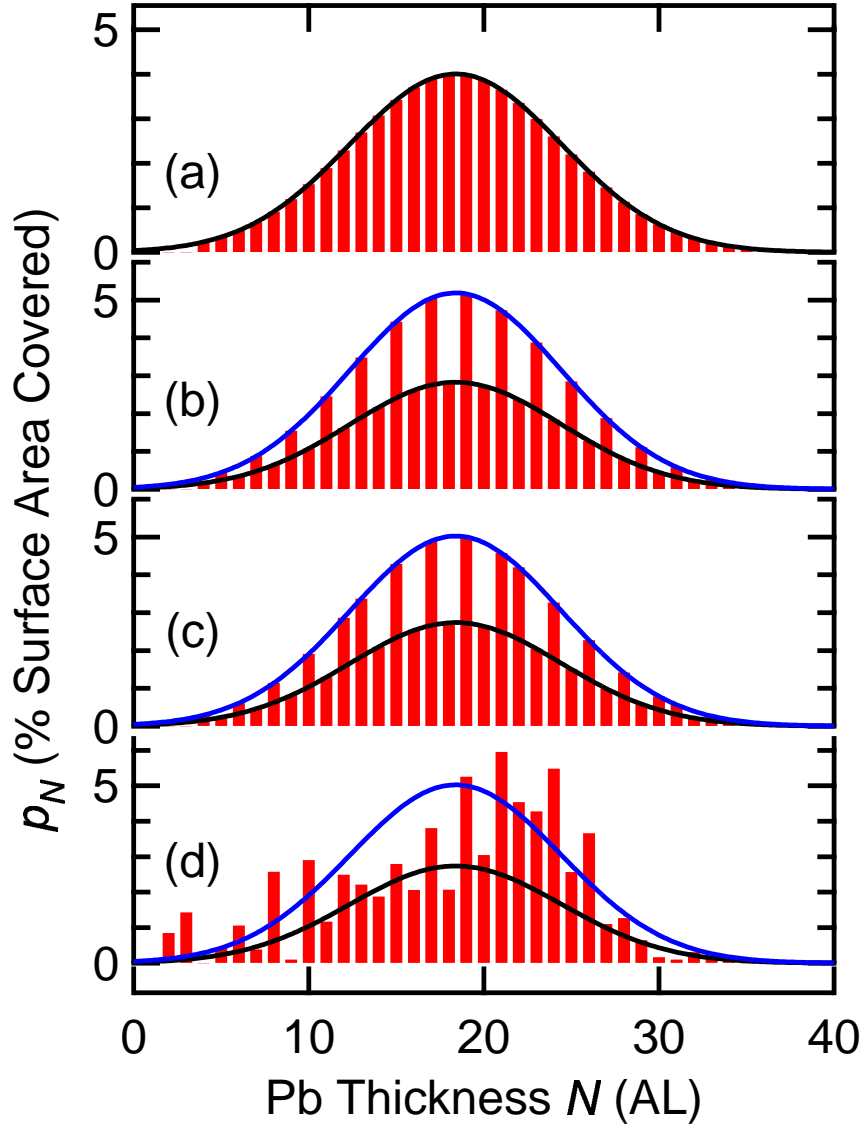
Figure 6.4: The thickness distributions used in the simulations of Fig. 6.3. (a) A simple Gaussian distribution. (b) A dual-Gaussian distribution where the upper envelope dictates the values for odd N. (c) The same dual-Gaussian distribution with an even-odd crossover every 9 AL, the expected period of the beating function in the surface energy. (d) The distribution resulting from a fit to the experimental data in Fig. 6.3(d), starting from the distribution in (c). In all cases, the coverage of the film, Eq. (2.43), is constrained to 11 AL (the coverage of the film whose data is shown) and the wetting layer, p_1, was adjusted such that the surface formed a closed film [Eq. (2.42)].

Fig. 6.3(c), where it can be seen that the near-half-order oscillations are now in phase with those in the data, although they are not reproduced exactly. By letting the p_N be independent parameters and using the values shown in Fig. 6.4(c) as an initial condition, an accurate fit to the data can be obtained, the results of which are shown in Fig. 6.4(d). Thus, the presence of the near-half-order oscillations in the data and their position relative to the Pb Bragg peaks is indicative of quasibilayer oscillations in the thickness distribution.

Detailed information on the surface morphology was obtained by fitting each reflectivity profile using Eq. (2.47) to obtain the thickness distribution present on the surface, $\{p_N\}$. Each p_N parameter was ultimately fit as an independent parameter except for p_1, the coverage of the wetting layer, which was constrained such that Eq. (2.42) was satisfied. At the higher annealing temperatures, when the distribution of thicknesses present on the surface is broad, the number of non-zero p_N values needed to describe the surface morphology is large. Local minima in parameter space were avoided by starting the fit for each temperature (except the first) from the best fit of the previous temperature, effectively following the film morphology as it evolves. Due to the large number of independent parameters used in some of the fits, the sensitivity of the fits to any individual p_N value was weak; however, as demonstrated with Figs. 6.3 and 6.4, the overall distribution of p_N values is well-determined by the information contained in the near-half-order oscillations in the x-ray reflectivity profiles. As a consequence, given the confidence in the form of the thickness distribution demonstrated above, the relative errors are estimated to be within 10% of each p_N value. The partial coherence factor in Eq. (2.47) was found to be near unity (all coherent scattering) for the lower annealing temperatures and on the order of 0.5 for the highest temperatures, consistent with a surface morphology that consists of many different height nanomesas that each extend laterally for significant distances.

6.3 Evolution of Film Morphology with Annealing

The thickness distributions determined from the fits to the reflectivity data in Fig. 6.1 are shown in Fig. 6.5. After deposition at 110 K, the thickness distribution is sharply peaked about $N = 6$, corresponding to a very smooth film with a rms roughness of about 1.3 Å. Upon annealing, no discernable changes in the reflectivity profile are observed until 232 K, at which point

regions of 8 and 10 AL start to form. These regions then become more prevalent by 250 K and the residual 7 AL region has disappeared, which is a less-stable thickness. The dominant thickness of the film is still 6 AL up to 266 K, though, at which point the distribution has broadened significantly. At 274 K, the preference for 6 AL due to the initial condition has disappeared and the surface has presumably reached a state of local equilibrium in which each thickness N is in equilibrium with its neighboring thicknesses $N \pm 1$. The rms roughness at this temperature is about 18 Å. The thickness distributions show a clear preference for certain thicknesses over others with a quasibilayer periodicity, which is expected because of the near-half-order oscillations present in the extended x-ray reflectivity profiles, as discussed in the last section. Two of the expected even-odd crossover points are evident as well at $N \approx 5$ and $N \approx 14$.

Phenomenologically, the fact that the thickness distribution gets broader after annealing is actually expected when one considers that the system follows a Stranski-Krastanov growth mode at room temperature, where islands form on top of a single wetting layer. However, in this case the distribution of thicknesses not only broadens, but its center moves upwards in N. That is, at lower temperatures, the distributions in Fig. 6.5 are peaked about the initial thickness of 6 AL, but at the final temperature, the average structure height above the wetting layer is about 12 AL, which implies that on average the surface features are getting higher with increasing temperature. To conserve the amount of Pb on the surface, the initially smooth film must break up into islands separated by increasingly wide regions of the surface covered only by a wetting layer. The amount of the surface covered by only a wetting layer, p_1, found in our analysis is shown in Fig. 6.6. It increases monotonically with the annealing temperature. The most stable configuration of the system is to maximize the coverage of the wetting layer, which is supported by first-principles calculations that show a deep global minimum at $N = 1$ in the surface energy (see Fig. 1.3). However, the system cannot fully maximize the coverage of the bare wetting layer due to kinetic limitations and thermal fluctuations that will tend to roughen the surface and favor a reasonable nanostructure height. The combination of these effects explains the annealing behavior observed.

In contrast to the 6 AL film, whose initial thickness persisted through most of the annealing process, indicating that this thickness is preferred, films with initial thicknesses that are not preferred exhibit a qualitatively distinct behavior. Figure 6.7 shows the thickness distributions for the film with an initial coverage of 11 AL (Fig. 6.2) and its morphological changes
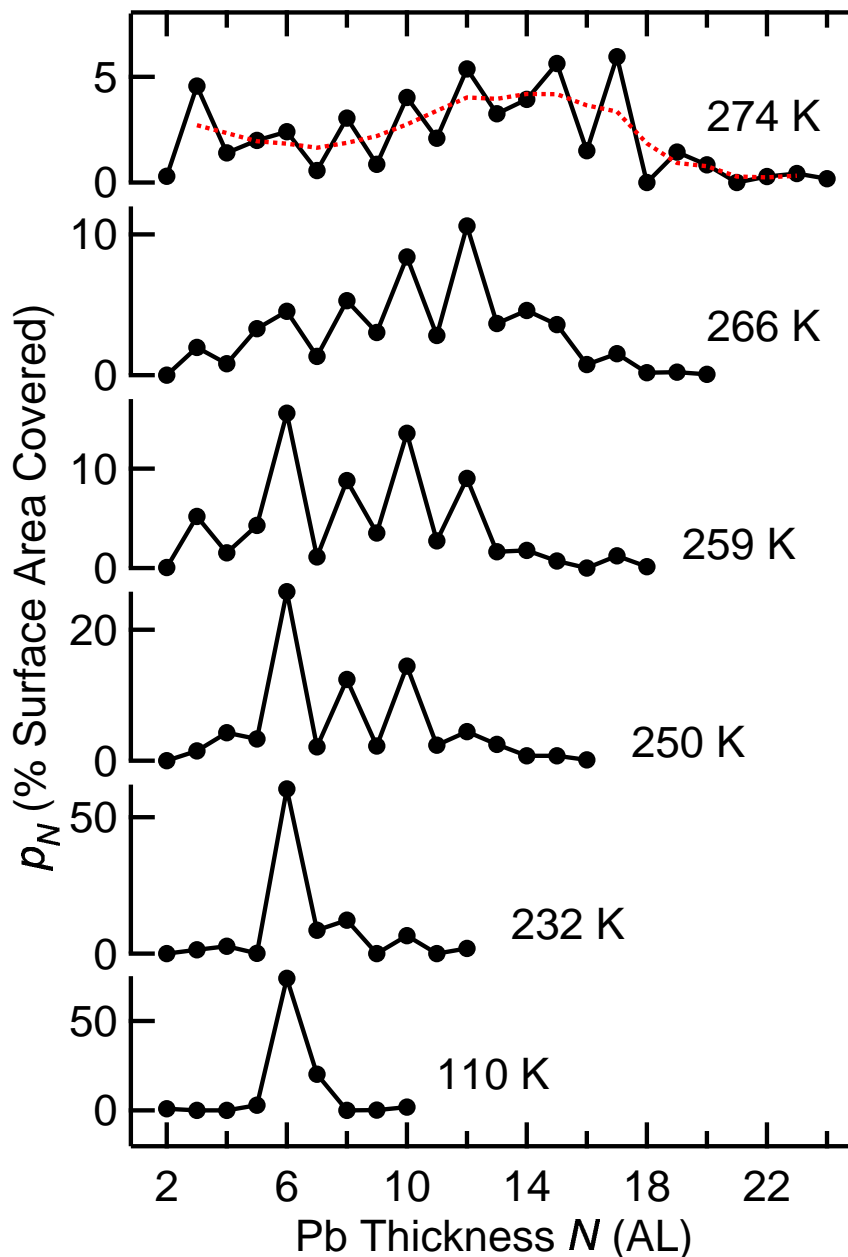
Figure 6.5: The coverage of different thicknesses present on the sample surface for each corresponding curve in Fig. 6.1, with the annealing temperatures indicated. The coverage values were determined via a fit using a model described in the text. The surface evolution is shown to evolve from a very smooth film at 110 K through various metastable "preferred thickness" states before reaching a state of local equilibrium. The preference of certain thicknesses over others corresponds to quasibilayer oscillations in the surface energy. The dotted line through the 274 K data is the result of applying a binomial filtering algorithm to the values for an analysis of the surface energy.
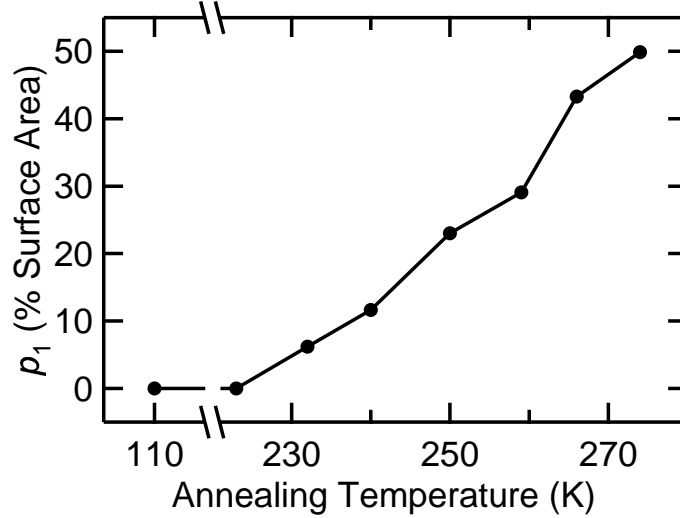
Figure 6.6: The amount of the 6 AL sample surface covered only by a single wetting layer increases with temperature. The surface energy has a deep global minimum at $N = 1$ that results in the wetting layer being the most stable configuration of the system.

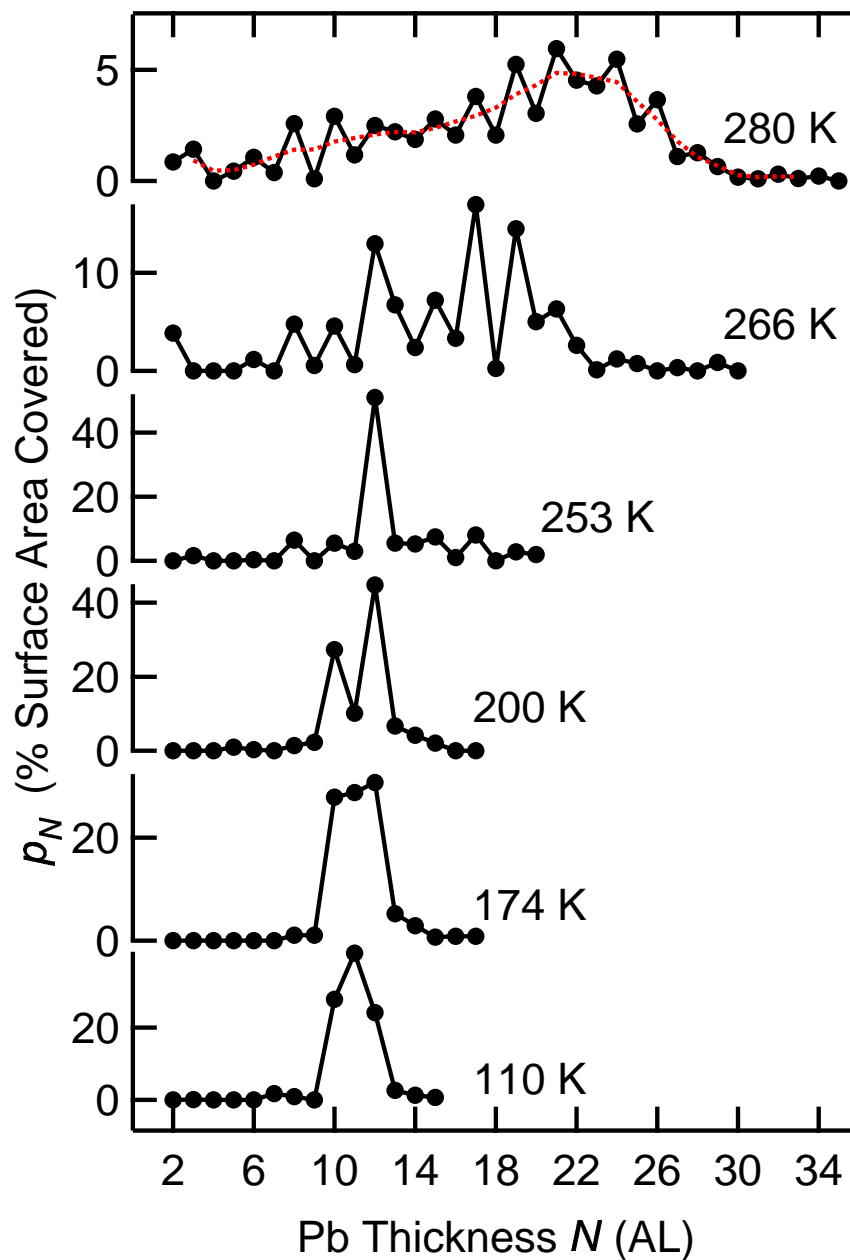upon annealing to the indicated temperatures. As with the 6 AL film, the initial distribution is sharply peaked about the initial thickness, consistent with a layer-by-layer growth mode. However, in this case the initially smooth film (3.2 Å rms roughness) begins to break up at a much lower temperature of 174 K. By 200 K, the coverage of the initial 11 AL has largely disappeared and the film has bifurcated into the neighboring thicknesses of 10 and 12 AL, both of which are more stable than 11 AL. At 253 K, the surface is dominated by regions of 12 AL, resulting from phase separation of the system into a state corresponding to a local minimum in the surface energy at $N = 12$ and a state in the global minimum at $N = 1$. It is this temperature range in which uniform height nanomesas have been observed in many microscopy studies [15, 19, 20, 22–25]. Annealing to higher temperatures results in a broadening of the thickness distribution until at 280 K, when the residual preference for 12 AL from the uniform height phase has disappeared, the film has reached local equilibrium (28 Å rms roughness). Since we started with a thicker film, there are more Pb atoms to rearrange and nanostructures of larger height are able to form on the surface. The final distribution of thicknesses is correspondingly much broader and has a higher average structure height above the wetting layer of approximately 18 AL. As a result, the oscillations in the distribution, which are indicative of variations in the relative stability of different thicknesses, are present over a wider range, allowing a more comprehensive analysis of the surface energy.

Figure 6.7: Evolution of the structure of the 11 AL film after annealing to the temperatures indicated, obtained from fits to the extended reflectivity data in Fig. 6.2. In contrast to the 6 AL film, which is a stable thickness, this film bifurcates at the comparatively low temperature of 174 K. Due to the higher volume (coverage) of Pb in the film, the final distribution of thicknesses is broader and peaked at a greater thickness than that in Fig. 6.5, providing information about the surface energy over a broader range of thicknesses.

6.4 Surface Energy

The variations in the thickness distributions of Figs. 6.5 and 6.7 are indicative of a relative preference for certain thicknesses over others. An experimental measure of the relative stability of a thickness can be obtained by comparing the fractional surface area it covers with that of its neighbors

$$p_N - \frac{p_{N-1} + p_{N+1}}{2} = -\frac{1}{2}p_N''$$ (6.1)

where p_N'' is the discrete second derivative of p_N. That is, thicknesses for which the local curvature of p_N is negative ($p_N'' < 0$) are relatively stable, since they cover more of the sample surface compared with their neighboring thicknesses. Conversely, if the local curvature of p_N is positive ($p_N'' > 0$), the thickness N is relatively unstable since the system prefers to form regions with thicknesses of $N \pm 1$ over N. The values of p_N'' for the highest annealing temperature data in Figs. 6.5 and 6.7 are shown as solid circles in Figs. 6.8(a) and 6.8(b), respectively. In both cases, quasibilayer oscillations about $p_N'' = 0$ are evident, a reflection of variations in the relative stability of different thicknesses. As mentioned above, the 11 AL sample provides information over a wider range of thicknesses than the 6 AL sample due to its greater initial thickness.

This effect will manifest itself as corresponding variations in the surface energy, similar to those seen in the free-electron calculations of Sec. 4.5. We can extract empirical information about the surface energy by relating it to the p_N parameters, which should follow a Boltzmann distribution

$$p_N = \mathcal{X}e^{-E_S(N)/k_B T}$$ (6.2)

where k_B is Boltzmann's constant and T is taken to be the annealing temperature. In the case of a system that is in global thermodynamic equilibrium, $\mathcal{X}$ is simply a constant of proportionality. However, in the present case it is only assumed that the system is in a state of local equilibrium, in which case $\mathcal{X}$ is a slowly varying function of N. Thus, $\mathcal{X}$ will depend on a variety of factors, including the film's annealing history. To remove this ill-defined function from the analysis, the self-normalized local variations in p_N are considered instead:

$$\delta p_N \equiv \frac{p_N - \bar{p}_N}{\bar{p}_N}$$ (6.3)

where $\bar{p}_N$ is a local average of p_N. Such a quantity corresponds to the smoothly varying background underlying the oscillations in the p_N values
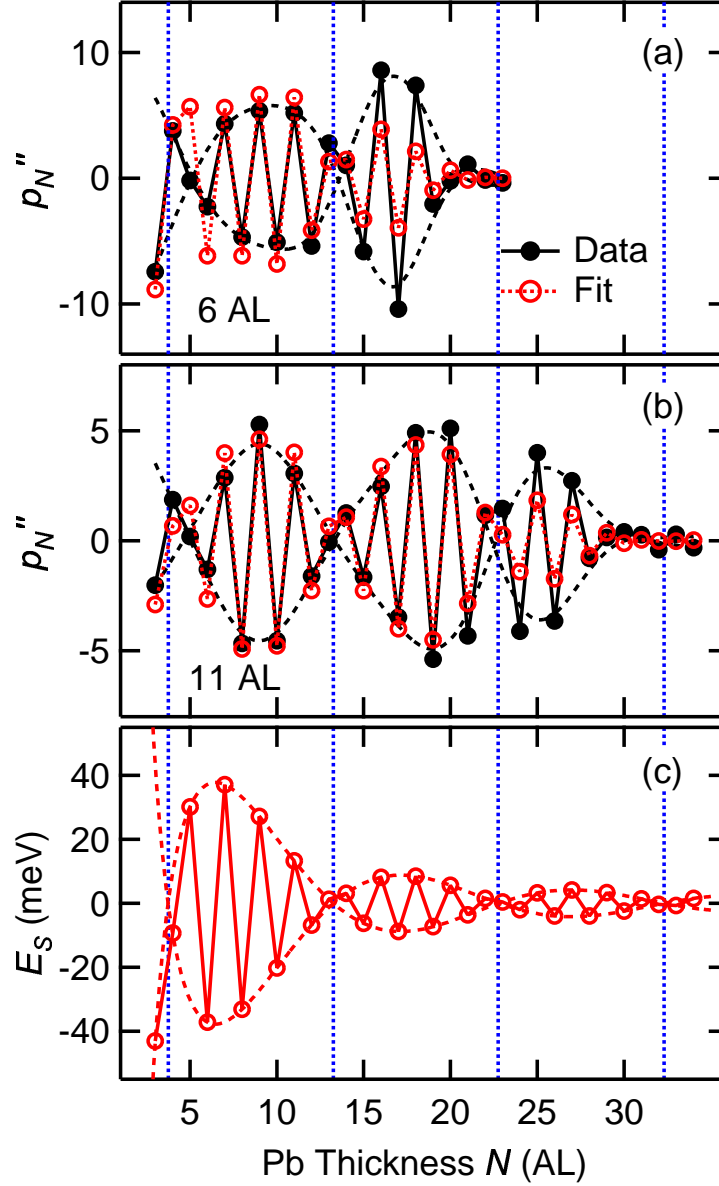
Figure 6.8: The discrete second derivative of the p_N values for the 274 K and 280 K data in Figs. 6.5 and 6.7 are shown as solid circles in (a) and (b), respectively. Two-parameter fits to these data as described in the text are shown as open circles, which accurately reproduce the quasibilayer oscillations and envelope beating functions. (c) The surface energy as calculated using Eq. (4.52) with the average parameters from the two fits in (a) and (b). Dashed lines show the beating envelopes for the experimental values in (a) and (b) and the calculated values in (c). Vertical dotted lines indicate the nodes in the beating envelope of the surface energy in (c), which correspond closely to the nodes in (a) and (b).

of Figs. 6.5 and 6.7. As long as $\bar{p}_N$ is calculated using only a small local set of p_N values, $\mathcal{X}$ can be regarded as being approximately constant over this set and δp_N is independent of $\mathcal{X}$. A reasonable method for calculating the local average is to use a binomial filtering algorithm [92]

$$\bar{p}_N = \frac{p_{N-1} + 2p_N + p_{N+1}}{4}. \tag{6.4}$$

The $\bar{p}_N$ values resulting from the application of this algorithm to the top p_N distributions in Figs. 6.5 and 6.7 are shown as dotted curves, which show that it indeed produces smooth curves. Using this algorithm also has the additional benefit that δp_N is simply related to the discrete second derivative of p_N

$$\delta p_N = \frac{-p_N''}{4\bar{p}_N}. \tag{6.5}$$

The empirical discrete second derivative values in Figs. 6.8(a) and 6.8(b) were fit using the function

$$\left(p_N''\right)_{\text{theory}} = -4\left(\bar{p}_N\right)_{\text{expt}}\left(\delta p_N\right)_{\text{theory}}, \tag{6.6}$$

where the theoretical version of δp_N is

$$\left(\delta p_N\right)_{\text{theory}} = \frac{4p_N}{p_{N-1} + 2p_N + p_{N+1}} - 1, \tag{6.7}$$

with the p_N values calculated using Eq. (6.2) and the sinusoidal approximation for the surface energy found from the free-electron model calculation, Eq. (4.52). Note that when this form for E_S is used, the constant offset in Eq. (4.52), B, cancels from Eq. (6.7). Due to a significant covariance found between the parameters A and α, where the adjustment of one parameter could be largely compensated for by a complementary adjustment of the other, the value for the decay exponent found in Sec. 4.5, $\alpha = 1.77$, was fixed in the fits. The analysis was found to be relatively insensitive to the specific value of the decay exponent, as long as it was between $0.9 < \alpha < 2.0$. Similar fits with $\alpha = 1$ yield comparable surface energies that differ by less than 3 meV for most of the thickness range available. The Fermi wave vector was taken to be the empirical value for bulk Pb(111), $k_F = 1.59$ Å^{-1}. Thus, only two adjustable parameters were used in the fits: A and ϕ. The fitted value of ϕ was $(0.49 \pm 0.01)\pi$ for both fits and the fitted value of A was 1.0 ± 0.3 eV for the 6 AL sample and 1.3 ± 0.2 eV for the 11 AL sample. The surface energy shown in Fig. 6.8(c) was calculated using the average of these two values.

6.5 Discussion

The annealing behavior of the two films is consistent with the surface energy shown in Fig. 6.8(c). At low temperatures, the system is kinetically limited and can therefore be found in a metastable state where the predominant thickness is energetically unfavorable, as with the 11 AL film in this study. However, as the film is annealed and given more thermal energy, the unstable 11 AL thickness easily bifurcates into the energetically preferred thicknesses of 10 and 12 AL. Upon further annealing, in some cases the film coalesces into a state where the surface is mostly covered by islands of uniform height. For the initial 11 AL film, the preferred thickness of the islands (nanomesas) is 12 AL, which is actually indicated to have a higher surface energy than 10 AL in Fig. 6.8(c). However, the system is prevented from forming uniform 10 AL islands since this thickness is smaller than the initial thickness, and the deep minimum in the surface energy for $N = 1$ favors the formation of surface regions covered only by a single wetting layer. As a consequence, a state that consists of 12 AL islands separated by regions of the surface covered only by the wetting layer is favored over a state in which both 10 and 12 AL islands are present.

In contrast, for a film whose initial predominant thickness is more stable, like the 6 AL film in this study, the surface morphology remains unchanged up to a much higher temperature. When it does begin to evolve, the initial 6 AL portion of the film is mostly retained while the unstable thicknesses (e.g., 7 AL) transform into higher stable thicknesses. The coverage of the initial thickness in this case only slowly decays with increasing temperature until local equilibrium is attained. We have collected similar data for other initial thicknesses, both preferred and not preferred, the annealing behavior of which is consistent with the results presented here.

The overall phase shift of the surface energy and its envelope beating function depend only on the boundary conditions at the film interfaces. As such, the nodal points in the surface energy envelope (the points where even-odd crossover occurs) should be found in the same places for the two data sets, which is indeed the case as seen in Fig. 6.8. Due to the symmetric boundary conditions used in the free-electron model of Sec. 4.5, the phase shift in the surface energy calculated from it is different from the experimentally determined phase shift, as one would expect. The amplitudes of oscillation found experimentally appear to be significantly greater than the free-electron amplitude; however, they are consistent with the amplitude found in the first-principles calculations shown in Fig. 1.3. The nodes in the

beating envelope occur with the periodicity expected given the bulk Fermi energy, although there is a slight discrepancy for the first node at $N \approx 5$ (see dotted vertical lines in Fig. 6.8). In this thickness region, interface effects are more significant and the free-electron approximation of the surface energy, Eq. (4.52), becomes less accurate. However, the empirical stability data for the lower N values in Figs. 6.8(a) and (b) is supported by independent photoemission measurements [41], indicating that the data are reliable.

6.6   Summary

This chapter presented temperature-dependent x-ray diffraction data showing the morphological evolution of Pb films grown on Si(111) substrates. The films were grown at 110 K, at which temperature the system follows a metastable layer-by-layer growth mode. By annealing the films to around 280 K in increments of 5–10 K, the surface morphology was observed passing through various metastable states before reaching a roughened state characterized by local equilibrium. The annealing behavior of two films with different initial thicknesses clearly shows that certain film thicknesses are more stable than others. A film with an initial thickness that is relatively stable (6 AL) remained intact up until approximately 230 K, at which point it began to roughen and explore the broader energy landscape. In contrast, a film with an initial thickness that is relatively unstable (11 AL) began to break up at the comparatively low temperature of 170–200 K, at which point it decomposed (phase separated) into regions of thicknesses with lower surface energies (islands dominated by a single height, 12 AL, surrounded by regions covered by the wetting layer only). This phenomenon of preferred heights can be explained by the phase separation of the system into a state corresponding to a local minimum in the surface energy (the uniform-height islands) and a state in the global minimum (the wetting layer).

In Sec. 4.5, the oscillations in the free-electron surface energy were found to closely follow a damped sinusoidal form with a wavelength of $\lambda_F/2$. This result is used to relate the details of the broad thickness distributions of the annealed films to their surface energy. These results draw a direct empirical link between the formation of quantized electronic states due to confinement of the itinerant electrons to a metal film (QSE) and the relative stability of different film thicknesses, which can exhibit large variations for sizes differing by as little as a single atomic layer. Understanding such effects is critical for the engineering of metallic nanoscale devices.

7 Conclusions and Outlook

This dissertation has presented research on size-dependent quantum electronic effects in ultrathin Pb/Si(111) films. These quantum size effects are investigated both theoretically with models based on a confined free-electron gas as well as experimentally with surface x-ray diffraction. The theoretical models predict quasibilayer variations both in the atomic-layer structure of the films as well as their surface energy as a function of thickness. These predictions are subsequently confirmed experimentally. In a layer-resolved study of smooth films of thicknesses 6–19 AL, distinctive features appear in the extended x-ray reflectivity spectra indicative of lattice distortions in the films with a quasibilayer superperiodicity. Detailed analysis reveals that these lattice distortions vary for different thickness films, again with a quasibilayer periodicity. In another experiment, the energetics of the system is investigated by annealing initially smooth Pb films to progressively higher temperatures, which causes the metastable films to break up into different height nanostructures. The structural evolution of these film nanostructures is observed throughout the annealing process, which reveals quasibilayer variations in the relative stability of the film structures as a function of height (film thickness). These variations are directly linked to oscillations in the surface energy similar to those calculated with the theoretical models. Together, these studies have determined that the effects of quantum confinement on atomic-scale metal structures can be dramatic and have a significant impact both on the lattice structure and the thermal stability of such nanostructures and films.

As always, there are many more directions in which this research could continue. For example, it would be interesting to see if the effects described in this work are also present in ultrathin liquid metal films. If a metal film with a thickness in the quantum regime could be prepared in the liquid state on a semiconductor substrate, then the properties of the film could conceivably be examined as a continuous function of thickness, which is in contrast with the integer number of atomic layers to which one is limited with epitaxial films. Another avenue of research that is currently being pursued is a real-time reflectivity study of the growth and annealing behaviors

of Pb/Si(111) films. In such a study, the reflectivity rod is measured by scanning the incident angle of the x rays while a range of exiting beams is collected simultaneously with an area detector such as a charge-coupled device (CCD). With this method, the rod can be measured in ∼2 min, another order-of-magnitude improvement over the ridge scan method outlined in Sec. 3.6.2. Using this technique, real-time studies can be readily performed of the growth of these films at different growth temperatures and/or growth rates. By exploring the temperature/growth-rate parameter space, one can deduce information on the kinetic barriers that are involved in the peculiar morphology that these films exhibit. In addition, the quantum size effects described here are found in a variety of other properties of metal nanostructures, the details of which remain unexplored in many cases. An excellent example of one such property is the superconducting transition temperature. Preliminary results from other research groups [7, 8] appear to show variations in T_c for thin Pb films with a bilayer periodicity, similar to the those observed in the surface energy reported here. However, these data are not comprehensive and many details of the effect remain unknown or unexplored.

In conclusion, it is clear that quantum electronic effects play a significant role in the physical characteristics of nanoscale metallic structures. These properties can deviate significant from their bulk counterparts. As the size of technological devices settles more firmly in the quantum regime, these size-dependent effects will be of utmost importance.

References

[1] F. K. Schulte. "A theory of thin metal films: electron density, potentials and work function." *Surf. Sci.* **55**, 427 (1976).

[2] S. Ciraci and I. P. Batra. "Theory of the quantum size effect in simple metals." *Phys. Rev. B* **33**, 4294 (1986).

[3] P. J. Feibelman. "Static quantum-size effects in thin crystalline, simple-metal films." *Phys. Rev. B* **27**, 1991 (1983).

[4] G. A. Sorokin. "Influence of the surface scattering on the quantum size effect." *Sov. Phys. Solid State* **15**, 1231 (1973).

[5] J. M. Blatt and C. J. Thompson. "Shape resonances in superconducting thin films." *Phys. Rev. Lett.* **10**, 332 (1963).

[6] B. G. Orr, H. M. Jaeger, and A. M. Goldman. "Transition-temperature oscillations in thin superconducting films." *Phys. Rev. Lett.* **53**, 2046 (1984).

[7] Y. Guo, Y.-F. Zhang, X.-Y. Bao, T.-Z. Han, Z. Tang, L.-X. Zhang, W.-G. Zhu, E. G. Wang, Q. Niu, Z. Q. Qiu, J.-F. Jia, Z.-X. Zhao, and Q.-K. Xue. "Superconductivity modulated by quantum size effects." *Science* **306**, 1915 (2004).

[8] T.-C. Chiang. "Superconductivity in thin films." *Science* **306**, 1900 (2004).

[9] N. Trivedi and N. W. Ashcroft. "Quantum size effects in transport properties of metallic films." *Phys. Rev. B* **38**, 12298 (1988).

[10] I. Vilfan, M. Henzler, O. Pfennigstorf, and H. Pfnür. "Anomalous thickness dependence of the Hall effect in ultrathin Pb layers on Si(111)." *Phys. Rev. B* **66**, 241306(R) (2002).

[11] P. Saalfrank. "Quantum size effects in thin lead films." *Surf. Sci.* **274**, 449 (1992).

[12] I. B. Altfeder, K. A. Matveev, and D. M. Chen. "Electron fringes on a quantum wedge." *Phys. Rev. Lett.* **78**, 2815 (1997).

[13] J. J. Paggel, C. M. Wei, M. Y. Chou, D.-A. Luh, T. Miller, and T.-C. Chiang. "Atomic-layer-resolved quantum oscillations in the work function: Theory and experiment for Ag/Fe(100)." *Phys. Rev. B* **66**, 233403 (2002).

REFERENCES

[14] P. J. Feibelman and D. R. Hamann. "Quantum-size effects in work functions of free-standing and adsorbed thin metal films." *Phys. Rev. B* **29**, 6463 (1984).

[15] M. Hupalo and M. C. Tringides. "Correlation between height selection and electronic structure of the uniform height Pb/Si(111) islands." *Phys. Rev. B* **65**, 115406 (2002).

[16] A. Mans, J. H. Dil, A. R. H. F. Ettema, and H. H. Weitering. "Quantum electronic stability and spectroscopy of ultrathin Pb films on Si(111)7× 7." *Phys. Rev. B* **66**, 195410 (2002).

[17] A. Crottini, D. Cvetko, L. Floreano, R. Gotter, A. Morgante, and F. Tommasini. "Step height oscillations during layer-by-layer growth of Pb on Ge(001)." *Phys. Rev. Lett.* **79**, 1527 (1997).

[18] J. Braun and J. P. Toennies. "Observation of a quantum size effect in the surface electron density of thin lead films." *Surf. Sci.* **384**, L858 (1997).

[19] W. B. Su, S. H. Chang, W. B. Jian, C. S. Chang, L. J. Chen, and T. T. Tsong. "Correlation between quantized electronic states and oscillatory thickness relaxations of 2D Pb islands on Si(111)-(7x7) surfaces." *Phys. Rev. Lett.* **86**, 5116 (2001).

[20] W.-B. Su, S.-H. Chang, C.-S. Chang, L. J. Chen, and T. T. Tsong. "Quantum size effects in low-temperature growth of Pb islands on Si(111)7x7 surfaces." *Jap. J. Appl. Phys.* **40**, 4299 (2001).

[21] R. Otero, A. L. Vázquez de Parga, and R. Miranda. "Observation of preferred heights in Pb nanoislands: A quantum size effect." *Phys. Rev. B* **66**, 115401 (2002).

[22] K. Budde, E. Abram, V. Yeh, and M. C. Tringides. "Uniform, self-organized, seven-step height Pb/Si(111)-(7 × 7) islands at low temperatures." *Phys. Rev. B* **61**, R10602 (2000).

[23] M. Hupalo, S. Kremmer, V. Yeh, L. Berbil-Bautista, E. Abram, and M. C. Tringides. "Uniform island height selection in the low temperature growth of Pb/Si(111)-(7x7)." *Surf. Sci.* **493**, 526 (2001).

[24] V. Yeh, L. Berbil-Bautista, C. Z. Wang, K. M. Ho, and M. C. Tringides. "Role of the metal/semiconductor interface in quantum size effects: Pb/Si(111)." *Phys. Rev. Lett.* **85**, 5158 (2000).

[25] M. Hupalo, V. Yeh, L. Berbil-Bautista, S. Kremmer, E. Abram, and M. C. Tringides. "Uniform height island growth of Pb on Si(111)-Pb($\sqrt{3} \times \sqrt{3}$) at low temperatures." *Phys. Rev. B* **64**, 155307 (2001).

[26] H. Hong, C.-M. Wei, M. Y. Chou, Z. Wu, L. Basile, H. Chen, M. Holt, and T.-C. Chiang. "Alternating layer and island growth of Pb on Si by

136

spontaneous quantum phase separation." *Phys. Rev. Lett.* **90**, 076104 (2003).

[27] L. Gavioli, K. R. Kimberlin, M. C. Tringides, J. F. Wendelken, and Z. Zhang. "Novel growth of Ag islands on Si(111): Plateaus with a singular height." *Phys. Rev. Lett.* **82**, 129 (1999).

[28] L. Huang, S. J. Chey, and J. H. Weaver. "Metastable structures and critical thicknesses: Ag on Si(111)-7 × 7." *Surf. Sci.* **416**, L1101 (1998).

[29] C. M. Wei and M. Y. Chou. "Theory of quantum size effects in thin Pb(111) films." *Phys. Rev. B* **66**, 233408 (2002).

[30] W. B. Jian, W. B. Su, C. S. Chang, and T. T. Tsong. "Vertical friedel oscillations in interface-induced surface charge modulations of ultrathin quantum islands." *Phys. Rev. Lett.* **90**, 196603 (2003).

[31] B. J. Hinch, C. Koziol, J. P. Toennies, and G. Zhang. "Single and double layer growth mechanisms induced by quantum size effects in Pb films deposited on Cu(111)." *Vacuum* **42**, 309 (1991).

[32] M. Valden, X. Lai, and D. W. Goodman. "Onset of catalytic activity of gold clusters on titania with the appearance of nonmetallic properties." *Science* **281**, 1647 (1998).

[33] N. D. Lang and W. Kohn. "Theory of metal surfaces: Charge density and surface energy." *Phys. Rev. B* **1**, 4555 (1970).

[34] Z. Zhang, Q. Niu, and C.-K. Shih. ""Electronic growth" of metallic overlayers on semiconductor substrates." *Phys. Rev. Lett.* **80**, 5381 (1998).

[35] T. Valla, M. Kralj, A. Šiber, M. Milun, P. Pervan, P. D. Johnson, and D. P. Woodruff. "Oscillatory electron-phonon coupling in ultra-thin silver films on V(100)." *J. Phys.: Condens. Matter* **12**, L477 (2000).

[36] T.-C. Chiang. "Photoemission studies of quantum well states in thin films." *Surf. Sci. Rep.* **39**, 181 (2000).

[37] L. Aballe, A. Barinov, A. Locatelli, S. Heun, and M. Kiskinova. "Tuning surface reactivity via electron quantum confinement." *Phys. Rev. Lett.* **93**, 196103 (2004).

[38] D.-A. Luh, T. Miller, J. J. Paggel, and T.-C. Chiang. "Large electron-phonon coupling at an interface." *Phys. Rev. Lett.* **88**, 256802 (2002).

[39] G. Materzanini, P. Saalfrank, and P. J. D. Lindan. "Quantum size effects in metal films: energies and charge densities of Pb(111) grown on Cu(111)." *Phys. Rev. B* **63**, 235405 (2001).

REFERENCES

[40] D. Schmicker, T. Hibma, K. A. Edwards, P. B. Howes, J. E. Macdonald, M. A. James, M. Breeman, and G. T. Barkema. "Low-temperature growth of thin Pb layers and the quantum size effect." *J. Phys.: Condens. Matter* **9**, 969 (1997).

[41] M. H. Upton, C. M. Wei, M. Y. Chou, T. Miller, and T.-C. Chiang. "Thermal stability and electronic structure of atomically uniform Pb films on Si(111)." *Phys. Rev. Lett.* **93**, 026802 (2004).

[42] J.-H. Cho, K. S. Kim, C. T. Chan, and Z. Zhang. "Oscillatory energetics of flat Ag films on MgO(001)." *Phys. Rev. B* **63**, 113408 (2001).

[43] C. M. Wei and M. Y. Chou. "Effects of the substrate on quantum well states: A first-principles study for Ag/Fe(100)." *Phys. Rev. B* **68**, 125406 (2003).

[44] D.-A. Luh, T. Miller, J. J. Paggel, M. Y. Chou, and T.-C. Chiang. "Quantum electronic stability of atomically uniform films." *Science* **292**, 1131 (2001).

[45] A. R. Smith, K.-J. Chao, Q. Niu, and C.-K. Shih. "Formation of atomically flat silver films on GaAs with a "silver mean" quasi periodicity." *Science* **273**, 226 (1996).

[46] E. Ganz, I. Hwang, F. Xiong, S. K. Theiss, and J. Golovchenko. *Surf. Sci.* **257**, 259 (1991).

[47] M. J. Hadley, S. P. Tear, and T. N. Doust. *J. Phys. Cond. Matt.* **3**, S277 (1989).

[48] P. B. Howes, K. A. Edwards, D. J. Hughes, J. E. Macdonald, T. Hibma, T. Bootsma, and M. A. James. "Influence of interfacial atomic structure on the Schottky-barrier height of Si(111)-Pb." *Phys. Rev. B* **51**, 17740 (1995).

[49] P. B. Howes, K. A. Edwards, J. E. Macdonald, T. Hibma, T. Bootsma, M. A. James, and C. L. Nicklin. "The atomic structure of the Si(111)-($\sqrt{3} \times \sqrt{3}$)-Pb reconstruction." *Surf. Rev. Lett.* **5**, 163 (1998).

[50] K. Horn, B. Riehl, A. Zartner, D. E. Eastman, K. Hermann, and J. Noffke. "Electronic energy bands of lead: Angle-resolved photoemission and band-structure calculations." *Phys. Rev. B* **30**, 1711 (1984).

[51] A. Zangwill. *Physics at Surfaces* (Cambridge University Press, Cambridge, 1988).

[52] R. Feidenhans'l. "Surface structure determination by x-ray diffraction." *Surf. Sci. Rep.* **10**, 105 (1989).

[53] I. K. Robinson. *Handbook on Synchrotron Radiation*, volume 3, pp. 221–266 (North-Holland Publishing Company, 1991).

REFERENCES

[54] I. K. Robinson and D. J. Tweet. "Surface x-ray diffraction." *Rep. Prog. Phys.* **55**, 599 (1992).

[55] J. Als-Nielsen and D. McMorrow. *Elements of Modern X-Ray Physics* (John Wiley & Sons, Chichester, 2001).

[56] B. E. Warren. *X-ray Diffraction* (Dover, New York, 1969).

[57] L. H. Schwartz and J. B. Cohen. *Diffraction from Materials* (Springer-Verlag Berlin, Heidelberg, 1987), second edition.

[58] N. W. Ashcroft and N. D. Mermin. *Solid State Physics* (Harcourt College Publishers, Philadelphia, 1976).

[59] M. P. Marder. *Condensed Matter Physics* (John Wiley & Sons, New York, 2000).

[60] I. K. Robinson and E. Vlieg. "X-ray reflectivity study of the Si(111)7×7 surface." *Surf. Sci.* **261**, 123 (1992).

[61] R. D. Aburano. *Interfacial Studies of Buried Semiconductor Surfaces.* Ph.D. thesis, University of Illinois at Urbana-Champaign, Urbana, Illinois (1997).

[62] J. D. Jackson. *Classical Electrodynamics*, chapter 14.8, pp. 694–697 (John Wiley & Sons, New York, 1999), third edition.

[63] E. N. Maslen, A. G. Fox, and M. A. O'Keefe. *International Tables for X-Ray Crystallography*, volume C, pp. 554–584 (Kluwer Academic Publishers, Dordrecht, The Netherlands, 2004), third edition.

[64] J. Z. Tischler and B. W. Batterman. "Determination of magnitude, phase, and temperature dependence of forbidden reflections in silicon and germanium." *Phys. Rev. B* **30**, 70607066 (1984).

[65] I. K. Robinson. "Crystal truncation rods and surface roughness." *Phys. Rev. B* **33**, 3830 (1986).

[66] E. Vlieg. "Integrated intensities using a six-circle surface x-ray diffractometer." *J. Appl. Cryst.* **30**, 532 (1997).

[67] E. D. Specht and F. J. Walker. "A method for the accurate determination of crystal truncation rod intensities by x-ray diffraction." *J. Appl. Cryst.* **26**, 166 (1993).

[68] J. M. Bloch. "Angle and index caculations for a 'z-axis' x-ray diffractometer." *J. Appl. Cryst.* **18**, 33 (1985).

[69] L.-M. Peng, G. Ren, S. L. Dudarev, and M. J. Whelan. "Debye-Waller factors and absorptive scattering factors of elemental crystals." *Acta Cryst.* **A52**, 456 (1996).

[70] K. A. Edwards, P. B. Howes, J. E. Macdonald, T. Hibma, T. Bootsma, and M. A. James. "Observation of a structrual transition during the low-temperature growth of the Si(111)7 × 7-Pb interface." *Surf. Sci.* **424**, 169 (1999).

[71] J. A. Venables. *Introduction to Surface and Thin Film Processes* (Cambridge University Press, Cambridge, 2000).

[72] A. Roth. *Vacuum Technology* (Elsevier Science Publishers, 1990), third, updated and enlarged edition.

[73] J. F. O'Hanlon. *A User's Guide to Vacuum Technology* (John Wiley & Sons, New York, 1989), second edition.

[74] G. F. Knoll. *Radiation Detection and Measurement* (John Wiley & Sons, New York, 1989), second edition.

[75] B. E. A. Saleh and M. C. Teich. *Fundamentals of Photonics* (John Wiley & Sons, New York, 1991).

[76] J. G. Timothy and R. P. Madden. *Handbook on Synchrotron Radiation*, volume 1A, chapter 5, pp. 315–366 (North-Holland Publishing Company, Amsterdam, 1983).

[77] L. H. Schwartz and J. B. Cohen. *Diffraction from Materials*, chapter D.2, pp. 554–557. In [57] (1987), second edition.

[78] J. D. Jackson. *Classical Electrodynamics* (John Wiley & Sons, New York, 1999).

[79] J. A. Carlisle, T. Miller, and T.-C. Chiang. "Photoemission study of the growth, desorption, Schottky-barrier formation, and atomic structure of Pb on Si(111)." *Phys. Rev. B* **45**, 3400 (1992).

[80] P. B. Howes, K. A. Edwards, D. J. Hughes, J. E. Macdonald, T. Hibma, and M. A. James. "A surface x-ray diffraction study of the Si(lll)-Pb-buried interface." *Surf. Sci.* **331-333**, 646 (1995).

[81] M. H. Upton, T. Miller, and T.-C. Chiang. "Absolute determination of film thickness from photoemission: Application to atomically uniform films of Pb on Si." *Appl. Phys. Lett.* **85**, 1235 (2004).

[82] F. Grey, R. Feidenhans'l, M. Nielsen, and R. L. Johnson. "The relationship between the metastable and stable phases of Pb/Si(111)." *Colloque de Physique* **C7**, 181 (1989).

[83] P. Czoschke, H. Hong, L. Basile, and T.-C. Chiang. "Surface x-ray diffraction study and quantum well analysis of the growth and atomic-layer structure of ultrathin Pb/Si(111) films." *Phys. Rev. B* **71** (2005). (in press).

REFERENCES

[84] P. Czoschke, H. Hong, L. Basile, and T.-C. Chiang. "Quantum size effects in the surface energy of Pb/Si(111) film nanostructures studied by surface x-ray diffraction and model calculations." (2005). (submitted).

[85] D. A. Ricci, T. Miller, and T.-C. Chiang. "Chemical tuning of metal-semiconductor interfaces." *Phys. Rev. Lett.* **93**, 136801 (2004).

[86] P. Czoschke, H. Hong, L. Basile, and T.-C. Chiang. "Quantum oscillations in the layer structure of thin metal films." *Phys. Rev. Lett.* **91**, 226801 (2003).

[87] Y. S. Li, F. Jona, and P. M. Marcus. "Multilayer relaxation of a Pb{111} surface." *Phys. Rev. B* **43**, 6337 (1991).

[88] C. M. Wei and M. Y. Chou. Unpublished.

[89] A. Samsavar, E. S. Hirschorn, T. Miller, F. M. Leibsle, J. A. Eades, and T.-C. Chiang. "High-resolution imaging of a dislocation on Cu(111)." *Phys. Rev. Lett.* **65**, 1607 (1990).

[90] M. F. Crommie, C. P. Lutz, and D. M. Eigler. "Imaging standing waves in a two-dimensional electron gas." *Nature* **363**, 524 (1993).

[91] P. Czoschke, H. Hong, L. Basile, and T.-C. Chiang. "Quantum beating patterns in the energetics of Pb film nanostructures." *Phys. Rev. Lett.* **93**, 036103 (2004).

[92] P. Marchand and L. Marmet. "Binomial smoothing filter: A way to avoid some pitfalls of least-squares polynomial smoothing." *Rev. Sci. Instrum.* **54**, 1034 (1983).

Author's Biography

Peter Jeremy Czoschke was born on April 17, 1975 in Madison, Wisconsin. He graduated magna cum laude with distinction in physics and honors in music performance from Carleton College in 1997. From 1997–2000 he worked at ServiceNet, LLC; UnitedHealth Group; and Comdisco, Inc. in various information technology technical roles. He received an M.S. in physics from the University of Illinois at Urbana-Champaign in 2002 and his Ph.D. in 2005. He is married to Rebecca Leech Czoschke and has one daughter, Meredith Victoria Czoschke.

Publications

P. Czoschke, Hawoong Hong, L. Basile, and T.-C. Chiang. "Calculated and observed quantum size effects in the surface energy of ultrathin Pb films on Si(111)." *Physical Review B* , (2005, submitted).

P. Czoschke, Hawoong Hong, L. Basile, and T.-C. Chiang. "An x-ray study of the growth and layer structure of ultrathin Pb/Si(111) films." *Physical Review B* **71**, (2005, in press).

P. Czoschke, Hawoong Hong, L. Basile, and T.-C. Chiang. "Quantum Beating Patterns in the Energetics of Pb Film Nanostructures." *Physical Review Letters* **93**, 036103 (2004).

L. Basile, Hawoong Hong, **P. Czoschke**, and T.-C. Chiang. "X-ray studies of the growth of smooth Ag films on Ge(111)-c(2x8)." *Applied Physics Letters* **84**, 4995–4997 (2004).

P. Czoschke, Hawoong Hong, L. Basile, and T.-C. Chiang. "Quantum Oscillations in the Layer Structure of Thin Metal Films." *Physical Review Letters* **91**, 226801 (2003).

M. Holt, **P. Czoschke**, Hawoong Hong, P. Zschack, H. K. Birnbaum, and T.-C. Chiang. "Phonon dispersions in niobium determined by x-ray transmission scattering." *Physical Review B* **66**, 064303 (2002).